Energy-Aware Design Methods for Piezoelectric Mechatronic Systems

HSIN CHENG

A DISSERTATION
PRESENTED TO THE FACULTY
OF PRINCETON UNIVERSITY
IN CANDIDACY FOR THE DEGREE
OF DOCTOR OF PHILOSOPHY

RECOMMENDED FOR ACCEPTANCE
BY THE DEPARTMENT OF
ELECTRICAL AND COMPUTER ENGINEERING

ADVISER: MINJIE CHEN

MARCH 2026

Abstract

Piezoelectric mechatronic systems merge piezoelectric actuators with electrical circuits and mechanical structures, offering a promising approach for intelligent structures to interact with humans and the environment. Despite their potential, these systems face multiple operational challenges. First, piezoelectric actuators often require hundreds to over a thousand volts for meaningful actuation. Traditional high-voltage power sources are heavy and bulky, limiting the applicability of piezoelectric mechatronic systems. Second, the energy-efficiency of piezoelectric actuators is highly sensitive to driving conditions and the mechanical structures to which the actuators are attached, highlighting the need for end-to-end electrical-mechanical co-design. Third, material variation, aging, and degradation of piezoelectric actuators decrease system controllability and robustness, necessitating proper implementation of control strategies.

This thesis presents an extendable Vibrating Intelligent Piezo-Electric Robot (eViper) platform for studying untethered, multi-actuator, and multipurpose energy-aware mechatronic systems. Based on the measured electrical characteristics of piezoelectric actuators, a scalable and modular power architecture was designed to convert 7 V battery input to multiple voltage levels up to 1500 V to drive these actuators. Automated data collection was performed to record the robot's motion dynamics under different driving waveforms. Data-driven models were used to identify optimal driving waveforms for maximum energy efficiency. A closed-loop feedback control system based on computer vision was implemented for path-tracking tasks. The thesis provides insights for future research on electrical, mechanical, and control co-design to achieve precise, flexible, and energy-efficient operation of piezoelectric mechatronic systems.

Acknowledgments

I would like to express my deepest gratitude to my advisor, Dr. Minjie Chen, for his continuous guidance, support, and patience throughout this research. I would also like to thank my committee members, Dr. Naveen Verma and Dr. James C. Sturm, for their valuable feedback and the time devoted to this study. I thank my thesis reader, Dr. Tian-Ming Fu, for his expertise and thoughtful comments on this thesis. I am grateful to my colleagues and lab mates for their timely assistance and constructive discussions. Finally, I thank my family and friends for their emotional support throughout the years of my Ph.D. study.

Contents

List of Tables

List of Figures

1

Introduction

This chapter is based on work published in the following paper or currently under review:

- *H. Cheng, Z. Zheng, P. Kumar, W. Afridi, B. Kim, S. Wagner, N. Verma, J. C. Sturm and M. Chen, "eViper: A Scalable Platform for Untethered Modular Soft Robots," 2023 IEEE/RSJ International Conference on Intelligent Robots and Systems (IROS).*

- *H. Cheng, Z. Zheng, E. Veilleux, S. Wagner, N. Verma, J. C. Sturm and M. Chen, "eViper: A Scalable Untethered End-to-End 2D Soft Robotics Research Platform with Data Driven Modeling and Control," IEEE Transactions on Robotics (T-RO) (Under Review).*

1.1 Background and Motivation

Piezoelectric mechatronic systems integrate piezoelectric actuators, driving electronics, and mechanical structures into tightly coupled electromechanical platforms. They are capable of converting electrical energy into mechanical motion, or vice versa. By utilizing the piezoelectric effect, these systems can produce fast and precise deformation. They have found applications in biomedical devices, robotics, and precision manufacturing [1–5].

In this thesis, piezoelectric mechatronic systems are studied in the context of a soft robotic platform. Soft robots are robotic systems constructed primarily from compliant materials. Their deformable nature gives them unique advantages in unstructured environments, including impact tolerance, robustness, safety, and adaptability. However, these properties also introduce significant challenges. Soft robots often exhibit highly nonlinear dynamics and limited force output compared to rigid-body systems [6, 7]. Moreover, their deformable structures hinder accurate modeling, sensing, and control, and make it difficult to systematically characterize the relationships among electrical input energy, mechanical output energy, and resulting locomotion performance. These challenges motivate the development of new system-level hardware design strategies and energy-aware characterization approaches for soft robotic platforms.

1.2 Research Gap and Problem Statement

Soft robots often include electrostatic soft actuators, such as piezoelectric and dielectric elastomer actuators, because they enable compact designs, high energy density, and fast response time. However, they often require hundreds to thousands of volts for actuation. Lightweight power management systems have been proposed, powered by batteries [8–14] or photovoltaic arrays [15], to achieve integrated design and untethered operation. However, the locomotion performance of soft robots is highly sensitive to the driving waveform and frequency. Prior work has largely focused on achieving fast or untethered motion [3, 16–18], while systematic characterization of how locomotion behavior varies across excitation waveforms remains limited.

It's challenging to use analytical methods to describe the complex interactions among soft actuators, compliant robot bodies, onboard electronics and batteries, and the environment. Previous studies have explored various aspects of soft robot locomotion, including crawling and jumping [19, 20], turning [21, 22], friction manipulation [23, 24], and frequency-dependent behavior [25, 26]. However, the analytical models reported in the literature are often highly system-specific and difficult to generalize to scalable, multi-actuator soft robotic platforms. Moreover, while existing robotic simulation tools, such as PyBullet [27, 28] and MuJoCo [29], are well suited for modeling rigid components and motor-driven systems, they offer limited accuracy in capturing the nonlinear continuum dynamics and material behavior of soft robots [30]. Consequently, determining how multiple actuators should coordinate to achieve fast and energy-efficient locomotion across different environments remains an open challenge for sensing and control.

During locomotion, energy is continuously converted between the electrical and mechanical domains. It is crucial to quantify the total required energy for actuation across waveforms and frequencies, because it (1) enables informed battery sizing and runtime estimation, (2) supports energy-aware control strategy, and (3) provides an end-to-end system-level performance metric. Despite this, existing literature rarely investigates system performance from an energy point of view.

1.3 Objectives and Scope

The objectives of this thesis are:

- To establish experimental methods to quantify the electrical-to-mechanical energy conversion efficiency of piezoelectric actuators.
- To design a lightweight and efficient power converter capable of boosting battery voltage to drive piezoelectric actuators, with customizable output voltage, waveform, and frequency.
- To develop a systematic soft robotic framework to analyze and model the impact of driving signals on the locomotion behavior of soft robots.
- To investigate the energy transfer efficiency from the battery to a single actuator across different driving waveforms and frequencies.
- To quantify the power-to-velocity conversion efficiency of the entire robotic system across driving waveforms and frequencies.
- To implement and evaluate feedback control strategies to demonstrate the maneuverability of the soft robotic platform.

1.4 Contributions of This Thesis

The contributions of this thesis are:

- Designed and implemented a lightweight and efficient power converter capable of boosting a 7.4 V battery input to 300 V and 1500 V to drive piezoelectric actuators, with customizable output voltage, waveform, and frequency.
- Developed and experimentally demonstrated a system-level energy analysis framework for untethered, multi-actuator piezoelectric soft robots, connecting battery-level energy input, power electronics, and actuator energy consumption.

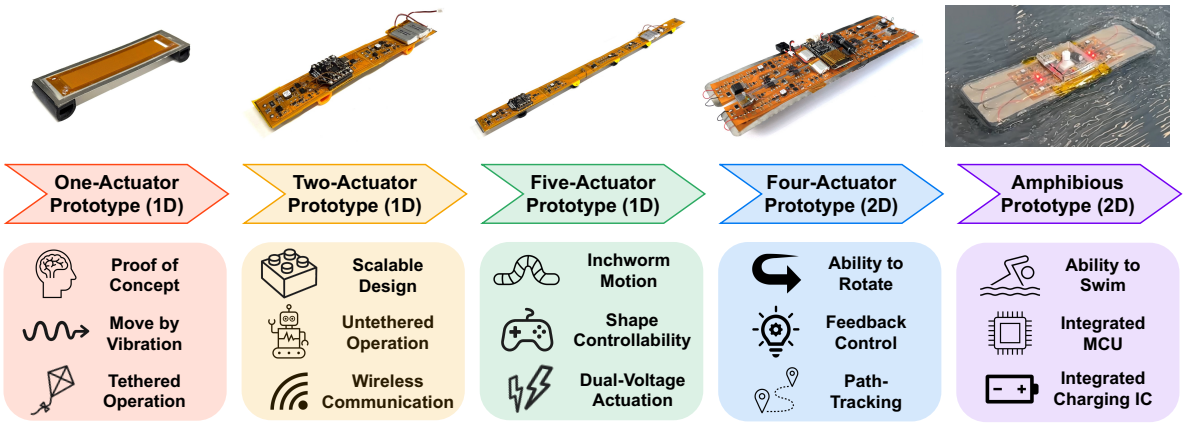

Figure 1.1: Overview of the eViper research platform and the highlighted features of various prototype designs.

- Designed and implemented the eViper soft robotic platform that integrates piezoelectric actuators, power electronics, batteries, control, and wireless communication, enabling systematic experimental study of energy-aware piezoelectric mechatronic systems.
- Established an automated data collection framework to record soft robot locomotion under diverse driving conditions, enabling data-driven analysis and modeling of robot behavior.
- Quantitatively characterized actuator-level power consumption and robot-level power-to-velocity conversion efficiency across a wide range of driving waveforms and frequencies.

1.5 Overview of the eViper Research Platform

This thesis introduces extendable Vibrating Intelligent Piezo-Electric Robot (eViper), a scalable research platform for untethered, multi-actuator, multipurpose soft robots. Figure 1.1 illustrates the platform's evolution from one-dimensional (1D) to two-dimensional (2D) configurations. As a proof of concept, a simple one-actuator prototype was first developed, and actuator-induced vibration enabled its locomotion. The second robot [12], incorporated two actuators and was designed to integrate a customized flexible printed circuit board (PCB). The mechanical and electrical building blocks were designed to be modular and scalable, allowing for future integration of additional actuators into the design. This prototype achieved untethered operation and could be controlled remotely. The third prototype [31] featured five actuators connected end-to-end, inspired

by inchworm crawling. To enable greater shape controllability, this robot included two types of actuators requiring different driving voltages.

These 1D soft robots are capable of bidirectional locomotion along their longitudinal axis. However, their rotational motion cannot be effectively controlled. To enable higher control degrees of freedom, a 2D eViper platform was developed by arranging four actuators in an 2×2 array [32]. With this new form factor, the robot is capable of both bidirectional linear motion and bidirectional rotation. Feedback control and path-tracking were successfully implemented on this prototype due to its enhanced locomotion flexibility. To further explore eViper's behavior on different types of surfaces, the robotic structure was waterproofed, enabling it to float and operate on the water surface. This amphibious prototype features an even lighter PCB design through the integration of the microcontroller (MCU) chip and battery-charging IC. Experimental results demonstrate that eViper achieves up to 6.7× higher linear velocities on water than on land. This development opens a new research direction that is introduced in this thesis and will be explored more extensively in future work. The 1D and 2D eViper robots are introduced in detail in Chapters 4 and 5.

1.6 Thesis Organization

This thesis is organized as follows. Chapter 2 introduces the piezoelectric actuator used throughout this research and quantifies its electrical-to-mechanical energy conversion efficiency and aging effects. Chapter 3 describes the architecture of the lightweight, high-voltage power electronics, and analyzes the system power consumption when driving actuators across different waveforms and frequencies. Chapter 4 examines the performance and behavior of the two-actuator soft robot prototype. The actuators in the prototype are aligned along their longitudinal axis, so the system is referred to as "linear 1D robot". Chapter 5 discusses the performance of the four-actuator and amphibious soft robot prototypes. The actuators are arranged in a 2x2 array; therefore, these systems are referred to as "planar 2D robots". Because planar robots have higher controllability than linear robots, data-driven modeling, locomotion noise, and feedback control are also covered in this chapter. Finally, Chapter 6 concludes this thesis.

2

Characterization of Piezoelectric Actuators

This chapter is based on work published in the following papers:

- *H. Cheng, Z. Zheng, P. Kumar, Y. Chen and M. Chen, "Hybrid-SoRo: Hybrid Switched Capacitor Power Management Architecture for Multi-Channel Piezoelectric Soft Robot," 2022 IEEE Applied Power Electronics Conference and Exposition (APEC).*

- *Z. Zheng, P. Kumar, Y. Chen, H. Cheng, S. Wagner, M. Chen, N. Verma and J. C. Sturm, "Piezoelectric Soft Robot Inchworm Motion by Tuning Ground Friction Through Robot Shape: Quasi-Static Modeling and Experimental Validation," in IEEE Transactions on Robotics, vol. 40, pp. 2339-2356, 2024.*

2.1 Chapter Introduction

This chapter characterizes Macro Fiber Composite (MFC) devices, a class of piezoelectric actuators, that are utilized in all eViper robotic prototypes. Section 2.2 describes the basic properties of MFC devices. Section 2.3 introduces the deformation behavior of steel-bonded MFC devices. Section 2.4 analyzes an actuator's energy utilization via voltage-charge (V-Q) loop measurements. Section 2.5 discusses the equivalent circuit model of a piezoelectric actuator and the induced current generated during actuator deformation. Section 2.6 assesses the time-dependent behavioral variation of the actuators. Finally, Section 2.7 summarizes this chapter.

2.2 Macro Fiber Composite (MFC) Devices

The piezoelectric actuators used in this research are Macro Fiber Composite (MFC) devices manufactured by Smart Material Corporation [33]. These planar, low-profile actuators contain rectangular piezoelectric ceramic rods that can deform or distort depending on the spatial arrangement of the rods and electrodes. Specifically, the robot prototypes in this research uses M-8514-P1 and M-8514-P2 MFC devices, as shown in Fig. 2.1. The number "8514" stands for the dimension of the active region containing piezoelectric ceramic rods (85 mm long, 14 mm wide). After necessary packaging and the addition of external electrodes, each actuator is 100 mm long, 20 mm wide, and weighs approximately 2 g. P1 MFCs are "elongators", meaning that their length increases if

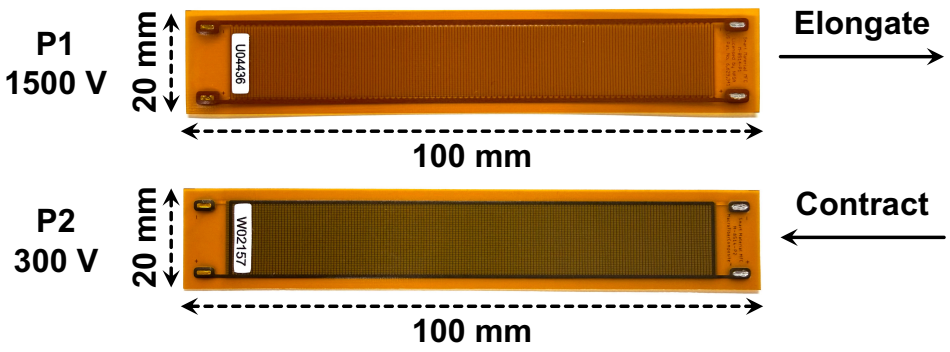

Figure 2.1: Photos of P1 and P2 MFC devices. The maximum driving voltage, dimension, and deformation characteristics under positive applied voltage are labeled.

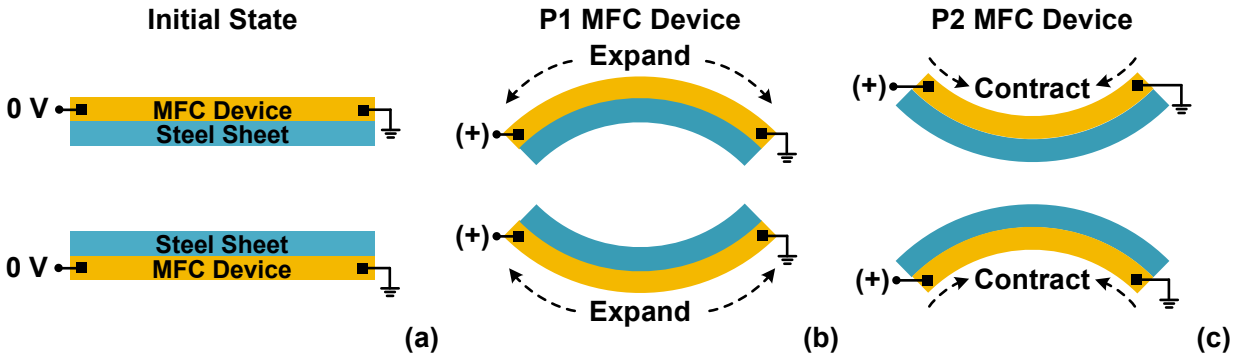

Figure 2.2: Illustration of the operating principles of steel-bonded MFC devices. Mounting the MFC layer on either the upper or lower surface of the steel sheet (top and bottom row of the figure) results in different bending directions. (a) The actuator is flat when with no applied voltage. Applying a positive voltage to (b) the P1 MFC and (c) the P2 MFC cause them to deform and bend the structure in opposite directions.

a positive voltage is applied across the terminals. On the other hand, P2 MFCs are "contractors" whose length decreases with positive applied voltage. The maximum operational positive voltage is 1500 V for P1 MFCs and 360 V for P2 MFCs.

2.3 Basic Operation of Steel-Bonded Piezoelectric Actuators

Fig. 2.2 is an illustration showing the basic operation principles of steel-bonded piezoelectric actuators. In this thesis, MFC devices are always bonded to a 50-μm-thick stainless steel sheet. The Young's modulus is 30 GPa for the MFC devices and 190 GPa for the steel sheet. A higher Young's modulus indicates that the steel sheet has much higher resistance to axial deformation. Therefore, when a positive voltage is applied across a P1 MFC device, it tries to lengthen, but the whole structure bends toward the opposite side of the MFC due to the high elongation stiffness of the

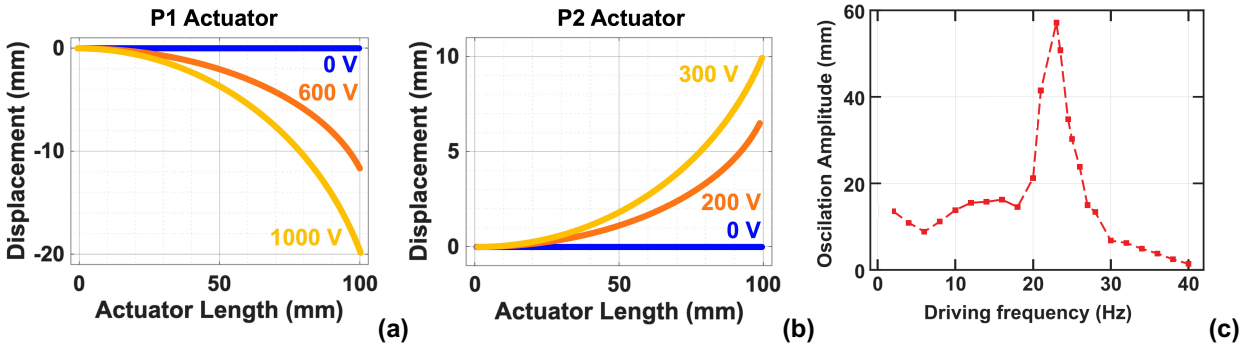

Figure 2.3: Bending displacement for (a) P1 and (b) P2 actuators across their length when different static voltage is applied. (c) The dynamic response of a P1 actuator when driven by 1000 V sine wave across various frequencies. Figures recreated from [20]. The actuator oscillates with the highest amplitude at around 23 Hz.

steel sheet. The same principle applies to P2 actuators. P2 devices tries to contract when applied a positive voltage, but the whole structure bends toward the same side of the MFC. Fig. 2.2 includes two possible bending scenarios for both P1 and P2 actuators. Whether the steel-bonded structure bends concave up or down not only depends on the type of MFC devices, but also the arrangement of the two material layers.

Fig. 2.3(a) and Fig. 2.3(b) show the bending displacement of P1 and P2 actuators when different static voltage is applied. The bending direction follows the convention that the MFC device is attached on top of the steel sheet (refer to Fig. 2.2). P1 actuators bend concave down 20 mm when 1000 V is applied. P2 actuators bend concave up 10 mm when 300 V is applied. Fig. 2.3(c) shows the dynamic response of a P1 actuator, measured with a cantilever experiment, when driven by 1000 V_{pp} sine wave. The resonant frequency is 23 Hz.

2.4 V-Q Loop of Actuators with Various Driving Waveforms

Piezoelectric actuators exhibit hysteresis behavior between applied voltage and accumulated electric charge, particularly under large-signal operation employed in this research. Measuring the voltage-charge (V-Q) loops provides a direct evaluation of the energy usage in the actuator, including the peak stored energy and the net energy consumed by the actuator per operating cycle. It also allows us to compare actuator properties across different driving waveforms and frequencies. In a V-Q loop, the total input electrical energy per cycle $E_{tot,\,act}$ is approximately equal to the maximum

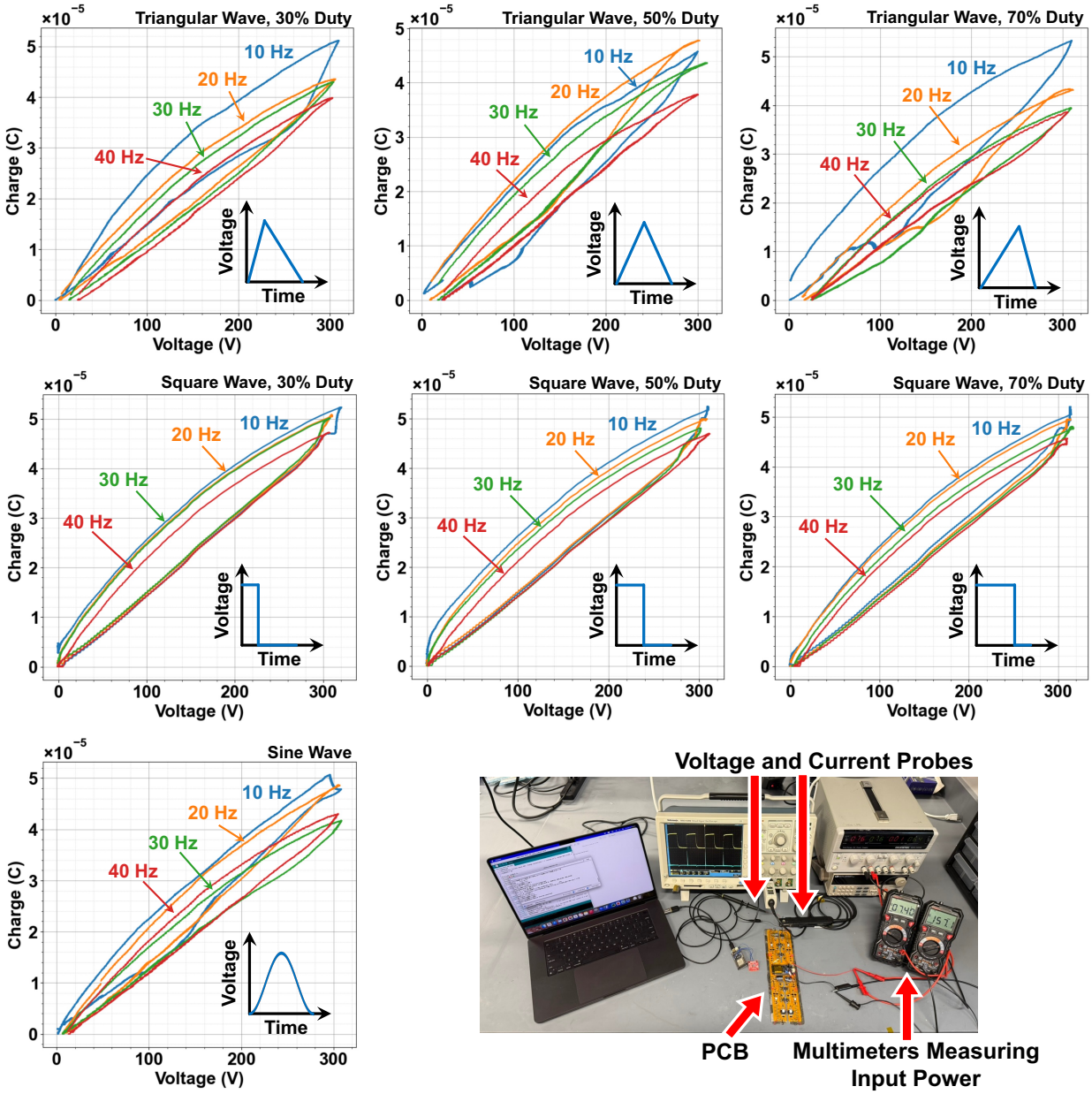

Figure 2.4: Measured V-Q loops for a piezoelectric actuator across various frequencies and driving waveforms. The experimental setup is captured in the bottom-right photo.

Table 2.1: Energy consumed by actuator per cycle ($E_{net,\,act}$), maximum stored energy ($E_{stored,max}$), and energy transfer efficiency from driving electronics to actuator (η_{act}) for different excitation waveforms from 10 Hz to 40 Hz. All energy values are expressed in millijoules (mJ).

Waveform	Parameter	10 Hz	20 Hz	30 Hz	40 Hz
Tri_30%	$E_{net,\,act}[mJ]$	2.25 ± 0.40	1.59 ± 0.29	1.43 ± 0.35	1.11 ± 0.24
	$E_{stored,\,max}[mJ]$	8.33 ± 0.62	7.34 ± 0.24	6.91 ± 0.57	6.40 ± 0.21
	$\eta_{act}[\%]$	27.0 ± 5.2	21.7 ± 4.0	20.7 ± 5.3	17.3 ± 3.8
Tri_50%	$E_{net,\,act}[mJ]$	2.08 ± 0.52	1.30 ± 0.49	1.10 ± 0.47	1.19 ± 0.49
	$E_{stored,\,max}[mJ]$	7.87 ± 0.01	6.82 ± 0.59	6.70 ± 0.44	6.86 ± 0.50
	$\eta_{act}[\%]$	26.4 ± 6.6	19.1 ± 7.4	16.4 ± 7.1	17.4 ± 7.3
Tri_70%	$E_{net,\,act}[mJ]$	1.51 ± 0.15	1.33 ± 0.52	1.27 ± 0.40	1.19 ± 0.33
	$E_{stored,\,max}[mJ]$	7.35 ± 0.31	7.16 ± 0.28	6.77 ± 0.38	6.68 ± 0.29
	$\eta_{act}[\%]$	20.6 ± 2.2	18.6 ± 7.3	18.8 ± 6.0	17.8 ± 5.0
Sine	$E_{net,\,act}[mJ]$	1.67 ± 0.21	1.36 ± 0.33	1.01 ± 0.21	1.33 ± 0.37
	$E_{stored,\,max}[mJ]$	8.09 ± 0.26	7.32 ± 0.34	6.78 ± 0.18	7.06 ± 0.46
	$\eta_{act}[\%]$	20.7 ± 2.7	18.6 ± 4.6	14.9 ± 3.1	18.8 ± 5.4
Squ_30%	$E_{net,\,act}[mJ]$	2.45 ± 0.48	1.95 ± 0.35	1.93 ± 0.32	1.84 ± 0.27
	$E_{stored,\,max}[mJ]$	8.86 ± 0.27	7.90 ± 0.36	7.76 ± 0.32	7.64 ± 0.27
	$\eta_{act}[\%]$	27.7 ± 5.5	24.7 ± 4.6	24.9 ± 4.2	24.1 ± 3.6
Squ_50%	$E_{net,\,act}[mJ]$	2.71 ± 0.23	2.23 ± 0.39	2.01 ± 0.37	1.95 ± 0.36
	$E_{stored,\,max}[mJ]$	8.65 ± 0.35	8.02 ± 0.37	7.55 ± 0.37	7.84 ± 0.37
	$\eta_{act}[\%]$	31.3 ± 2.9	27.8 ± 5.0	26.6 ± 5.1	24.9 ± 4.7
Squ_70%	$E_{net,\,act}[mJ]$	2.41 ± 0.09	2.15 ± 0.40	2.02 ± 0.37	1.83 ± 0.33
	$E_{stored,\,max}[mJ]$	8.84 ± 0.08	8.27 ± 0.43	8.23 ± 0.23	7.74 ± 0.32
	$\eta_{act}[\%]$	27.3 ± 1.0	26.0 ± 5.0	24.5 ± 4.5	23.6 ± 4.4

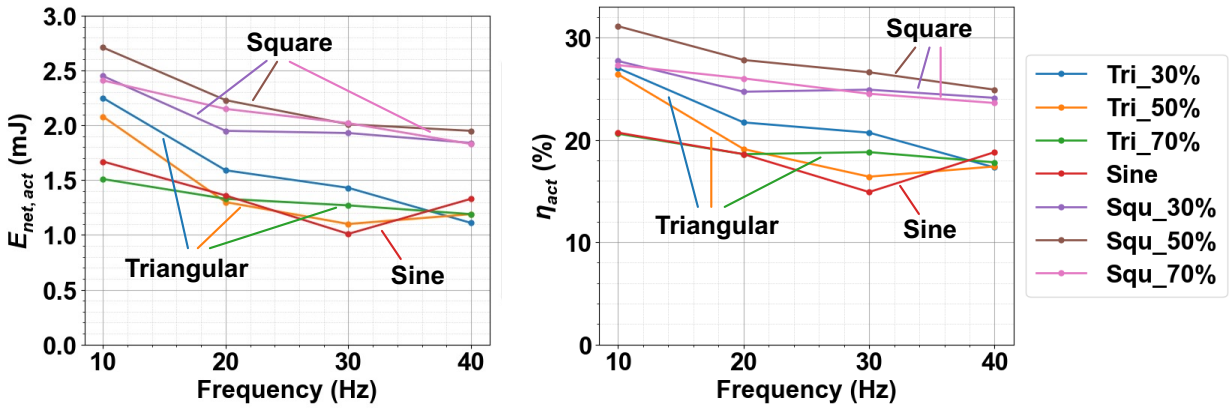

Figure 2.5: Plots of $E_{net,\,act}$ and η_{act} across various different waveforms and frequencies.

stored energy $E_{stored,\,max}$ of the piezoelectric actuator:

$$E_{tot,\,act} = \int_{charging} V\,dQ \approx E_{stored,\,max} = \int_0^{Q_{max}} V(Q)\,dQ \tag{2.1}$$

The net electrical energy consumed by the actuator per operating cycle, $E_{net,\,act}$, is the area enclosed by the V-Q hysteresis loop:

$$E_{net,\,act} = \oint V\,dQ \tag{2.2}$$

$E_{net,\,act}$ can be decomposed into two components: the mechanical output work E_{mech} and the energy dissipated as heat due to internal material loss $E_{heat,\,act}$. Namely:

$$E_{net,\,act} = E_{mech} + E_{heat,\,act} \tag{2.3}$$

The main contributors of the internal loss are related to material properties, including (1) domain wall hysteresis, (2) dielectric loss, (3) mechanical loss, and (4) leakage current. A detailed introduction to the loss mechanism can be found in previous literature [34, 35]. The energy transfer efficiency from driving electronics to actuator, η_{act}, denotes the fraction of the electrical energy delivered to the actuator that is absorbed by the actuator. η_{act} is defined as:

$$\eta_{act} = \frac{E_{net,\,act}}{E_{stored,\,max}} \tag{2.4}$$

The V-Q loops of the actuators are measured across various representative waveforms at 10, 20, 30, and 40 Hz operating frequencies. The results are presented in Figs. 2.4 and 2.5 (Squ: Square Wave; Sine: Sinusoidal Wave; Tri: Triangular Wave, with different duty ratios labeled as %). Table 2.1 shows the numbers of $E_{net,\,act}$, $E_{stored,\,max}$, and η_{act}. Based on Fig. 2.5, square waves have higher $E_{net,\,act}$ and η_{act}, while the numbers are lower for sine waves and triangular waves. η_{act} approximately lies in the range from 15% to 30%. During the experiment, the voltage and current waveforms at the output ports of the driving electronics (input ports of the actuator) were measured. The current waveforms were integrated over time to obtain the charge. The actuator was driven in the air and does not have net displacement. The experimental setup cannot isolate E_{mech} or $E_{heat,\,act}$ from the reported $E_{net,\,act}$. Small cycle-to-cycle variation of the V-Q loops is observed in the measurement. This might arise from noises in the voltage/current measurement equipment and the limitation of the control bandwidth and timing precision of the MCU.

2.5 Electrical Modeling and Actuator-Induced Current

A piezoelectric actuator converts energy bidirectionally between the electrical and mechanical domains. It can be modeled as an equivalent electrical circuit to facilitate discussion of its response under electrical excitation. Fig. 2.6 shows the equivalent circuit model of a piezoelectric actuator. Mechanical deformation induces an electrical current, which flows through the actuator's internal impedance and results in a measurable terminal voltage. From an electrical modeling perspective, this behavior is represented by an ac current source [36, 37], denoted as i_p in the figure. The

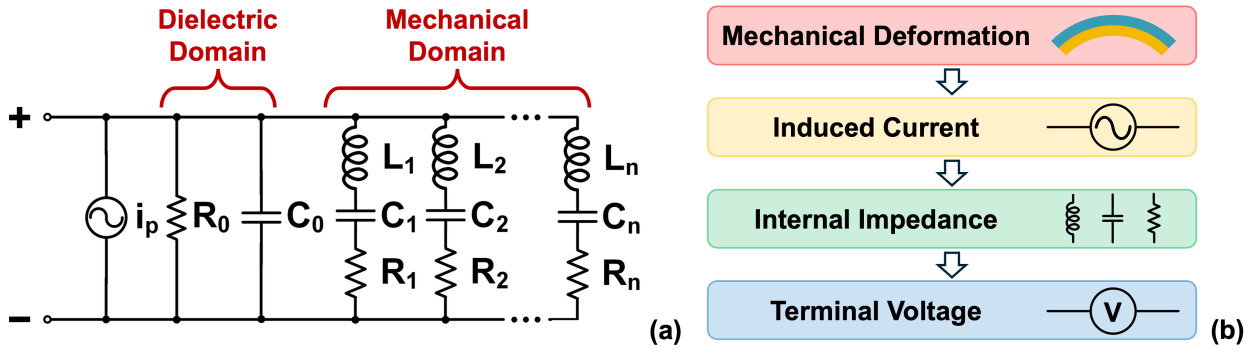

Figure 2.6: (a) Electrical equivalent circuit model of a piezoelectric actuator. (b) Conceptual diagram illustrating how mechanical deformation induces a current that flows through the internal impedance and results in a terminal voltage.

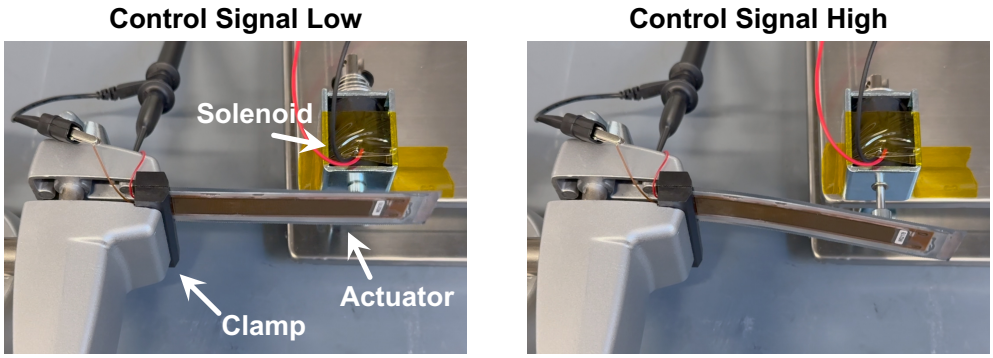

Figure 2.7: Experimental setup for measuring motion-dependent terminal voltage. The solenoid pushes the actuator when the control signal is high. The actuator terminals are connected to an oscilloscope.

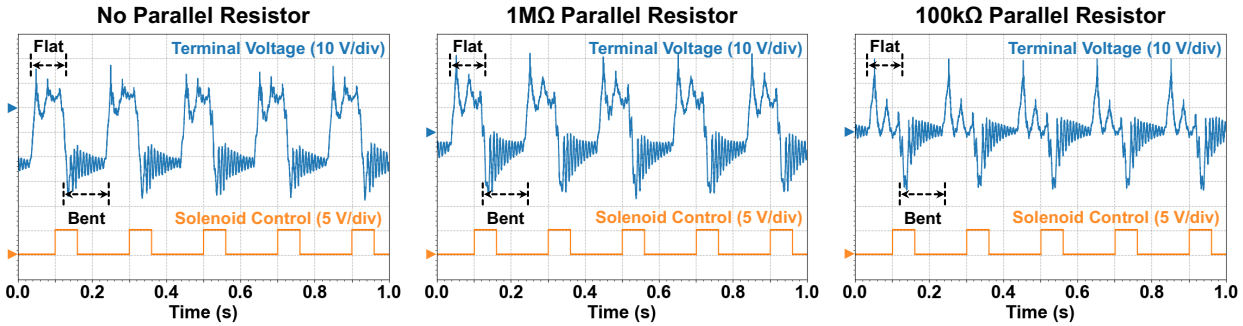

Figure 2.8: Measured actuator terminal voltage driven by a solenoid with different parallel resistors. Due to the slow mechanical response of the solenoid, the terminal voltage appears asynchronous with the solenoid control signal.

polarity of the current, and consequently the polarity of the terminal voltage, is determined by the direction of mechanical deformation. The induced current reverses sign when the actuator bends upward versus downward, or when it switches between bending and release. The elements R_0 and C_0 represent the dielectric properties and losses of the actuator. The multiple LCR branches correspond to different mechanical resonance modes [38, 39].

To estimate the magnitude of the motion-dependent terminal voltage during robotic operation, a solenoid was used to mechanically excite an actuator whose terminals were connected to an oscilloscope. Fig. 2.7 illustrates the experimental setup. A digital signal controls the solenoid. When the signal is low, the solenoid is in the default state and the actuator is flat. When the signal is high, the solenoid pushes the actuator, causing it to bend. Fig. 2.8 shows the measured waveforms. In this experiment, the solenoid was operated at 5 Hz. Different external resistors were connected in parallel with the actuator's terminals to simulate interfacing with an external power converter.

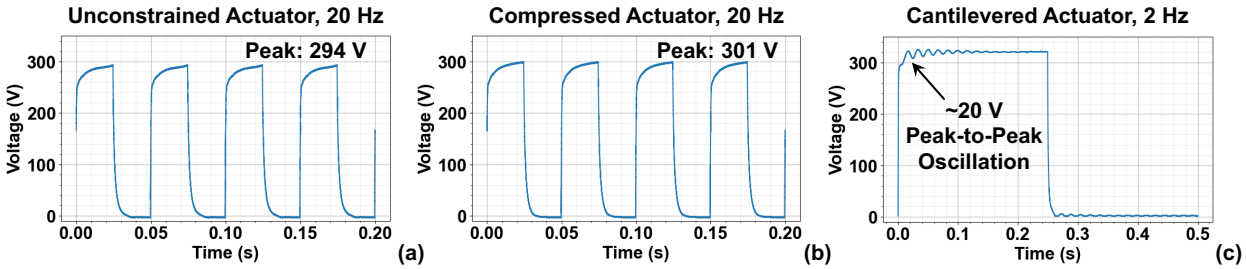

Figure 2.9: Measured actuator terminal voltage under 300 V driving square wave when the actuator is (a) placed on a table and allowed to bend freely, and (b) mechanically constrained by placing a book on top of it. (c) Measured step response of a cantilevered actuator under 300 V driving square wave.

The intervals when the actuator is pushed and released (marked as "Bent" and "Flat") are labeled in the figures. It is observed that the actuator's terminal voltage is negative when the actuator is bent and positive when it is released. When a resistor is connected, the negative and positive voltage peaks are approximately -25 V and 30 V, respectively, and an RC-type voltage decay is observed in the envelope of the measured waveforms.

When a piezoelectric actuator is driven by an external power converter, the actuator bends under a positive applied voltage. However, in the previous experiment, a negative terminal voltage is measured on a bent actuator. This indicates that as an external power source tries to charge an actuator, the actuator's induced current may counteract the charging current, resulting in a reduced terminal voltage. Fig. 2.9 shows multiple waveforms when an actuator is driven by a 300 V square wave. In Fig. 2.9(a), the actuator is placed on a table and can bend normally. In contrast, the actuator in Fig. 2.9(b) is mechanically constrained by placing a book on top of it. Under identical electrical excitation, the measured terminal voltage in Fig. 2.9(b) is approximately 7 V higher. This observation is consistent with the earlier result: reduced mechanical deformation leads to a smaller induced current, allowing the external source to charge the actuator more effectively.

Fig. 2.9(c) demonstrates the step response of an actuator in a cantilevered configuration, where one end is clamped and the other end can oscillate freely. After the sharp charging and discharging transitions, mechanical vibrations of the actuator appear as voltage oscillations in the measured waveform. This indicates that the actuator's self-induced current, and its resulting terminal voltage, can directly influence the applied driving voltage. However, these voltage oscillations are not

observed when the actuator is integrated into a soft robot because the printed circuit board (PCB) and robotic feet mechanically damp the actuator vibrations.

2.6 Variation in Actuator Characteristics

The robot prototypes in the eViper platform contain multiple piezoelectric actuators. Differences in their electromechanical responses to driving signals and their long-term stability will directly translate to eViper's behavioral consistency. To quantify variations in actuator performance over time, prolonged cantilever tests were conducted on three actuator samples to measure changes in oscillation amplitude. Although the cantilever configuration differs from the operating conditions of eViper, it provides a valuable reference for analyzing discrepancies and changes in actuator behavior. The samples were operated at 23 Hz, which is their resonant frequency according to a previous study [20]. The peak-to-peak oscillation amplitude was recorded using the slow-motion video mode (240 frames per second) of a GoPro HERO12 camera at ten-minute intervals. The results are shown in Fig. 2.10. Significant degradation in vibration amplitude was observed on all three actuator samples, indicating that the time-dependent characteristics need to be taken into consideration when operating soft robots for extended period of time. Different initial bending amplitude and lifetime across actuators were also observed in Fig. 2.10, the reasons for which can be attributed to:

- Sample-to-sample variation of actuators [40].
- Nonuniform application of epoxy during the manual bonding of steel sheet and actuators, leading to variations in adhesive layer thickness [41, 42].
- Electrical fatigue of piezoelectric materials, which reduces the bending responsiveness to electrical driving signals [43, 44].

The above factors highlight a challenge in operating a multi-actuator soft robot: the inherent complexity of the system. The complexity could come from different initial bending amplitude or

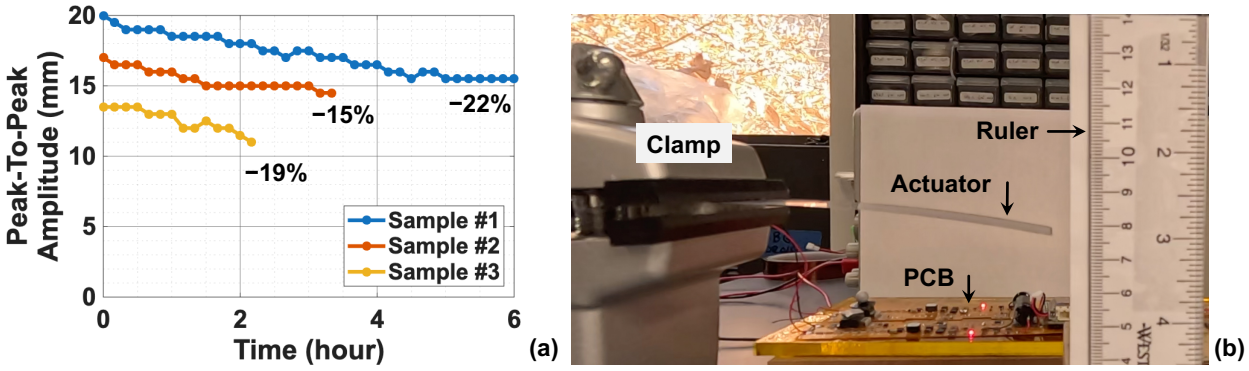

Figure 2.10: (a) The time variation of the peak-to-peak oscillation amplitude of three piezoelectric actuator samples during a cantilever experiment. The label at the end of each line indicates the percentage degradation of each actuator. (b) Experimental setup showing a cantilevered actuator, a ruler, and a driver PCB. The ruler is placed beside the actuator to determine the bending amplitude.

unbalanced rate of degradation, and it leads to non-ideal drift during robot operation. Methods to compensate the non-ideal behavior will be discussed in Chapter 5.

2.7 Chapter Summary

This chapter introduced the fundamental physical, electrical, and mechanical characteristics of the steel-bonded MFC devices. The V–Q loops were measured across different waveforms and frequencies to quantify how actuator energy utilization changes with driving conditions. The induced current and the resulting terminal voltage in a bent actuator were examined, and it was found that they can counteract the external power source during operation. Finally, actuator aging effects and lifetime were investigated, motivating the development of control strategies to regulate the behavior of actuators and the entire piezoelectric mechatronic system.

3

Driver Circuits and Power Architecture

This chapter is based on work published in the following papers:

- *H. Cheng, Z. Zheng, P. Kumar, Y. Chen and M. Chen, "Hybrid-SoRo: Hybrid Switched Capacitor Power Management Architecture for Multi-Channel Piezoelectric Soft Robot," 2022 IEEE Applied Power Electronics Conference and Exposition (APEC)*
- *H. Cheng et al., "A Flexible Lightweight 7.4 V Input 300 V to 1500 V Output Power Converter for an Untethered Modular Piezoelectric Soft Robot," 2023 IEEE 24th Workshop on Control and Modeling for Power Electronics (COMPEL)*

3.1 Chapter Introduction

This chapter details the design and implementation of the power circuits that enable efficient high-voltage generation and control for multi-actuator piezoelectric soft robots. System-level power flow analysis is also conducted to quantify energy required for actuation and support energy-aware control strategies. Section 3.2 reviews the properties desired for power electronics in a piezoelectric mechatronic system and topologies for building high-voltage converters. Section 3.3 introduces the implemented high-voltage power converter in this research. Section 3.4 compares centralized and distributed power delivery strategies for scalable actuation, and Section 3.5 presents the circuit topologies for both architectures. Section 3.6 demonstrates the experimental performance of the prototype systems. Section 3.7 explains the method used to synthesize customized actuator waveforms. Section 3.8 quantifies the total required power when driving an actuator with various operating conditions, and Section 3.9 investigates the system-level power delivery efficiency. Finally, Section 3.10 summarizes this chapter.

3.2 Power Electronics for Piezoelectric Mechatronic Systems

Piezoelectric mechatronic systems represent a novel application field for power electronics. Ideal power electronics for these systems should possess the following characteristics:

- High-voltage capability. Piezoelectric actuators typically require driving voltages on the order of hundreds to thousands of volts.

- Compact size and low mass. Lightweight and compact circuitry is essential for mobile and autonomous piezoelectric robotic systems.
- High efficiency. High conversion efficiency reduces overall power consumption and allows the use of smaller batteries for a given system and operational requirement.
- Scalability and modularity. Piezoelectric mechatronic systems often integrate multiple actuators that must be controlled independently to achieve better performance. Therefore, a scalable and modular power electronics architecture, with one module per actuator, naturally satisfies this requirement and enables straightforward expansion to larger systems.
- Flexible waveform generation. System performance depends strongly on the driving waveform. The ability to configure driving waveforms enables operation under optimal conditions and improves overall system performance.

A piezoelectric driving circuit is a high-voltage, low-power system. Existing high voltage power electronics can be grouped into two main categories: (1) transformer-based [10, 14, 45–48]; and (2) transformer-less [49–51]. In transformer-based design, the circuit usually consists of an inverter, a transformer, and a voltage rectifier or multiplier. The required voltage gain is contributed by many stages. In a transformer-less architecture, the circuits are composed of a variation of boost converters and a voltage rectifier or multiplier stage. Switched-capacitor circuits are also attractive [50, 51]. We adopt a transformer-based design, because (1) commercial low-power transformers can offer high conversion ratios with low mass ($\sim$0.5 g), ideal for high-voltage, lightweight power converters; (2) this design helps to reduce the switch stress and thus the package size of switches; and (3) it has the potential to achieve high efficiency.

3.3 High Voltage Power Converter Design

Fig. 3.1 shows the schematic of the implemented high-voltage power converter, which includes a full bridge LLC inverter, a transformer, and a Cockcroft–Walton voltage multiplier. Commercial lithium polymer batteries have a nominal output voltage of 3.7 V, and the 7.4 V system input voltage

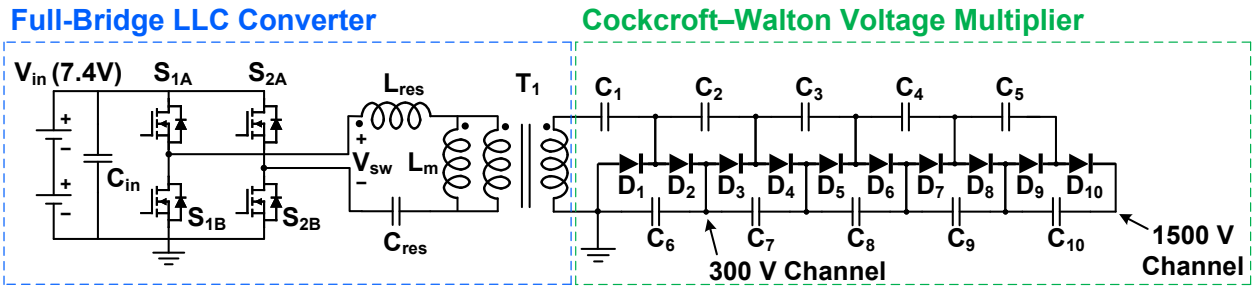

Figure 3.1: Circuit schematic of the implemented high-voltage power converter.

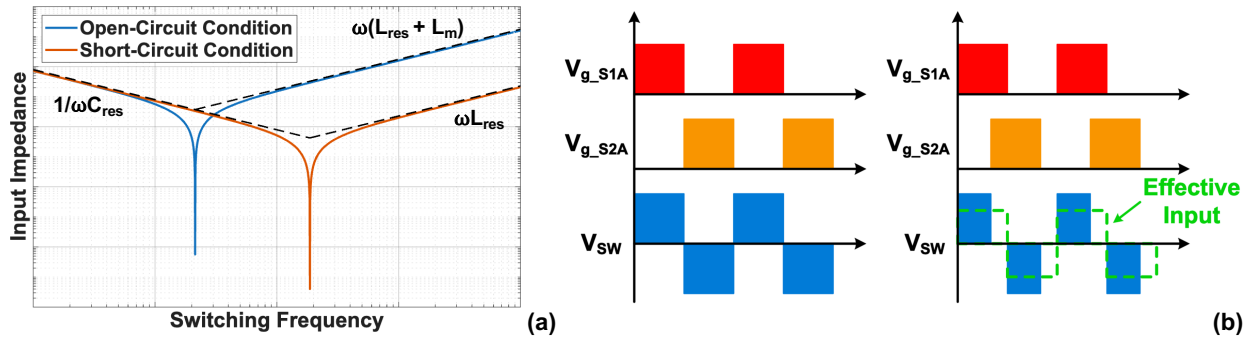

Figure 3.2: Illustration of (a) the dependence of resonant tank input impedance on the converter switching frequency, and (b) phase-shift modulation of the implemented power converter.

V_{in} is obtained by series-connecting two of those batteries. The full-bridge switches (S_{1A}, S_{1B}, S_{2A}, S_{2B}) operates at 50% duty ratio with phase shift. The dc input voltage V_{in} is converted into a bipolar square wave voltage excitation, which can be frequency modulated and phase modulated. This square wave excites the resonant tank, which consists of L_{res}, C_{res}, and the magnetizing inductance of the transformer L_m. The 1:20 transformer steps up the ac voltage and drives the voltage multiplier. Finally, the multiplier rectifies the ac voltage back to dc and linearly extends the voltage level with each multiplier stage. There are 5 levels of multiplier as depicted in Fig. 3.1, with the output of the first stage being 300 V and the output of the fifth stage being 1500 V. With this design, both P1 and P2 types of MFC devices can be strongly actuated.

The overall voltage gain of the LLC converter can be adjusted by either frequency modulation or phase-shift modulation. Fig. 3.2 illustrates the concept of both modulation approaches. Fig. 3.2(a) shows that the input impedance of the resonant tank depends strongly on the switching frequency of the full-bridge active switches. When the switches operate at different frequencies, the input ac voltage waveform to the resonant tank will be attenuated by different scale. Therefore, the input ac

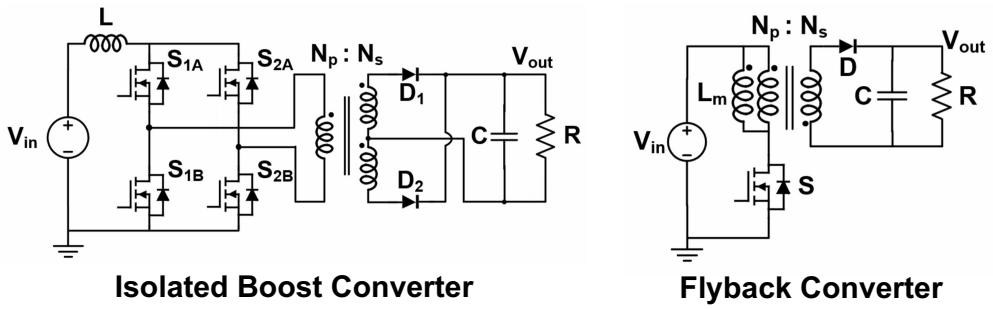

Figure 3.3: Circuit schematics of (a) isolated boost converter and (b) flyback converter.

voltage to the transformer and the resulting output dc voltage can be controlled. This is the concept of frequency modulation. Fig. 3.2(b) depicts the principle of phase-shift modulation. The top two rows draw the gate control signals of switches S_{1A} and S_{2A}, while the third row shows the input ac voltage waveform to the resonant tank V_{sw}. The left column shows the non-phase-shifted waveform, and V_{sw} is bipolar. The right column illustrates the phase-shifted waveform, where switches S_{1A} and S_{2A} are both turned on and off for a small period of time. V_{sw} is 0 V when both switches are on or off. Therefore, V_{sw} becomes a three-level waveform, and the effective input voltage (at the fundamental frequency) seen by the resonant tank is reduced. This way, the output voltage can also be modulated. Note that the control signals of switches S_{1B} and S_{2B} are always out-of-phase with S_{1A} and S_{2A}, respectively, to prevent short circuits from input to electrical ground.

This thesis adopts a full-bridge LLC converter as the high-voltage power converter topology because it offers flexible voltage control and the potential to achieve high power conversion efficiency. Fig. 3.3 presents two other power converter topologies that could be considered, but each of them has drawbacks in the context of piezoelectric mechatronic systems. An isolated boost converter requires a more complicated control sequence for the full-bridge switches. In addition to the conventional two-phase operation, it needs to implement an "all-on" phase, where all four switches are turned on after each traditional phase, to charge the inductor L [52]. This requirement noticeably increases control complexity and places stricter demands on signal timing and synchronization. In a flyback converter, electrical energy is stored in the magnetic core (magnetizing inductance) when the switch S is turned on, and the energy is released when S is turned off. As a result, the converter

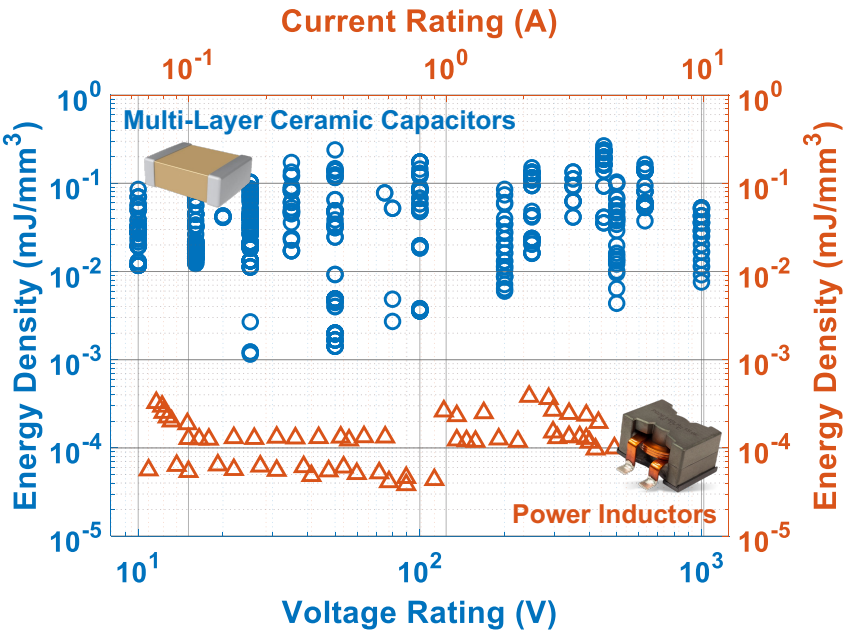

Figure 3.4: Datasheet survey on commercially available multi-layer ceramic capacitors (MLCCs) and power inductors. The blue data points and axes correspond to MLCCs, while the orange ones correspond to power inductors. The energy density of commercial MLCCs is approximately 100 times higher than that of power inductors.

usually needs a larger transformer core due to the higher peak magnetizing current. Complicated control and larger magnetic components are undesirable for the power systems discussed in this thesis because they conflict with the goals of compactness and low mass. Therefore, these converter topologies were not selected.

Fig. 3.4 shows that the energy density of commercial multi-layer ceramic capacitors (MLCCs) is approximately 100$\times$ higher than that of power inductors. This comparison supports the suitability of Cockcroft-Walton voltage multipliers for piezoelectric mechatronic systems because they rely on capacitors rather than bulky magnetic components. As a result, the multipliers offer high energy density while remaining compact and lightweight. Moreover, each stage requires only two diodes and two capacitors, providing a simple and modular approach to interface with actuators that have different voltage requirements.

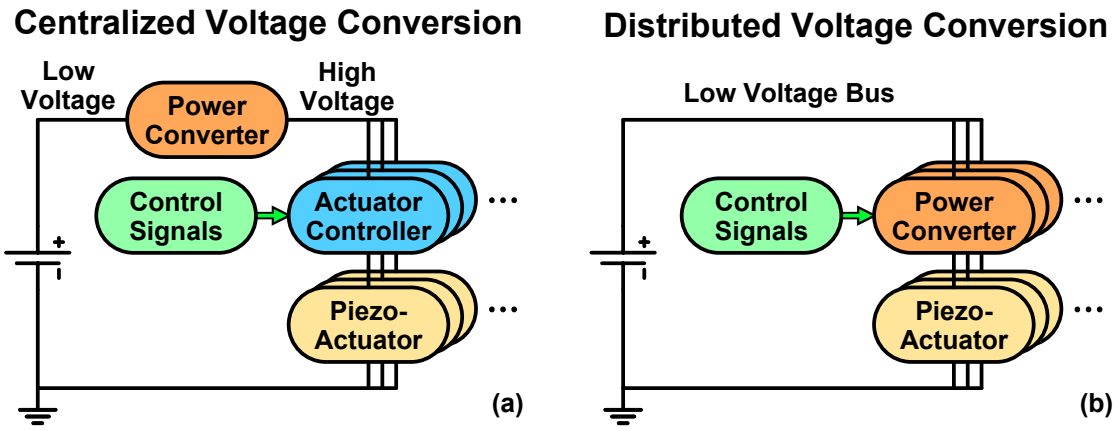

Figure 3.5: Block diagrams of two power delivery architectures: (a) centralized voltage conversion and (b) distributed voltage conversion. In (a), high voltage is generated with a global voltage converter, and then distributed to each actuator controller. In (b), system input voltage is distributed to each voltage converter module, and high voltage is generated locally.

3.4 Centralized and Distributed Voltage Conversion Architectures

A soft robot may contain multiple actuators. The actuators may be controlled independently to achieve the highest degree of freedom in motion control. Therefore, the design of the power circuitry needs to enable distributed power delivery and control. There are primarily two strategies to fulfill this function. Fig. 3.5(a) shows the centralized voltage conversion architecture. In this design, there is one voltage converter and many distributed actuator controllers on the circuit. The voltage converter maintains a global high-voltage rail and delivers high voltage across the circuit. Each distributed actuator controller regulates how the actuator interfaces with the high-voltage rail, depending on the motion control requirements.

On the other hand, Fig. 3.5(b) shows the distributed voltage conversion architecture. In this design, there are many power converter modules, and each of them is responsible for the actuation of a single actuator. Therefore, the system input voltage (battery voltage) is distributed across the circuit, and high voltage is generated locally at each power module. A converter is activated when the actuator requires charging. The converter and actuator discharge simultaneously when commanded by the motion control system.

The above two architectures have distinct strengths and limitations. The centralized architecture reduces the number of high-voltage power converters, resulting in lower overall component

count. However, the load considered in this thesis, piezoelectric actuators, is highly capacitive and draws pulsating current when driven by square waves. Therefore, high-voltage capacitor banks are required to buffer energy and stabilize the high-voltage rail during operation. These high-voltage capacitors are bulky and occupy significant PCB area in practice. Moreover, the active switches in the distributed actuator controllers need to have high voltage ratings, which necessitates the selection of physically larger devices. These factors make the centralized architecture less practical and desirable for piezoelectric mechatronic systems. Nevertheless, this architecture could be highly attractive in other applications. For example, when driving multiple low-voltage DC motors (e.g., four 12 V motors) from a low-voltage battery source (e.g., 3.7 V), the loads are primarily resistive and the required output voltages are much more manageable. In this scenario, energy buffering and switch implementation are significantly simpler, allowing the advantages of reduced converter count to become more prominent.

On the other hand, the distributed architecture has a higher overall component count due to the use of multiple onboard converter modules. However, only low-voltage capacitor banks are needed to buffer battery-level input voltage, which is more space-efficient than high-voltage energy storage. In addition, fewer high-voltage switches are required per actuator since the voltage conversion is localized within each module. Therefore, the distributed architecture results in a more compact PCB design for piezoelectric mechatronic systems, and it is adopted in more recent eViper robots, including the four-actuator and amphibious prototypes introduced in Fig. 1.1. In the following sections, schematics and prototypes of both architectures are presented and discussed.

3.5 Schematics for Power Delivery Architectures

This section introduces the circuit schematics to implement both power delivery architectures.

3.5.1 Centralized Voltage Conversion

Figure 3.6 shows the circuit topology of the centralized voltage conversion architecture with a full bridge LLC inverter, a Cockcroft–Walton voltage multiplier, and distributed actuator controllers. The top half of the figure is the same as the high-voltage power converter introduced in section 3.3.

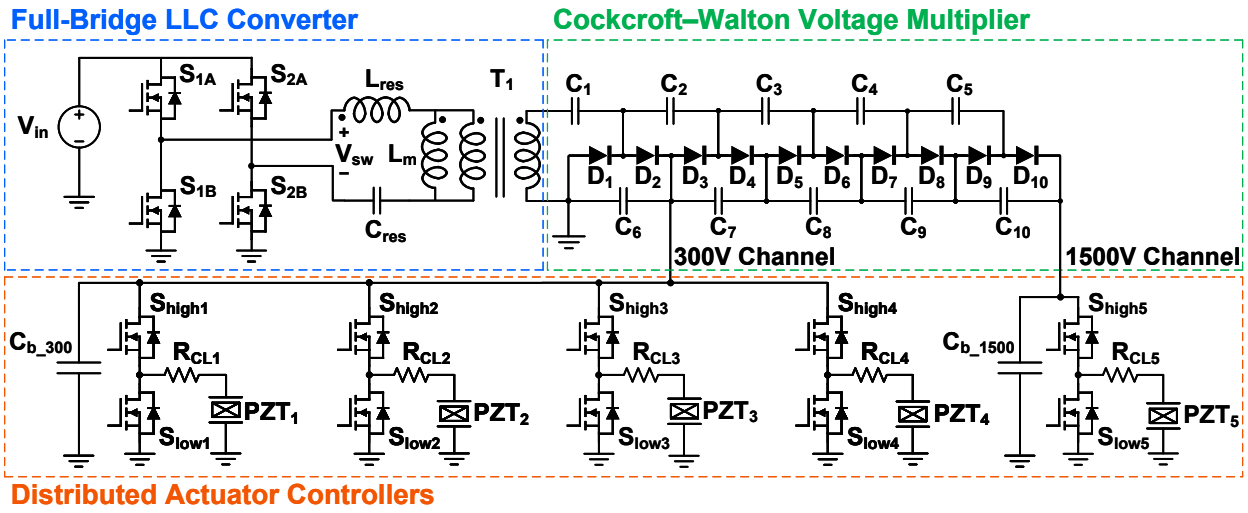

Figure 3.6: Schematic of an example centralized voltage conversion architecture containing an LLC converter, Cockcroft-Walton voltage multiplier, and five distributed actuator controllers (DACs). The multiplier stage count and the arrangement of the DAC connections can be altered based on the need of different robot design.

The multiplier and the distributed actuator controllers are designed to be scalable and modular. The dc nodes in the Cockcroft–Walton voltage multiplier ($C_6 - C_{10}$) function as the input of the controllers, and each node is able to serve as the voltage source of multiple controllers. The multiplier structure can also be further extended if higher voltage is desirable. In the implementation of Fig. 3.6, the multiplier can provide five linearly-spaced voltage levels to drive actuators, and two of them are utilized. The actuator controller modules can also be connected to other channels of the multiplier depending on specific actuator requirements.

The distributed actuator controllers should be designed to meet the functional requirements of the actuators, such as ramp-up rate, ramp-down rate, driving voltage polarity, and the requirements of energy recycling. As discussed in Section 2.5, piezoelectric actuators can be modeled as an RLC network, and the capacitor C_0 usually dominates the behavior. Depending on the actuator area and the required driving voltage, the capacitance values are different and should be considered in circuit design. Figure 3.7 shows four possible implementations of the controllers. Unipolar ones are designed to drive piezoelectric actuators that only need unipolar voltage. Bipolar counterparts are designed for actuators which may need bipolar voltage. Resistive controllers excite the actuator without recycling the energy stored in the actuators, and inductive ones can recycle part of the

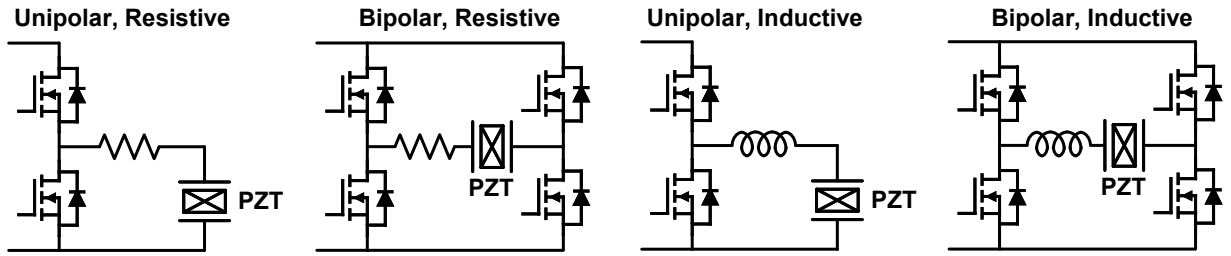

Figure 3.7: Four distributed actuator controller designs categorized by driving polarity and dominant passive element.

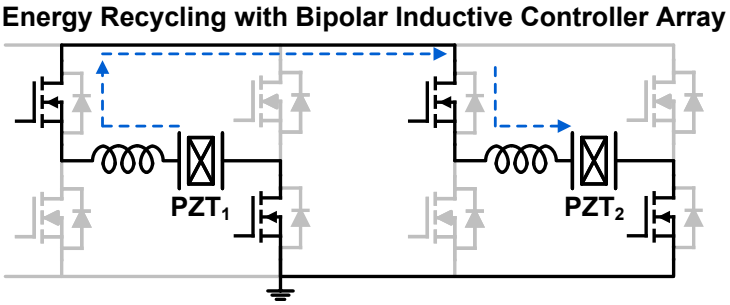

Figure 3.8: Conceptual illustration of a pre-charged PZT_1 charges PZT_2 by using a bipolar inductive controller array.

energy stored in the actuators with more sophisticated control. Figure 3.8 shows a conceptual illustration of using an actuator to charge another through a bipolar inductive controller array. Since the actuators in a soft robot are usually activated in sequence and operate in cycles, this operation may improve the energy efficiency of the system.

The proposed architecture is highly flexible and modular. In Fig. 3.6, each controller can interface with an arbitrary voltage levels on the multiplier. The capacitors in parallel with the DACs, C_{b_300} and C_{b_1500}, are the high-voltage capacitor banks required to buffer energy for the high voltage rails. When S_{highX} is ON and S_{lowX} is OFF, the actuator (a capacitive load) is charged and demands a pulsed current that causes a transient voltage droop on C_X and the capacitor banks. The voltage on the multiplier is temporarily pulled down, and the capacitor banks need to be large enough to ensure the PZTs reach sufficient voltage levels fast enough. When S_{lowX} is ON and S_{highX} is OFF, the actuator is discharged via R_{CLX}. Current limiting resistors R_{CLX} are placed in each controller to suppress the peak current and control the charging/discharging time of PZT_X. In this thesis, only resistive controllers are implemented. Inductive controllers are buck converters with voltage regulation and waveform generation capabilities. They require more sophisticated

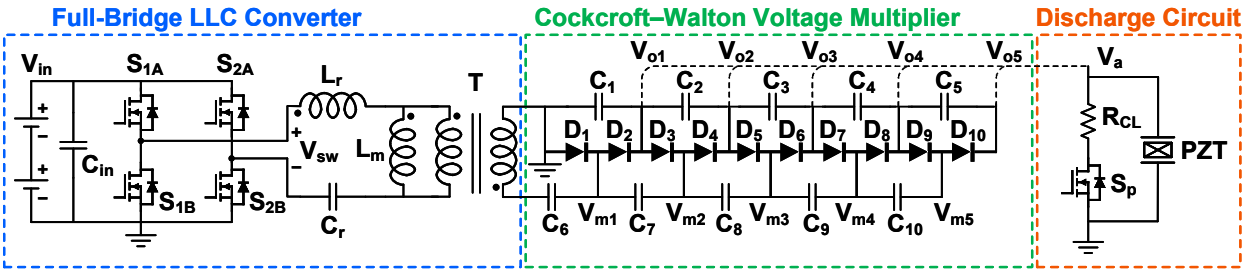

Figure 3.9: Schematic of the implemented distributed voltage conversion architecture. The load actuator can be connected to any multiplier output (V_{o1} to V_{o5}) depending on its actuation requirements.

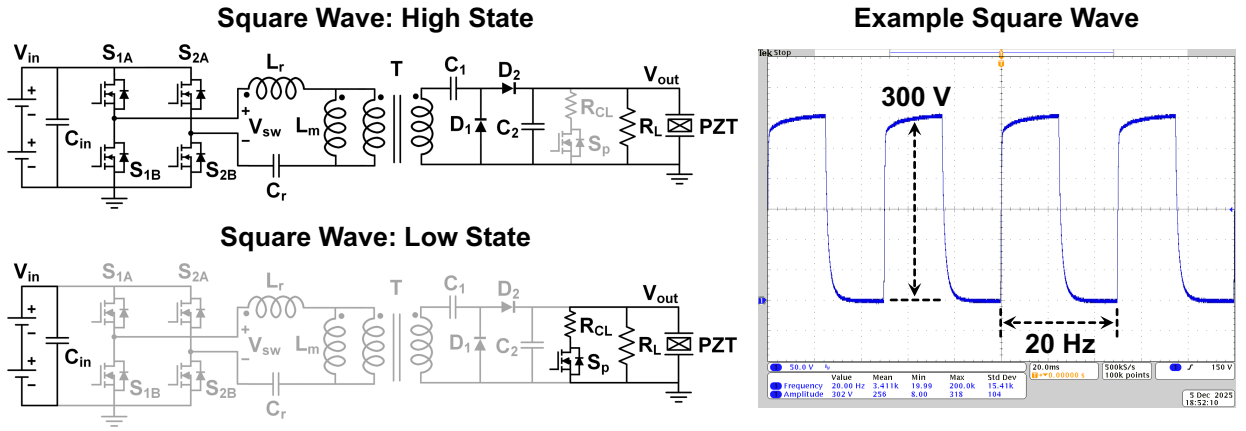

Figure 3.10: Schematics showing the two operational states of the circuit when generating square waves. The grayed-out circuit is deactivated. The right half of this figure demonstrates a 20 Hz, 50% duty ratio high-voltage square wave generated by the converter. The waveform has slower edges due to the limited current capability of the power circuit.

control circuitry and heavier magnetic components. Therefore, they are not selected in this design.

3.5.2 Distributed Voltage Conversion

In a distributed voltage conversion architecture, there are multiple power converter modules on the prototype PCB. Each module has the high-voltage power converter of Section 3.3 followed by a discharge circuit containing a current-limiting resistor and an active switch. Fig. 3.9 shows the circuit schematic of a single module. Each module is responsible for the actuation of a single actuator, therefore, the required number of modules would be equal to the number of actuators in a soft robot. Since the voltage converter directly interfaces with the actuator, the circuit and the actuator discharge together when the microcontroller requires the actuator to discharge. The stage count of the voltage multiplier is determined by actuator characteristics.

In this architecture, high-voltage output square waves are generated by controlling the LLC

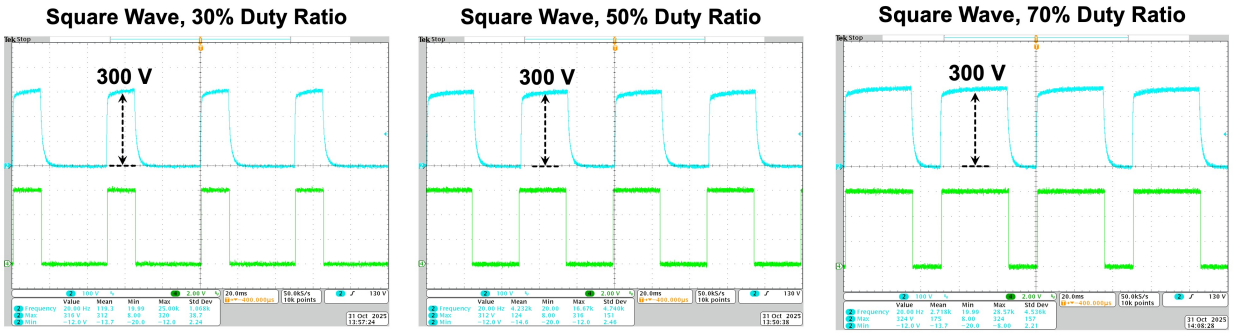

Figure 3.11: Square waves with different duty ratios. The blue waveforms are generated by the power converter, while the green ones are generated by an external signal generator to provide a reference for waveform ideality.

converter and the discharge circuit in a complementary way. When the actuator needs to be charged, the switches in the LLC converter operates normally and the switch S_p in the discharge circuit is turned off. When the actuator needs to be discharged, the gates of all LLC full-bridge switches are pulled low, and S_p is turned on, so the load discharges through R_{CL}. An illustration of this process is presented in Fig. 3.10. The frequency, duty ratio, and voltage amplitude of square waves are control variables. Fig. 3.11 shows several 20 Hz square waves with different duty ratios. The rise time is approximately 1 ms and the fall time is about 3 ms. The fall time can be shortened by reducing the value of R_{CL}, but the rise time presents a system limitation of the current circuit topology. With a more sophisticated control scheme, this circuit is also capable of generating triangular and sine waves, and the details will be presented in Section 3.7.

3.6 Prototypes and Power Efficiency

This section reports the design, layout, and dc-dc power efficiency of the PCB prototypes.

3.6.1 PCB Design and Layout

There are multiple prototypes of eViper that has been constructed and researched. Fig. 3.12 shows four different PCB designs that corresponds to three versions of the robot, and the dimensions of each design are labeled.

In the two-actuator prototype, a distributed voltage conversion architecture was adopted. There are two power converter modules, batteries, and a microcontroller (MCU) on board. Common battery options that have compact form factor include coin batteries and lithium-polymer (Li-Po)

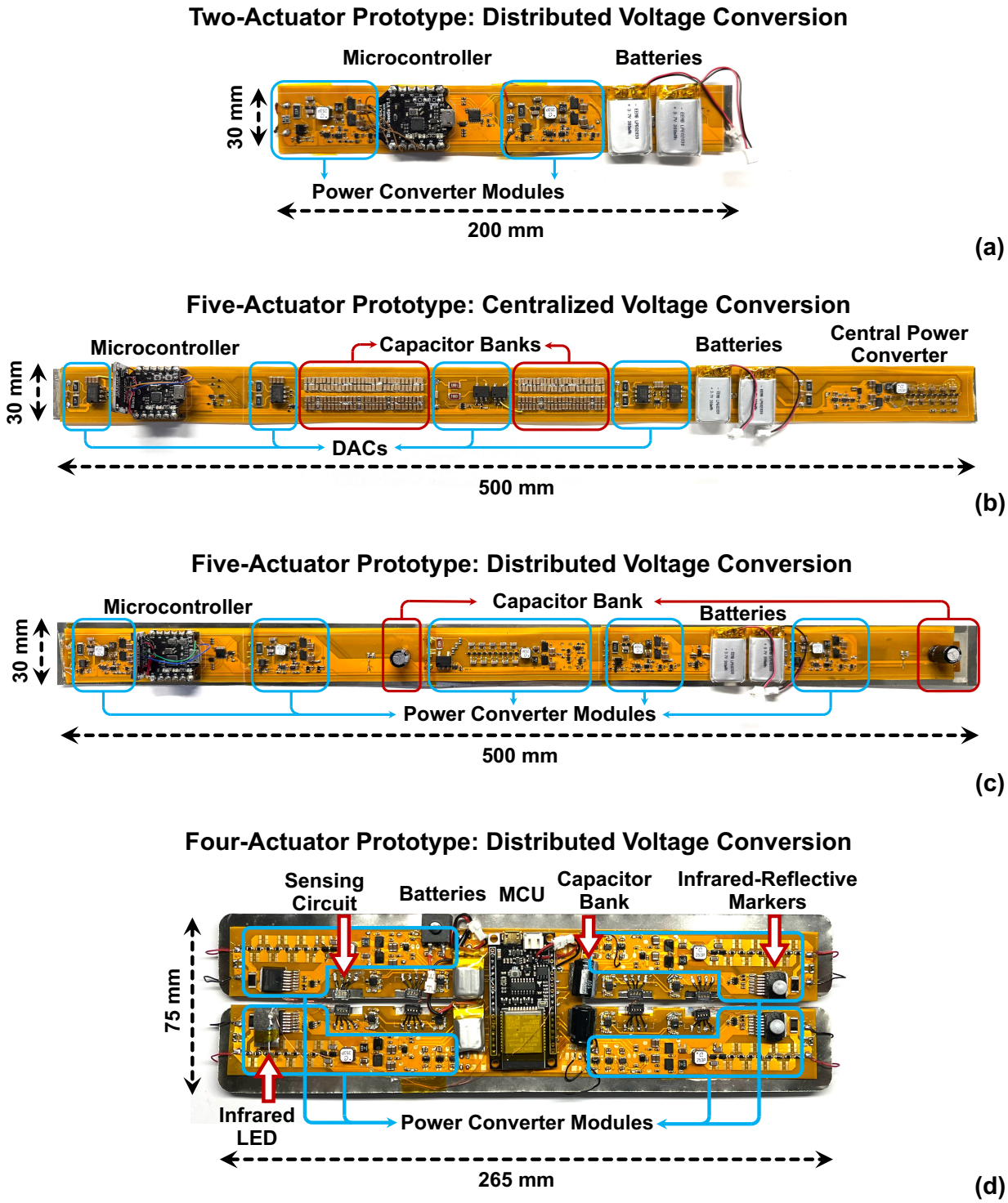

Figure 3.12: Four PCB designs across three versions of eViper robot prototypes. The figures are not to scale. The actual dimensions are labeled.

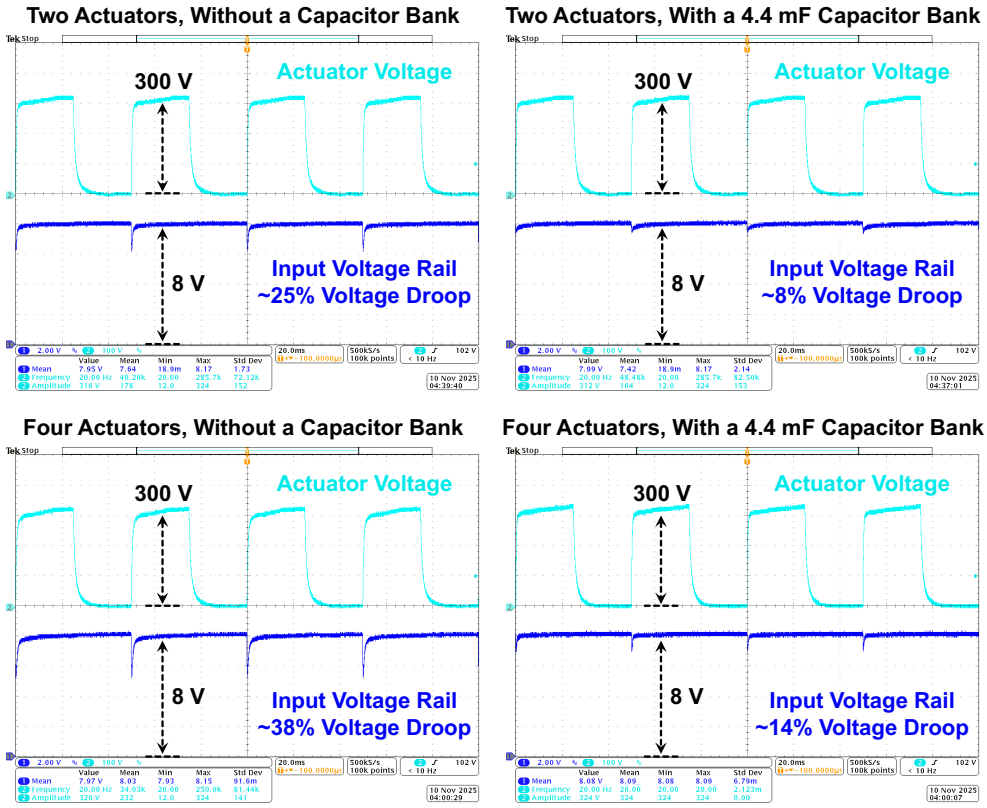

Figure 3.13: Oscilloscope images showing the voltage applied to an actuator (light blue waveform) and the input rail with voltage droop (dark blue waveform). The top row compares the results of driving two actuators simultaneously, with and without a capacitor bank, while the bottom row shows the cases of concurrently activating four actuators. Capacitor banks are effective in reducing the magnitude of voltage droop. The power source of this test was two fully-charged lithium polymer batteries, so the input voltage level is slightly higher than the nominal 7.4 V.

batteries. Li-Po batteries are utilized in this research because their rated dc output current (200 mA or higher) significantly exceeds that of coin batteries (∼1 mA). Additionally, Li-Po batteries are rechargeable, but most coin batteries are not. Rechargeable batteries are preferred because they enable repeated operation without replacement, simplifying system maintenance and reducing environmental impact. The nominal output voltage of a Li-Po battery is 3.7 V, the 7.4 V system input voltage is acquired by series connection of two Li-Po batteries.

Due to the capacitive nature of piezoelectric actuators, the converters must supply pulsating currents when charging the loads with square waves. However, the batteries cannot deliver large currents instantaneously, leading to voltage droop on the input voltage rail. This effect is more pronounced when multiple actuators are driven simultaneously since it puts more stress on the input

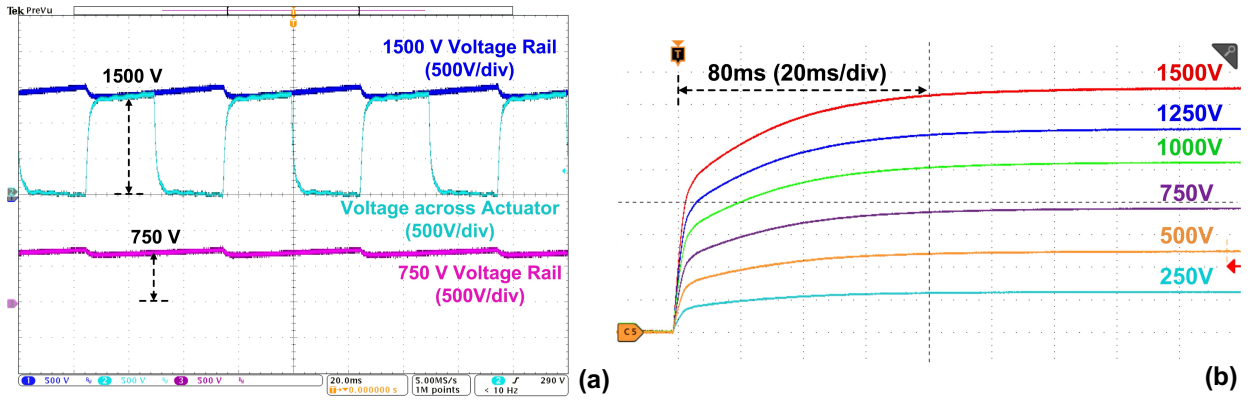

Figure 3.14: Oscilloscope images demonstrating the waveforms of the high-voltage rails and the voltage applied to an actuator in a centralized voltage conversion architecture. (a) Transient voltage droop when driving a 1500 V actuator. (b) Start-up transient of the voltage multiplier. The voltage rails are evenly distributed. In this experiment, the basic voltage level was regulated to 250 V, and there are six multiplier stages to generate 1500 V.

voltage rail. A capacitor bank is needed to stabilize the rail. Fig. 3.13 shows the waveforms of the input voltage rail and the 300 V output square waves at 20 Hz. The top row presents the results of driving two actuators together, with and without a capacitor bank, while the bottom row shows the case of driving four actuators concurrently on the four-actuator prototype (Fig. 3.12(d)). In both scenarios, a capacitor bank significantly reduces the droop magnitude. The two-actuator prototype was built without an input capacitor bank; however, such a feature can be seamlessly implemented if required. Prototypes with a larger number of actuators integrate capacitor banks to handle worst-case conditions, where multiple actuators are driven simultaneously. A larger capacitor bank can be utilized to further reduce the voltage droop magnitude, at the cost of increased area and weight. The current configuration (4.4 mF in total) represents a balanced trade-off between rail stability and system weight.

In the five-actuator prototype, both centralized and distributed voltage conversion architecture were constructed. In this prototype, 300 V and 1500 V actuators need to be driven simultaneously, therefore, two high-voltage rails need to be maintained in the PCB of Fig. 3.12(b). Aluminum electrolytic capacitors can be used to construct the 300 V rail, but the 1500 V rail becomes problematic since the voltage rating of those capacitors are less than 800 V. Cascading electrolytic capacitors to withstand higher voltage results in lower power efficiency, higher size and weight, and potential voltage balancing problems. Therefore, both high-voltage rails in this design were implemented

with multi-layer ceramic capacitors (MLCCs) for consistency and reliability. MLCCs generally have lower capacitance and suffer from dc voltage derating, therefore, many of them need to be connected in parallel and occupy a noticeable area on the PCB. Fig. 3.14 demonstrates waveforms measured from a five-actuator prototype with centralized voltage conversion architecture.

In the distributed version of the five-actuator PCB (Fig. 3.12(c)), five converter modules are required to drive the actuators, and two aluminum electrolytic capacitors (4.4 mF in total) were used to buffer the input voltage rail. A low-voltage capacitor bank occupies less PCB area and reduces the pulsating current stress on the power source.

The PCB for the four-actuator prototype was designed to have the highest flexibility and modularity. There are four power modules on the PCB. Each power module can drive an arbitrary actuator with required voltage up to 1500 V. A distributed power architecture was chosen for maximum controllability, modularity, and compactness of capacitor banks. The infrared-related components are related to robot motion analysis and will be discussed in later chapters.

All MCUs in Fig. 3.12 are capable of Bluetooth communication. Therefore, the power modules and the robots can be controlled remotely.

3.6.2 High-Voltage Safety Features

The PCBs developed in this thesis generate high output voltages. Consequently, several safety features are implemented to enhance operational safety. A red light-emitting diode (LED) is connected to the low-dropout (LDO) voltage regulator that powers the essential integrated circuits in each high voltage power converter. As a result, the LED is illuminated whenever the converter is operating, providing a clear visual signal that high voltage is present on the PCB. Additionally, each actuator is connected to a 2 MΩ bleeder resistor, which is placed in parallel with the actuator terminals. These resistors consume low power during normal operation and ensure each actuator is safely discharged after system shutdown. The high-voltage capacitor banks in the centralized architecture are also equipped with bleeder resistors. Together, these measures provide clear visual signals during system operation and ensure that the stored high voltage is dissipated after experiments. Fig. 3.15 illustrates the two safety features by using the four-actuator prototype as an example.

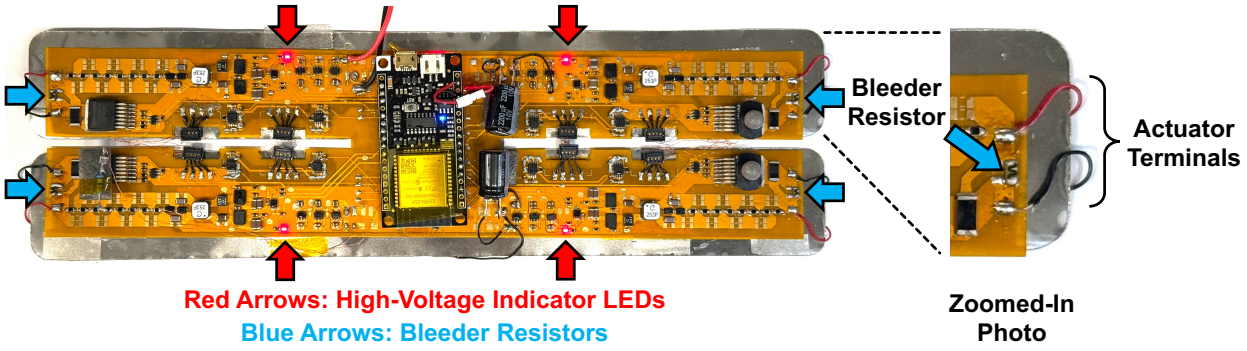

Figure 3.15: Safety features implemented on the PCBs. The red arrows highlight the high-voltage indicator LEDs, while the blue arrows mark the bleeder resistors. A zoomed-in photo is provided to show that the bleeder resistors are connected in parallel with the actuator terminals.

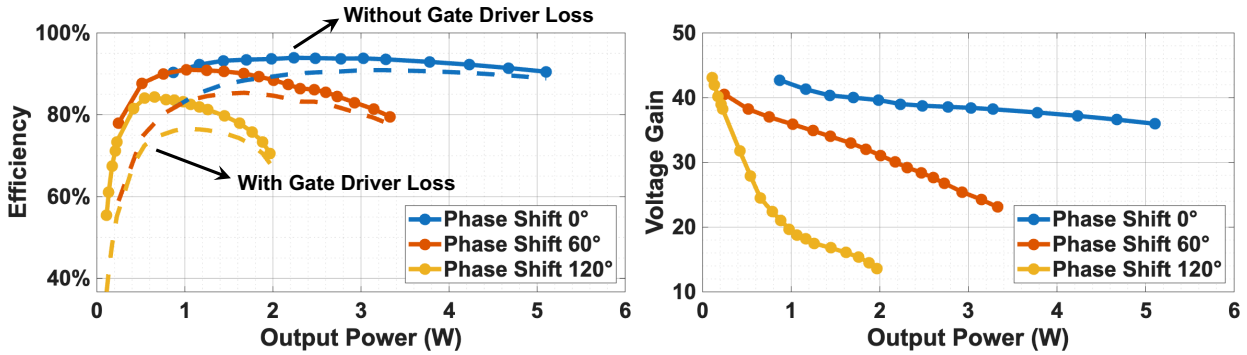

Figure 3.16: Dc-dc power conversion efficiency and voltage gain of the converter with respect to the output power. The legend indicates the phase shift applied to the two half-bridge branches of the full-bridge inverter, and 0° phase shift corresponds to the traditional full-bridge operation where the two half-bridge branches are out of phase. In the left figure, the solid lines represent the data without considering gate driver loss, and the dashed lines show the estimated efficiencies including gate driver loss.

3.6.3 Dc-dc Power Efficiency

The voltage gain of the circuit can be modulated by frequency and phase-shift modulation. Fig. 3.16 shows the dc-dc power conversion efficiency and voltage gain measured at different phase shifts. After considering gate driver loss, the converter's peak efficiency is 90.9% at 0° phase shift and 76.5% at 120° phase shift. The phase-shift modulation presents another degree of freedom for modulating the voltage gain of a full-bridge LLC converter other than frequency modulation, making a full-bridge design more attractive than half-bridge options. This figure reports the dc-dc power efficiency. However, the power circuit almost always needs to drive actuators with an ac waveform in this thesis. In Section 3.9, the system's ac power efficiency is analyzed.

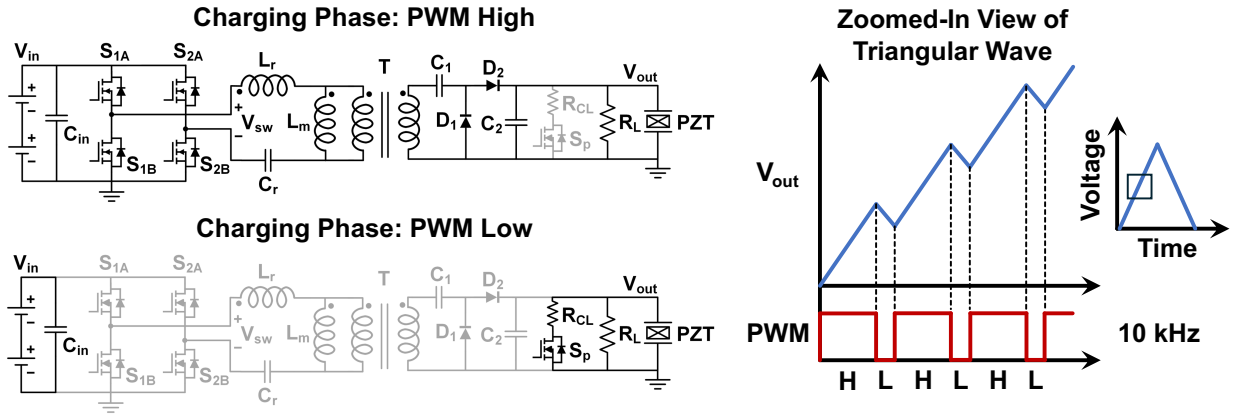

Figure 3.17: Schematics showing the two operational states of the circuit when generating the charging phase of triangular waves. The grayed-out circuit is deactivated. The right half of the figure shows an illustration of a zoomed-in triangular wave synchronized with the PWM control signal. Due to the incremental charging and discharging behavior, V_{out} is a sawtooth-like waveform.

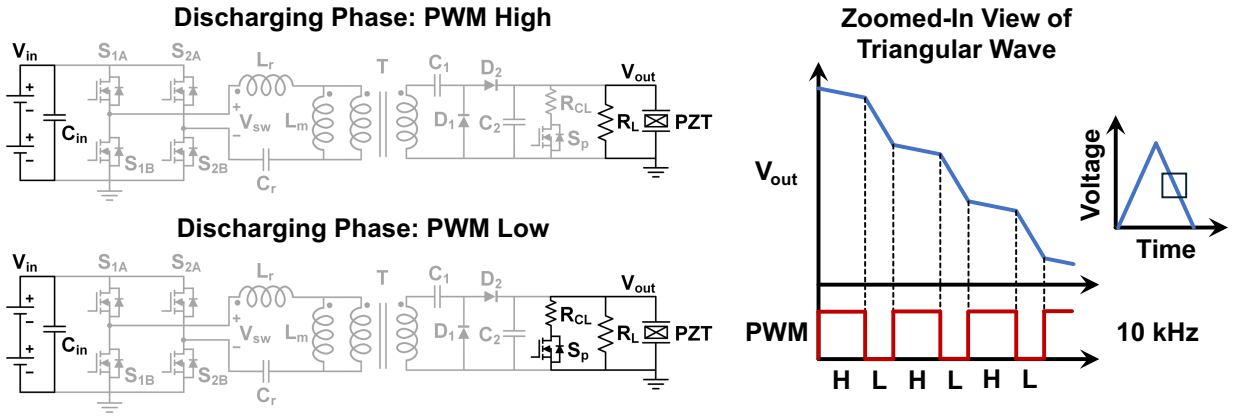

Figure 3.18: Schematics showing the two operational states of the circuit when generating the discharging phase of triangular waves. The grayed-out circuit is deactivated. The right half of the figure shows that V_{out} is discharged at two different rates in an alternating manner.

3.7 High-Voltage Waveform Synthesis for Piezoelectric Actuation

Generating high-voltage triangular or sinusoidal waveforms at the converter output requires the slope of the output voltage be precisely controlled. To achieve this, the power module is controlled by a 10 kHz pulse-width modulation (PWM) signal, which incrementally charge and discharge the actuator and shape the desired waveform. The actuator, which can be primarily modeled as a capacitive load, is always connected to a large bleeder resistor. This resistor provides a continuous discharge path that helps modulate the voltage ramp-up and ramp-down speed of the actuator.

Fig. 3.17 depicts the waveform generation of the triangular-wave charging phase. During the

charging phase, when the PWM signal is high, the converter is enabled and incrementally charges the actuator. When the PWM signal is low, the converter is disabled, allowing the actuator to discharge slightly through the discharge circuit. The discharge in this period is intentionally smaller than the charge gained during the PWM-high state to ensure a net increase in voltage. By adjusting the duty ratio of the 10 kHz PWM signal, the effective charging rate and the slope of the voltage waveform can be precisely tuned. A higher duty ratio results in a steeper voltage slope.

Fig. 3.18 depicts the waveform generation of the triangular-wave discharging phase. During the discharging phase, the full-bridge switches of the converter remains off, and the 10 kHz PWM signal is still on. The actuator slowly discharges through the large bleeder resistor when the PWM signal is high, and it discharges through the low-resistance discharge circuit when the signal is low. This configuration allows control of the overall discharge rate by alternating between slow and fast discharge paths according to the PWM duty ratio.

Because the piezoelectric actuator behaves as a capacitive load, the voltage waveform of the converter output naturally follows an RC charging and discharging curve. To obtain a desired voltage slope, the duty ratio of the 10 kHz PWM signal must therefore be continuously modulated to compensate for the nonlinear slope variations inherent to the RC response. In the current implementation, each cycle of the triangular waveform is divided into 20 discrete steps, meaning that the PWM duty ratio is updated 20 times per cycle to achieve the desired waveform accuracy. More discrete steps can be utilized to further improve the waveform shape accuracy and controllability, though this should be balanced with the available computational resources of the MCU. The procedure for generating high-voltage sinusoidal waveforms is similar. However, the PWM duty ratios must be appropriately modified to accommodate the different waveform shape.

Fig. 3.19 shows the experimental results for the 300 V waveform generation. By carefully controlling the duty ratio of the 10 kHz PWM signal, high-voltage high-fidelity triangular and sine waves can be generated from the distributed power architecture.

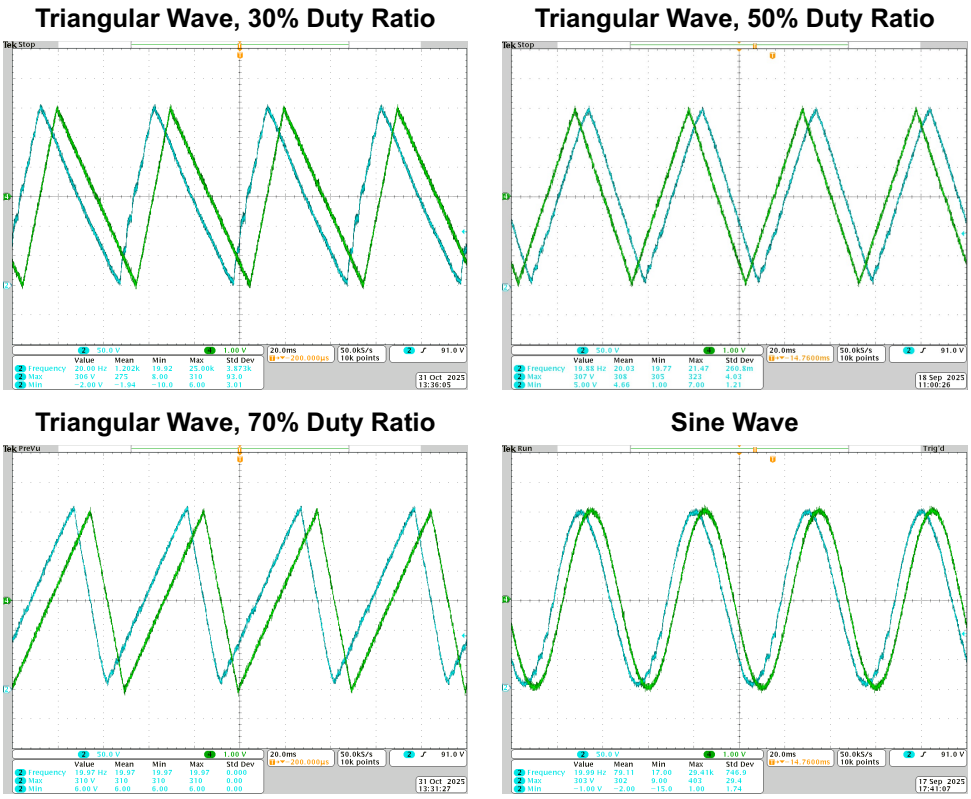

Figure 3.19: Oscilloscope images showing the converter-generated triangular waves and sine wave. The light blue waveform represents the 300 V waveforms generated by the converter. The light green waveform is a low-voltage reference signal generated by an external signal generator to visually compare the converter output with an ideal waveform shape.

3.8 System Power Consumption When Driving a Single Actuator

When piezoelectric actuators are integrated into a soft robotic system, the power demand is affected by not only the actuator but also the behavior of the driving power converter. Circuit topology, switching dynamics, waveform synthesis, and control strategy all influence how much energy needs to be supplied by the input source. To obtain a realistic estimation of energy usage, particularly for untethered robots powered by compact batteries, it is important to measure the input power drawn by the converter while it drives the output actuator with representative waveforms. The system-level observation reveals how different loading conditions, driving frequencies, and operating waveforms impacts the energy demand, and it also provides practical insights for optimizing the operational waveforms, control methods, and battery sizing.

The input power of a power module is measured under three different conditions: (1) Driving an

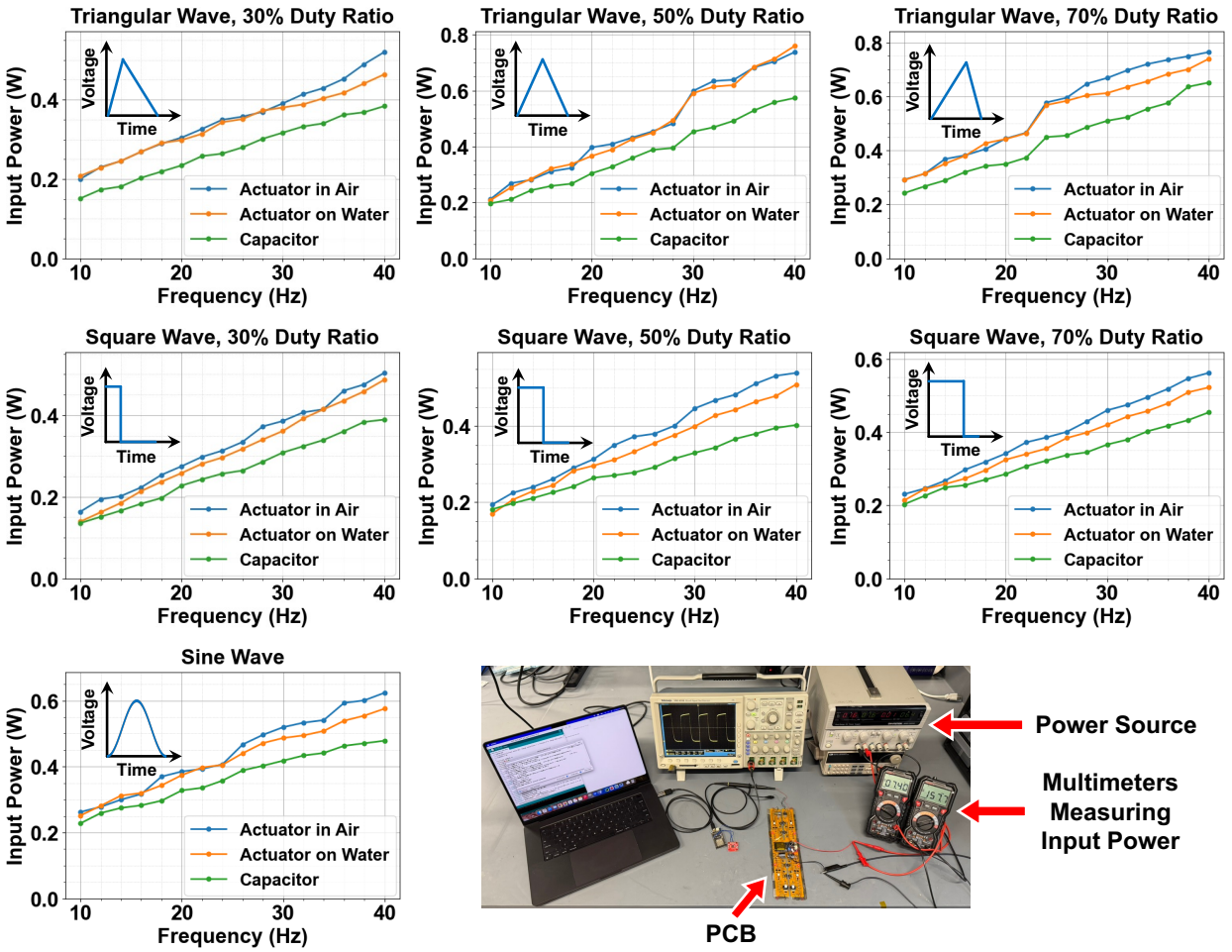

Figure 3.20: Measured converter input power for different driving waveforms across three converter loading conditions. The photo of experimental setup is attached.

actuator in the four-actuator prototype in air, (2) Driving an actuator in the amphibious prototype when it is floating on the surface of water, and (3) Driving an MLCC with comparable capacitance as the piezoelectric actuator (no mechanical motion in this case). Measured by an impedance analyzer (HP 4192A), the effective capacitance of a P2 MFC is approximately 120 nF. The MLCC used in this experiment (TDK CGA6M1X7T2J154K200AC) has a nominal capacitance of 150 nF. After considering DC voltage derating, it has a capacitance of approximately 100 nF. Comparing operating conditions (1) or (2) with (3) reveals how much more energy is required to drive a piezoelectric actuator and generate mechanical displacements than a purely capacitive load. Seven different waveform shapes are used to excite the loads: triangular waves with 30%, 50%, and 70% duty ratio, sine waves, and square waves with 30%, 50%, and 70% duty ratio. A frequency sweep

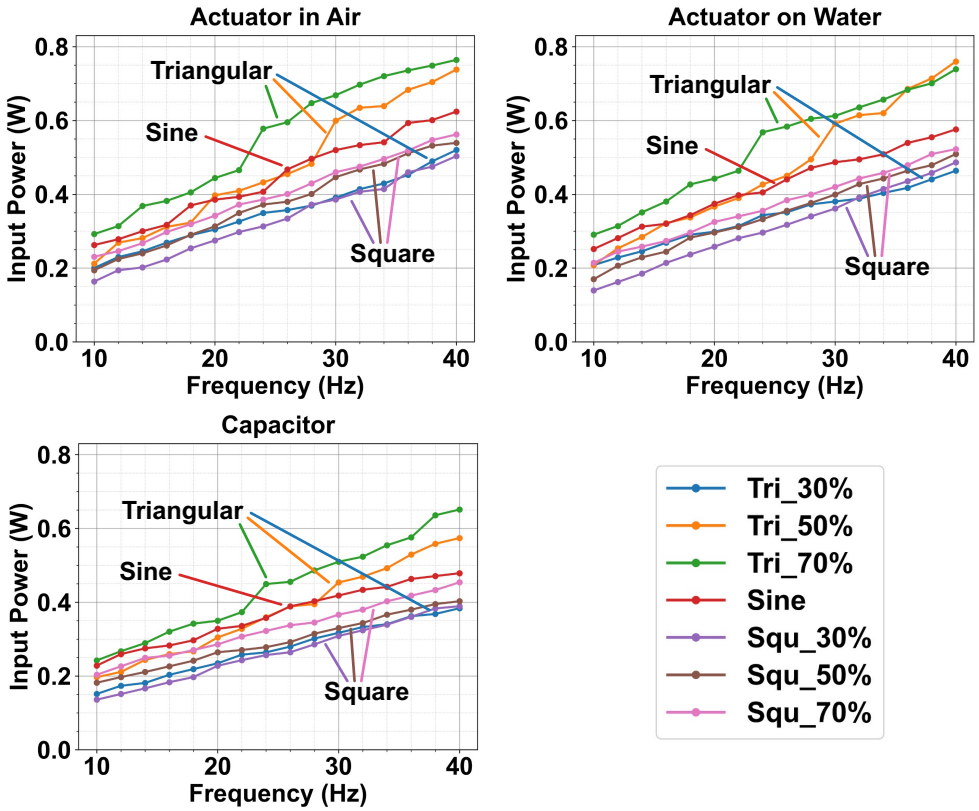

Figure 3.21: Measured converter input power for different loading conditions across seven driving waveforms. The legend is shared across all three sub-figures.

is conducted for each waveform from 10 Hz to 40 Hz, with a step size of 2 Hz.

Fig. 3.20 presents the experimental results for each waveform shape across different converter loading conditions. The power consumption increases with operating frequency because the converter need to charge and discharge a capacitive load more frequently, leading to higher energy use. Another observation is that the difference in power consumption between loading conditions is relatively small at lower frequencies but becomes more pronounced at higher frequencies. On average, driving an actuator at 40 Hz in air consumes ∼5% more power than driving an actuator on the surface of water and ∼22% more power than driving an MLCC.

Fig. 3.21 plots the data for each loading condition across different waveform shapes. For triangular waves, a larger duty ratio leads to higher power consumption since the power module is active during the rising interval. The same trend is also observed for square waves with different duty ratios. It can also be observed that triangular excitation consumes the most power, followed

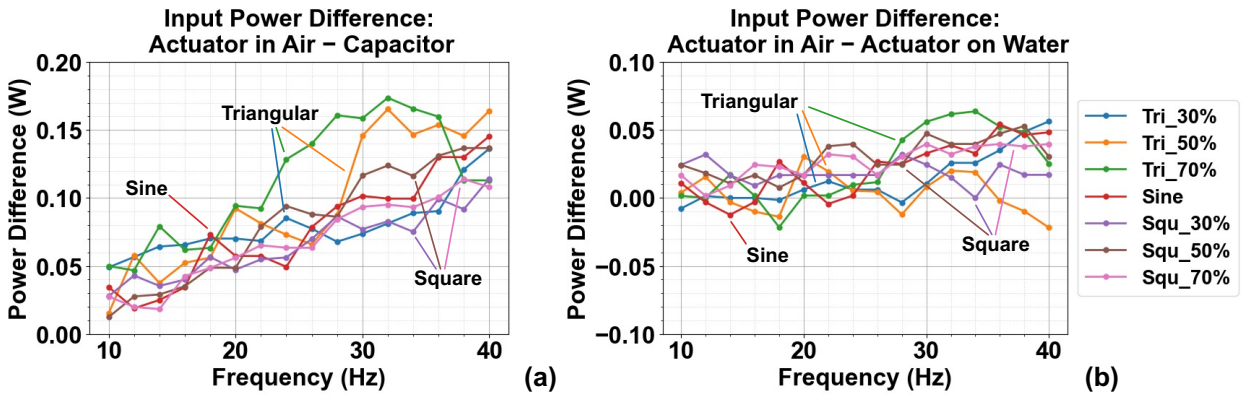

Figure 3.22: Difference of converter input power between (a) driving an actuator in air and a capacitor and (b) driving an actuator in air and an actuator on water surface. The legend is shared across the sub-figures.

by sinusoidal excitation, while square-wave excitation consumes the least.

Knowing that driving actuators in air requires the most power, Fig. 3.22 further shows the difference of measured system input power among different loading conditions. Fig. 3.22(a) shows the difference between driving actuators in air and driving capacitors. The difference increases with frequency, and the curves roughly lie in the same range. Fig. 3.22(b) shows the difference of driving actuators in different environments. The power difference has a weak positive relationship with increasing frequency. Most data points are positive, indicating that operating actuators in air typically require more power than on water.

3.9 System-Level Power Analysis

Fig. 3.23 illustrates the key power-flow components of the entire system. P_{in} denotes the electrical input power delivered from the batteries to the power system and is measured in Section 3.8. P_{out} represents the power delivered by the converter to the actuator and is computed as $E_{stored,\,max}$ divided by the period of an operation cycle (refer to Section 2.4). $P_{heat,\,pw}$ denotes the power conversion loss in the power electronics. The net power absorbed by the actuator is divided into mechanical output power, P_{mech}, and actuator material loss, $P_{heat,\,act}$. The sum of these two terms can be calculated by dividing $E_{net,\,act}$ by the period of an operation cycle. Finally, $P_{discharge}$ represents the power returned from the actuator to the power electronics and is dissipated in the discharging resistor R_{CL}. The current power architecture does not have energy recycling capability.

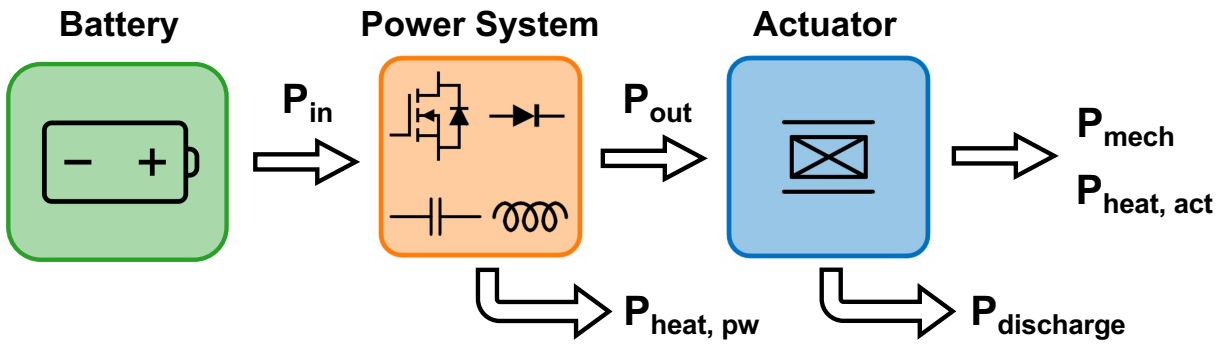

Figure 3.23: A block diagram showing system-level power flow from the battery to the actuator.

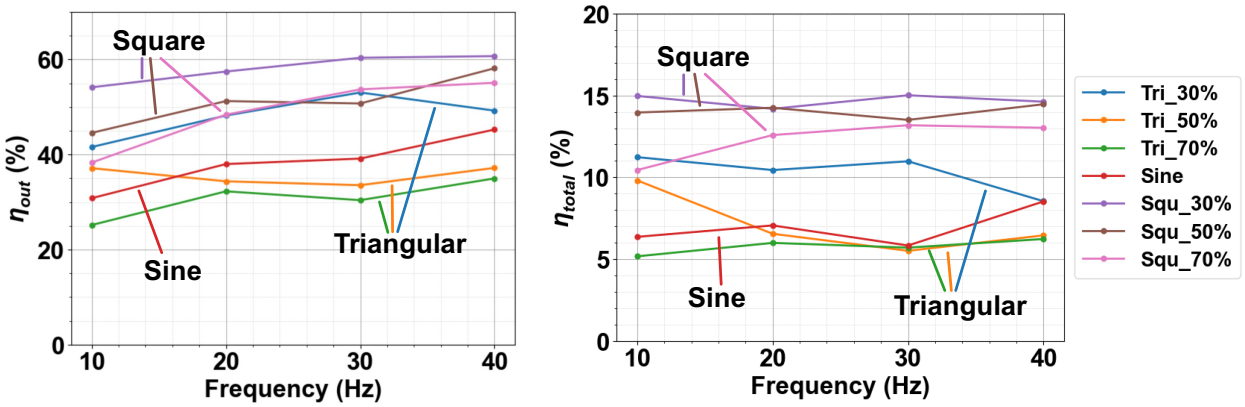

Figure 3.24: Data of η_{out} and η_{total} across operating waveforms and frequencies.

Therefore, $P_{discharge}$ cannot be recovered.

Based on the above power components, two system-level power metrics can be defined:

$$\eta_{out} = \frac{P_{out}}{P_{in}} \tag{3.1}$$

$$\eta_{total} = \frac{(P_{mech} + P_{heat,act})}{P_{in}} \tag{3.2}$$

η_{out} denotes the fraction of the input power that is delivered to the actuator and can be interpreted as the converter's ac power efficiency. η_{total} represents the fraction of the input power absorbed by the actuator and can be interpreted as the overall system power efficiency. These two metrics are calculated and displayed in Fig. 3.24.

η_{out} is typically lower for triangular and sinusoidal excitation and higher for square-wave excitation, which can be attributed to the waveform synthesis process introduced in Section 3.7.

During the charging phase of waveform synthesis, the actuator voltage is incrementally charged and discharged, leading to additional power loss. Alternative control strategies or circuit topologies may improve the ac power efficiency. The measured η_{total} lies between 5% to 15%. Square-wave excitation have higher power utilization than triangular and sinusoidal excitation. During the power measurements, the actuator is fixed in place and driven in air. Therefore, the mechanical output power P_{mech} is expected to be small (primarily moving the air), and $P_{heat,act}$ should contribute to the majority of the reported η_{total}. Several approaches may be explored to improve η_{total}, including (1) measure the V-Q loop of an actuator when it is doing mechanical work on external objects, and (2) investigate circuit topologies that enable energy recycling. η_{total} could be improved significantly if $P_{discharge}$ can be partially recovered.

3.10 Chapter Summary

This chapter investigates the power circuitry and energy flow of the eViper soft robotic platform. Power converter topologies, PCB implementation, and power delivery architectures are analyzed, and the design constraints are specified. Control methods for waveform synthesis are introduced and experimentally demonstrated. Finally, system-level power flow and energy utilization are studied, providing valuable insights for energy-aware control strategies across different driving waveforms and operating frequencies.

4

Linear 1D Piezoelectric Robots

This chapter is based on work published in the following papers:

- *H. Cheng, Z. Zheng, P. Kumar, W. Afridi, B. Kim, S. Wagner, N. Verma, J. C. Sturm and M. Chen, "eViper: A Scalable Platform for Untethered Modular Soft Robots," 2023 IEEE/RSJ International Conference on Intelligent Robots and Systems (IROS)*

- *Z. Zheng, H. Cheng, P. Kumar, S. Wagner, M. Chen, N. Verma and J. C. Sturm, "Wirelessly-Controlled Untethered Piezoelectric Planar Soft Robot Capable of Bidirectional Crawling and Rotation," 2023 IEEE International Conference on Robotics and Automation (ICRA)*

4.1 Chapter Introduction

This chapter introduces the linear, two-actuator eViper system. Inspired by inchworm locomotion, the two actuators are aligned end-to-end, giving the robot a one-dimensional (1D) overall structure. The prototype integrates actuators, power electronics, batteries, control, and a wireless MCU, enabling fully untethered operation. Sensors are also installed onboard, allowing the robot to measure its linear and rotational velocities.

Section 4.2 presents the hardware composition of the two-actuator eViper. Section 4.3 qualitatively explains its motion mechanism. Section 4.4 describes the employed approaches to simulate the robot's behavior in the PyBullet physics engine. Section 4.5 analyzes the impact of electrical driving parameters and battery weight distribution on the robot's locomotion behavior and energy efficiency. Finally, Section 4.6 summarizes this chapter.

4.2 Two-Actuator eViper Hardware Implementation

Figure 4.1 illustrates the mechanical structure of a two-actuator eViper example. The fabrication process is hierarchical, based on separating the components required for different functionality (actuators, mechanical substrate, power electronics, and control circuitry) across different soft and flexible layers. eViper is a piezoelectric soft robot. Each piezoelectric actuator is a 20-mm-wide, 100-mm-long, and 300-μm-thick commercial Macro Fiber Composite (MFC) unit from Smart Material Corp. [33], bonded to a 50-μm-thick steel foil. On top of the steel foil, we customized a

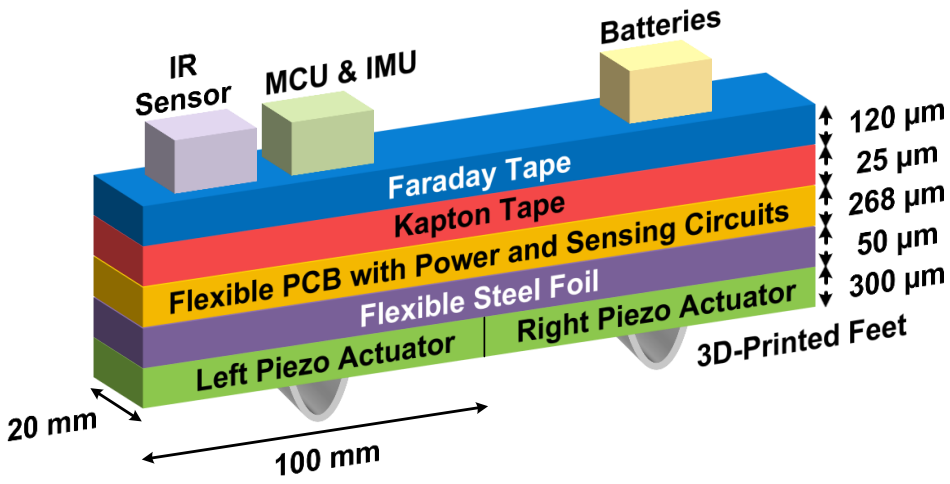

Figure 4.1: Mechanical structure of an illustrative two-actuator eViper comprising actuators, power electronics, sensors, microcontroller, and batteries. The actuators and the steel foil are bonded with epoxy glue. Other layers are bonded with double-sided tape or Kapton tape.

flexible printed circuit board (PCB) that hosts power converters and control circuitry to drive the actuators. To ensure safe testing and high voltage insulation, the power electronics are enclosed in a shielding layer. The shielding layer comprises a 25-μm-thick Kapton tape covered by a 120-μm-thick Faraday tape. The Faraday tape is conductive and is connected to the negative terminal of the battery (the electrical ground of the robot), functioning as a Faraday cage and electromagnetic interference (EMI) shield to block the high voltage. The batteries, microcontroller, communication circuits, and auxiliary sensors (all low-voltage) are left outside. Two 3D-printed plastic "D"-shaped feet are attached to the bottom side of the robot to lift the robot body and ensure robust ground friction. All these functional layers contribute to the weight distribution and the stiffness of the soft robot. These factors, together with the actuation pattern, jointly affect the locomotion efficiency and the payload capacity.

Figure 4.2(a) and 4.2(b) show the top view and the side view of the assembled robot. The infrared (IR) distance sensor, microcontroller (MCU), inertial measurement unit (IMU), and batteries are visible from the outside. The high-voltage power electronics are shielded by the Kapton and Faraday tapes. Figure 4.2(c) shows the power electronics inside the shielding. The weight of the robot is 44.5 g. Its remaining payload of about 10 g can accommodate more electronics or batteries. The structure of the proposed platform is highly scalable. It can be extended to a larger actuator

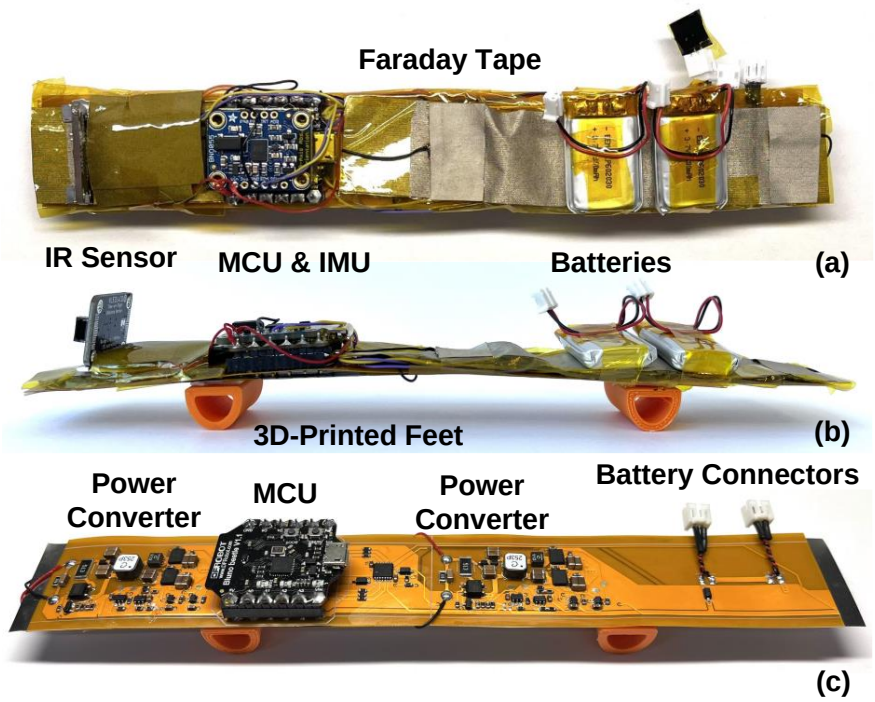

Figure 4.2: (a) Top view, (b) Side view, and (c) Embedded power electronics of a two-actuator eViper. The high voltage circuits are shielded by a Kapton insulating tape to ensure electrical safety, and a conductive Faraday tape connected to the negative terminal of the battery to block electromagnetic interference (EMI). The length and width of the robot are 200 mm $\times$ 20 mm. The height of the two 3D-printed robot feet is 10 mm.

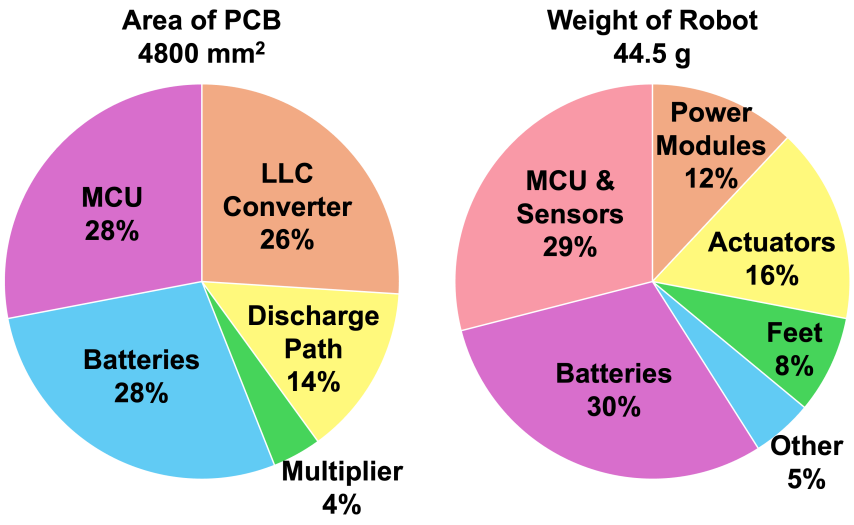

Figure 4.3: The area and weight distribution across multiple functional blocks of the two-actuator eViper. Batteries contribute the most to both the area and weight, indicating that energy storage is the primary constraint of untethered piezoelectric mechatronic systems. An MCU break-out board is utilized for this prototype. In later chapters, we integrate the MCU chip directly on the PCB to save area and weight contribution of the MCU.

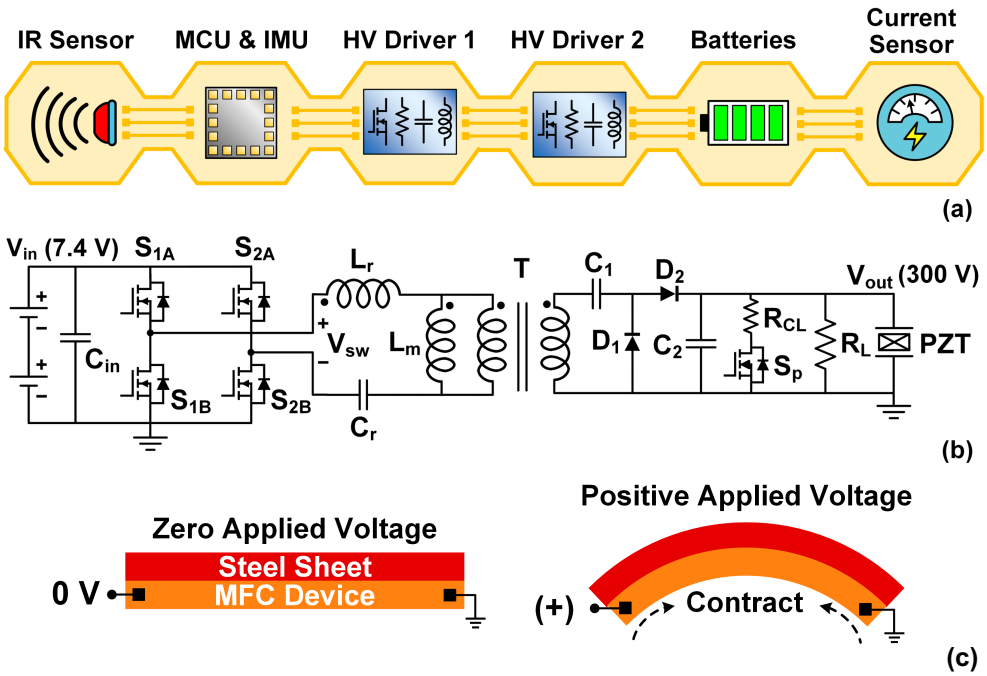

Figure 4.4: (a) Block diagram of eViper's electrical platform. (b) The circuit schematic of a high voltage driver with five configurable output voltage options. There are two high voltage drivers on board, and only the 300 V output is used in this work. (c) Bending behavior of the steel-bonded piezoelectric actuator. The red layer is the steel sheet, and the orange layer is the MFC device. The actuator bends concave down when a positive voltage is applied.

array or be arranged to other shapes based on need and application, which will be introduced in later parts of this thesis. Fig. 4.3 presents the pie charts for the area and weight distribution across functional blocks of this two-actuator prototype.

Figure 4.4 provides an overview of the electrical architecture of the soft robot. The circuit schematic and actuator bending behavior are attached for completeness. The eViper is controlled by a microcontroller which can support many sensors. A Bluetooth microcontroller (DFRobot DFR0339) takes charge of actuator control, sensor control, and communication with the PC; an infrared (IR) distance sensor (Adafruit VL53L4CD) measures robot velocity and detects the robot location; a nine-axis inertial measurement unit (IMU, Adafruit BNO055) is used for measuring locomotion; and a DC current sensor (Atnsinc INA219) gauges the power consumption of the untethered robot. The microcontroller and the sensors together consume about 0.8 W. The power stage consumes about 0.4 W. The power consumption of the entire robot is about 1.2 W. The batteries last for approximately an hour.

4.3 Two-Actuator eViper Basic Operation Mechanism

We start analyzing the locomotion of the two-actuator eViper by only driving a single actuator at a time. Motion in the long direction of the robot is created due to actuation asymmetry, weight, and structure. Figure 4.5 illustrates five general locomotion steps when only driving the left actuator, and we assume the weight distribution across the robot body is uniform. The same principle can also be applied if we only drive the right actuator of a uniform-weight eViper.

While the precise locomotion arises from more complex deformations and forces, the understanding explained in Figure 4.5 provides an effective starting point for design and trade-off exploration. The effectiveness of locomotion depends on the frequency, strength, and duration of the actuation. Asymmetric weight distribution and asymmetric actuation lead to asymmetric locomotion.

Understanding single-actuator actuation serves as the basis of understanding multi-actuator actuation. The locomotion becomes more complicated when two actuators are operating at various frequencies, duty ratios, and phases, and if weight distribution is asymmetric. Figure 4.6 shows an example of periodic control signals for both actuators. The enormous control DOF makes it complicated and impractical to develop an analytical model for describing the locomotion. Instead, we build a simulation toolkit to assist in the design and control of the modular soft robot.

4.4 SFERS: Simulation Framework for Electroactive Robotic Sheet

We introduce SFERS [53] as an open-source software platform (at https://github.com/zhiwuz/sfers) based on PyBullet, for rapid simulation of a multi-actuator soft robot. As shown in Fig. 4.7, SFERS models piezoelectric actuators as a series of short and rigid links connected with torque-controlled motors. It computes motor torques from the voltages applied to the actuators and uses the information to drive the soft robot. The model has proved useful for modeling static and dynamic motion of multi-actuator piezoelectric 2-D soft robots [53]. In this work, we model each actuator as six links and five motors. The entire two-actuator robot has eleven links and ten motors (the links at the junction of two actuators are treated as one link). Based on the measured material properties of eViper, the motors in the simulation are set to have a torsional Hooke's constant of 0.32 N·m. In

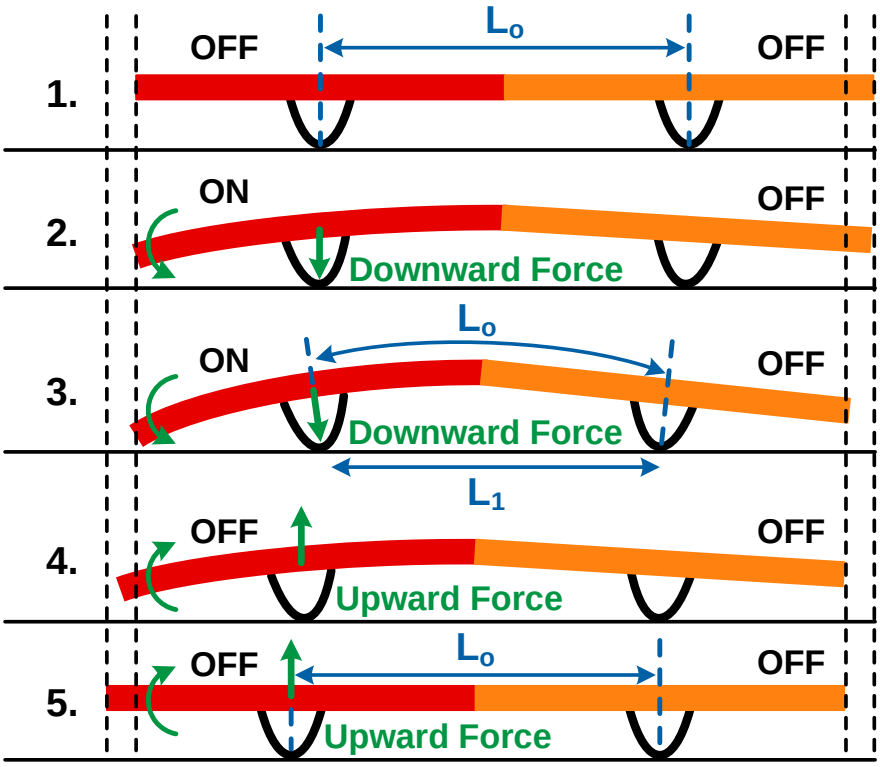

Figure 4.5: An illustration depicting the leftward motion when only driving the left actuator. 1. The initial state: L_o is the distance between the two contact points of the feet on the ground. 2. High voltage (300 V) is applied to the left actuator. It starts to bend concave down and applies a downward force to the left foot. The force increases the normal force and the maximum static friction between the left foot and the ground during the dynamic bending process. 3. The left actuator bends to its maximum extent. The distance between the two contact points, L_1, must be smaller than the original distance L_o due to the robot curvature. Since the left foot has a higher maximum static friction, the right foot is easier to move and is dragged to the left. 4. 0 V is applied to the left actuator, causing it to flatten and apply an upward force to the left foot, decreasing the normal force and the maximum static friction between the left foot and the ground. 5. In the final step of the cycle, the robot finishes flattening. Since the left foot has a lower maximum static friction than the right foot until the end of the cycle (robot completely flat), the left foot is easier to move and slides to the left. Then the entire robot has moved to the left with respect to its initial state.

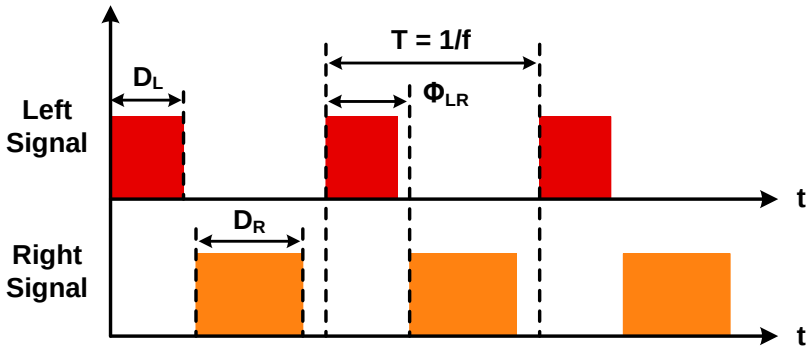

Figure 4.6: Example of periodic control signals when driving both actuators with a specific frequency (f), phase (Φ_{LR}), duty ratio of the left actuator (D_L), and duty ratio of the right actuator (D_R). Frequency is the reciprocal of the signal period T. Phase is the fraction of a period T between the rising edges of the two signals and is often expressed in degrees (0° to 360°). The duty ratio, when expressed as a percentage, is the fraction of a period T that a signal remains at the high level.

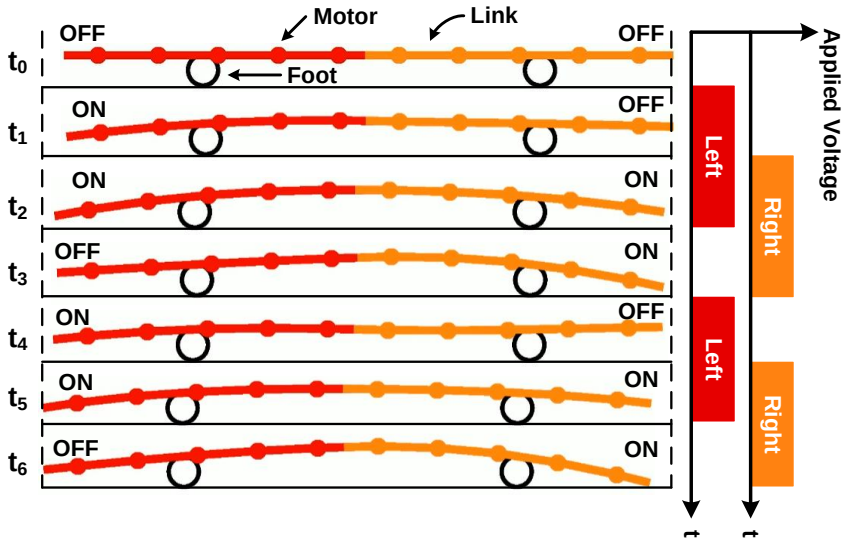

Figure 4.7: Illustration showing the concept of the motor-link structure together with several frames (t_0 to t_6) in a simulation video. We use five motors to simulate one actuator. The time difference between each frame is 20 ms. The right side shows the applied voltage versus time. The red and orange voltages correspond to the left and right actuator, respectively.

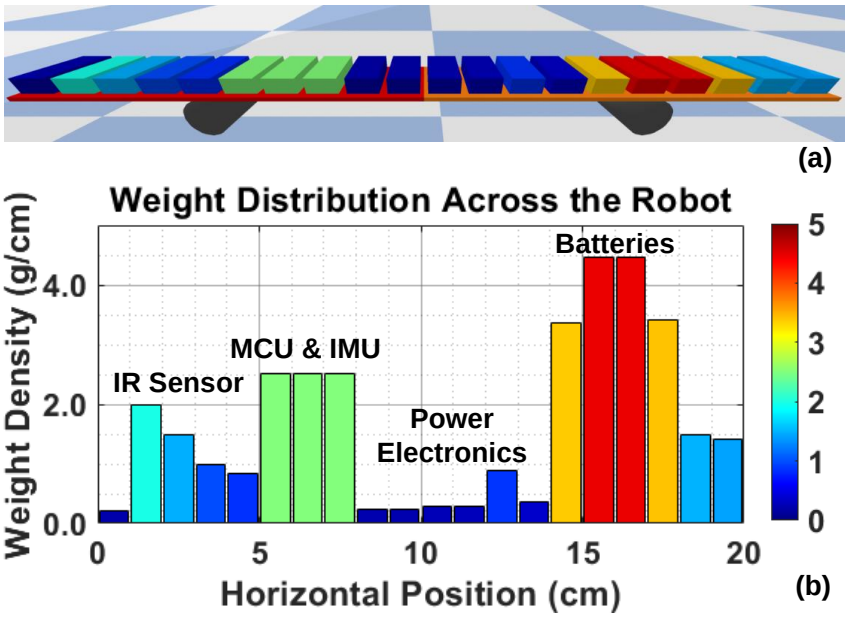

Figure 4.8: (a) The side view of the robot in PyBullet physics engine. There are three layers, from top to bottom: the boxes which represent the weight distribution, the actuators, and the feet of the robot. (b) The estimated weight distribution of the components on top of the robot body. Each bar in this graph is assigned the same color as the corresponding box in Figure 4.8(a).

SFERS we model the robot feet as a pair of hard cylinders which are attached to the robot body.

The numerous electronic components and batteries are modeled as inflexible boxes attached to the links, as illustrated in Fig. 4.8(a). The weight of each box is different, and the weight assignment is based on the weight distributed over each centimeter along the robot, which is shown in Fig. 4.8(b). The interface between the weight boxes and the robot body is firm and non-flexible. The robot weighs 44.5 g, including the two batteries weighing 12.4 g ($\sim$28% of the total weight).

The SFERS platform helps to develop a qualitative understanding of robot locomotion. It is a tool to assist more sophisticated soft robot design before experimental prototyping. However, SFERS has many limitations which may prevent it from making a precise prediction of the soft robot locomotion. These limitations include:

- SFERS assumes all functional layers are tightly bonded to each other, which may not be true.
- The electronics and batteries may change the flexibility and the effective Young's modulus.
- The interface between the feet and the external environment is different from the models.
- Non-idealities in the power electronics, e.g., the voltages generated by the power electronics are not ideal pulse-width-modulated square waves but have finite rising and falling time.
- The mechanical characteristics of the soft robot may not be uniform across the entire robot.
- The asymmetry across the width is not captured.

All these factors may influence the accuracy of the PyBullet model and may introduce discrepancies in robot behavior between simulation and experiment. Sensors and closed-loop control are needed for precise robot manipulation and locomotion. Nevertheless, we found that the scalable SFERS modeling framework can capture the general robot behavior across a wide range of operating frequency, phase, and duty ratios. It provides insights on robot locomotion when driving it with different actuation patterns and weight distribution across the robot body.

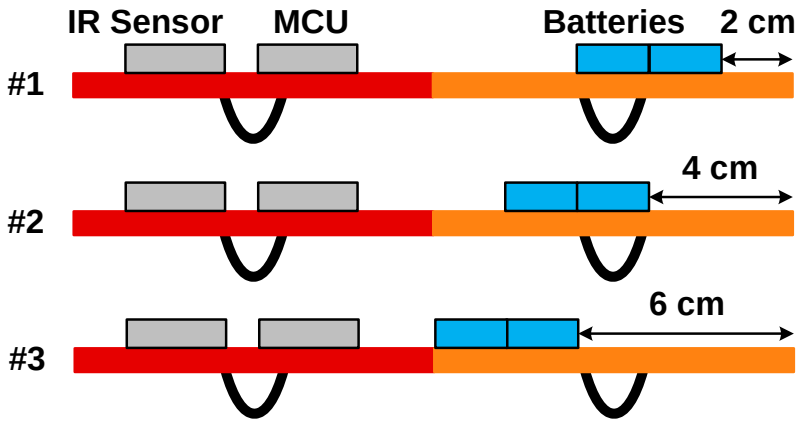

Figure 4.9: The three different battery positions we used to study the impact of weight distribution. We define the figures from top to bottom as battery position #1, #2, and #3, respectively. Battery position #1 is the default position used in the majority of tests presented in this paper.

4.5 Two-Actuator eViper Experimental Results

A test platform was constructed to collect data for experimental verification. The robot is tested on a 37×6-inch marble tile (friction coefficient measured as 0.36). A fence around the experimental area enables IR distance sensing with 1 mm precision. The eViper calculates its velocity and current consumption and communicates with a computer through Bluetooth to transmit the data, enabling fully untethered operation. For each actuation pattern, the robot was activated for 5 seconds to ensure that it reaches a periodic steady state before the data was measured and transmitted back to the computer. The experiments start by actuating a single actuator with different frequencies (8 Hz to 26 Hz) and duty ratios (10% to 90%). The two actuators are then actuated with different frequencies (8 Hz to 26 Hz), phases (0° to 324°), and duty ratios (0% to 90%). As shown in Fig. 4.9, experiments are also conducted with the batteries placed at three different locations to study the weight impact on robot velocities. In the following sections, we define velocity as positive when the robot moves to the left, and negative when it moves to the right.

4.5.1 Velocity and Efficiency when Actuating a Single Actuator

This section presents the simulation and experimental results for driving a single actuator with different frequencies and duty ratios. The velocity and power consumption are measured. The

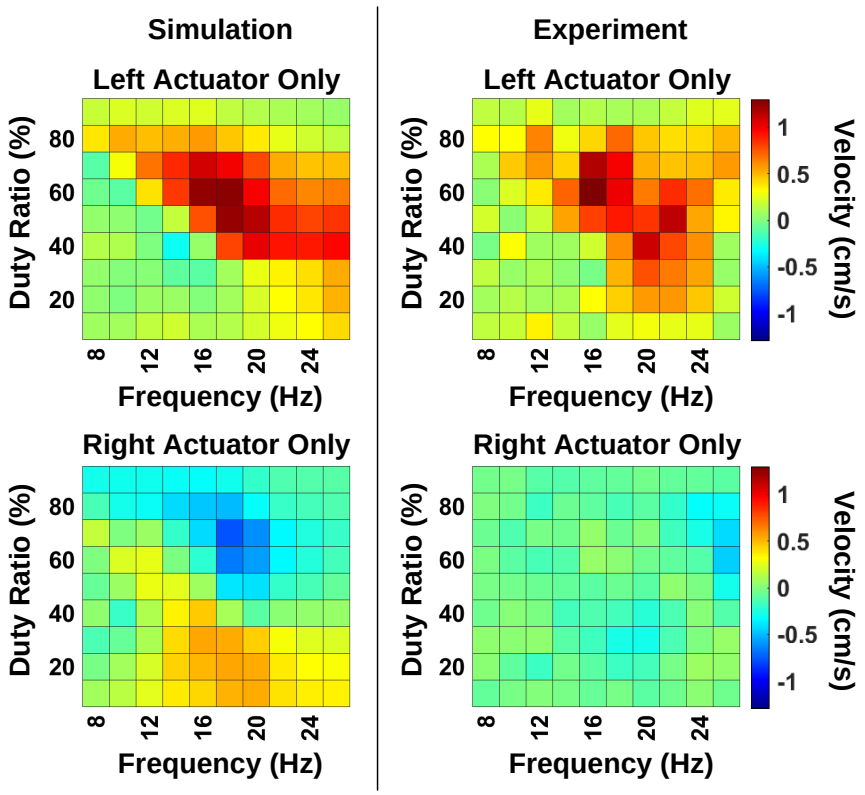

Figure 4.10: Simulated (left column) and experimentally measured (right column) robot velocity as a function of frequency and duty ratio when driving only the left actuator (top row) or the right actuator (bottom row). Batteries at position #1.

batteries are placed at position #1.

Figure 4.10 shows and compares the simulated and measured velocity. In experiments, we measured a maximum positive velocity of 1.3 cm/s at 16 Hz and 60% duty ratio when driving the left actuator only, and a maximum negative velocity of -0.5 cm/s at 26 Hz and 60% duty ratio when driving the right actuator only. The simulation result for the left actuator shows good agreement with the experimental results. However, discrepancies between experiment and simulation are observed for the right actuator. This could be a consequence of the batteries sitting on the right actuator, where they may alter the mechanical properties in a way that is not captured by the simulation.

Figure 4.11 depicts the power consumption for driving a single actuator at various frequency and duty ratio combinations. The values in the figure represent the power consumption of the power stage, which is the power consumed by the driver power electronics and the actuator. It

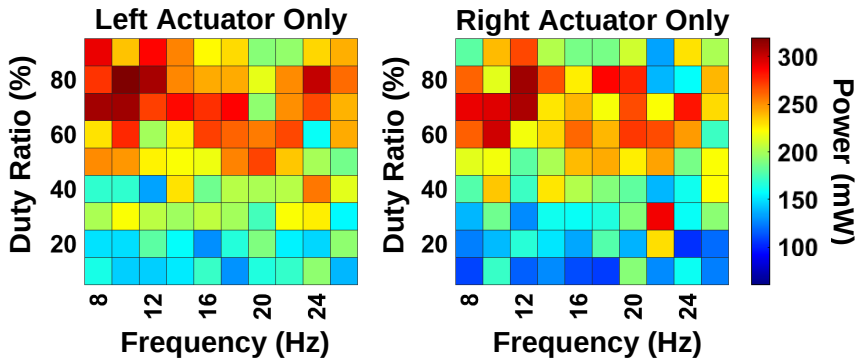

Figure 4.11: The power consumption of the soft robot power stage (power electronics and actuators) as a function of frequency and duty ratio when only driving the left actuator or the right actuator. Batteries at position #1.

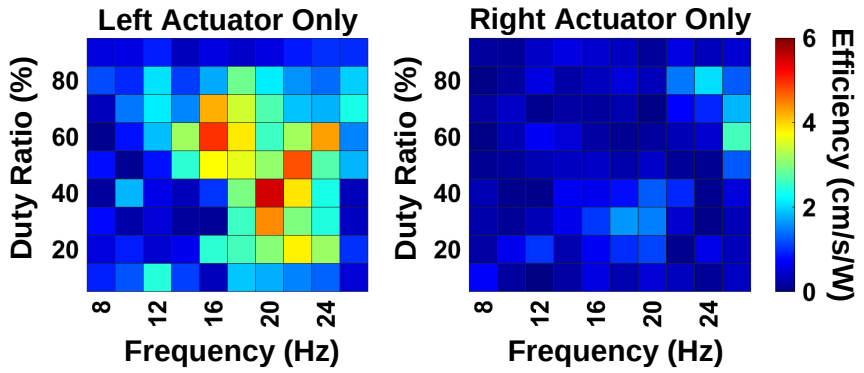

Figure 4.12: The actuation efficiency of the robot as a function of frequency and duty ratio when driving only the left actuator (left figure) or the right actuator (right figure). Driving the left actuator is more efficient than driving the right actuator. Carrying the batteries makes the right actuator less efficient. Batteries at position #1.

can be estimated by multiplying the measured average current by 7.4 V (the battery voltage) and subtracting the computational power (about 740 mW). The power consumption is generally higher with larger duty ratios. This is related to our power electronics design – the power consumption is linearly proportional to the duty ratio of the actuation pattern. A different implementation of the power electronics may lead to very different power consumption.

Dividing the absolute velocity (Fig. 4.10) by power (Fig. 4.11), we can estimate the locomotion efficiency in the unit of cm/s/W, as shown in Fig. 4.12. When driving the left actuator only, the efficiency is generally higher at mid-range frequencies and duty ratios. When driving the right actuator only, the efficiency is much lower due to the battery position.

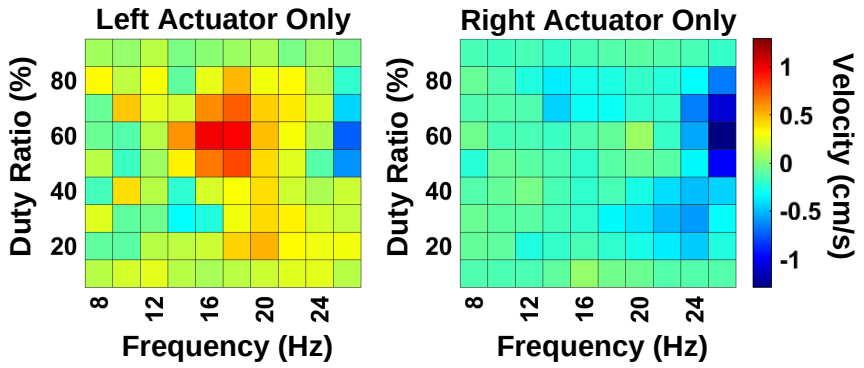

Figure 4.13: Experimentally measured soft robot velocity when driving only the left actuator (left figure) or the right actuator (right figure), with the batteries placed at position #2. The left actuator is again more efficient.

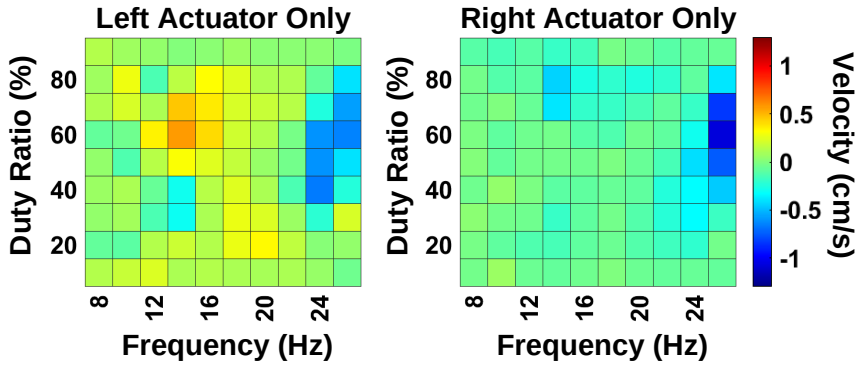

Figure 4.14: Experimentally measured velocity when driving only the left actuator (left figure) or the right actuator (right figure). The batteries are placed at position #3. Both left and right actuators become less efficient.

4.5.2 Impact of Battery Location on Soft Robot Locomotion

In this section, we show the experimental results when moving batteries from position #1 to position #2 and position #3. Only one actuator is actuated at a time.

Figures 4.13–4.14 depicts the velocity measured in experiments. We can observe an obvious difference by comparing these two figures to Fig. 4.10. With the same actuation pattern, the velocities with batteries in positions #2 and #3 are greatly reduced from that in position #1. These results indicate that the weight distribution of components has a significant impact on soft robot locomotion and must be considered when designing the soft robot body and placing the actuators.

The power consumption in positions #2 and #3 is similar to that in position #1 (Fig. 4.11), because the electrical circuits work similarly regardless of the weight distribution, albeit with different

mechanical responses and locomotion. Actuation efficiency can be computed in the same way. Due to a generally lower speed at positions #2 and #3, the efficiencies are also lower than those at position #1 (Fig. 4.12).

4.5.3 Velocity and Efficiency when Driving Two Actuators

In this section, we compare the data obtained in simulation and experiments when driving two actuators together. The batteries are at position #1 for all data presented. To ensure periodic steady-state operation, both actuators are actuated at the same frequency. We sweep the operating frequency together with the phase between the two actuators and the duty ratio of each actuator, and compare the locomotion results of simulations and experiments.

Figure 4.15 shows that in both simulation and experiments, the peak positive and negative velocity usually is reached at mid-range frequencies (14 Hz to 18 Hz), and that more noise is observed at higher and lower frequencies. The data are drawn with respect to the left- and right-actuator duty ratios at a fixed frequency and phase. In the following paragraphs, we call this a frequency-phase combination. As presented in [53], the piezoelectric soft robot is best operated close to the resonant frequency of the actuators. In general, driving the actuators at mid-range frequencies, low phase difference, high left-actuator and low right-actuator duty ratios leads to high velocity toward the left. Driving the actuators at mid-range frequencies, high phase difference, low left-actuator and high right-actuator duty ratios leads to high velocity toward the right. SFERS and experiments agree well on these characteristics. No clear trends are observed at lower or higher frequencies, for example in the third row of Fig. 4.15.

The power consumption of a two-actuator eViper is generally proportional to the summation of their duty ratios. The actuation efficiency can be derived with the same approach. When the robot moves left, the maximum efficiency is 9.5 cm/s/W, obtained at 16 Hz, 72° phase, 60% left duty ratio, and 30% right duty ratio. When the robot moves right, the maximum efficiency is 6.6 cm/s/W, which is achieved at 14 Hz, 324° phase, 20% left duty ratio, and 60% right duty ratio. Figure 4.16 shows the motion of the robot operating at the two operation points.

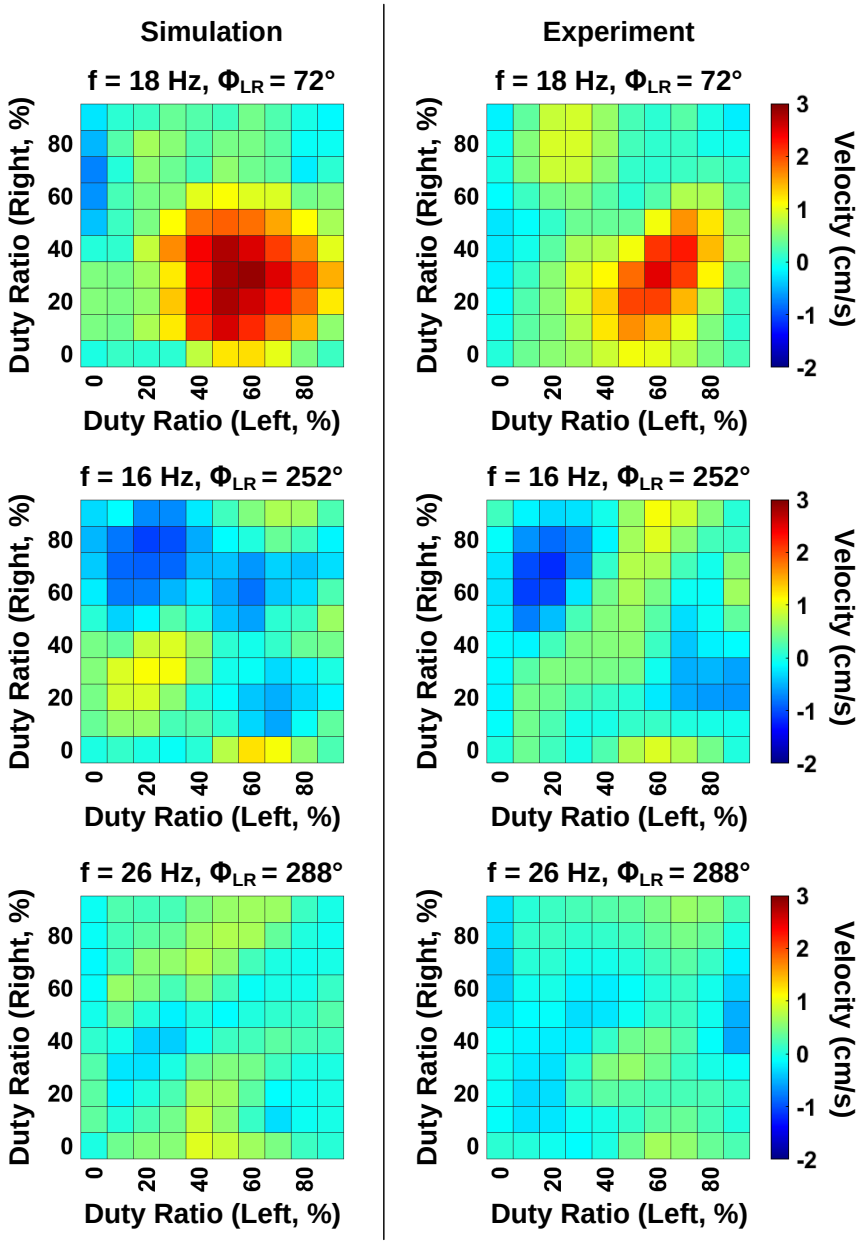

Figure 4.15: Simulated (left) and measured (right) soft robot velocity when both actuators are activated. The two actuators are driven at the same frequency f and a specific phase Φ_{LR}, as shown in the title of each graph, but at different duty ratios. Batteries at position #1.

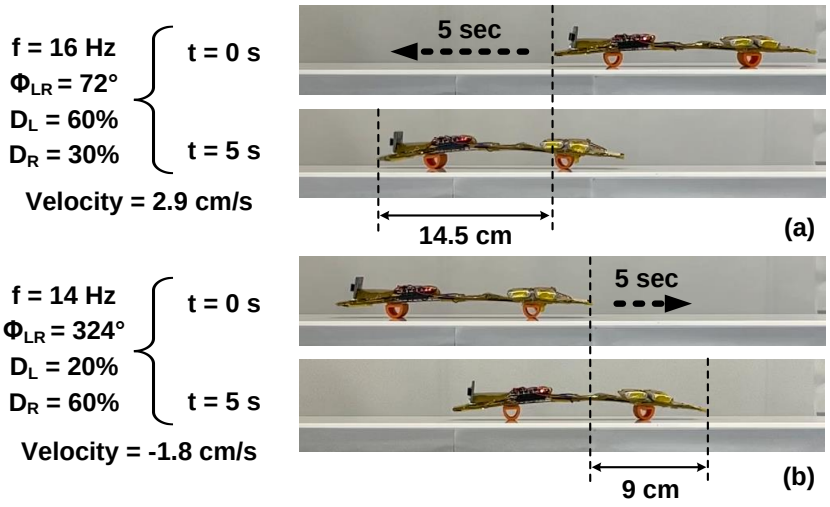

Figure 4.16: (a) eViper reaches 2.9 cm/s when operated at the maximum efficiency point of positive velocity. (b) eViper reaches -1.8 cm/s when operated at the maximum efficiency point of negative velocity.

4.5.4 Simulation Error Analysis

Root-mean-square error (RMSE) and Pearson Correlation Coefficient (PCC) are used to compare the simulation and experimental results at each frequency-phase combination. They are visualized as 2-D heat maps in Fig. 4.17. RMSE describes the absolute error between the simulated and measured velocity. PCC represents the correlation as a means of quantifying the similarity in shape of the velocity contour between simulation and measurement. RMSE and PCC jointly quantifies the applicability and limitations of SFERS. The RMSE is defined as:

$$RMSE = \sqrt{\frac{1}{N}\sum_{i=1}^{N}(X_i - Y_i)^2}. \tag{4.1}$$

The PCC is defined as:

$$PCC = \frac{\sum_{i=1}^{N}(X_i - \overline{X})(Y_i - \overline{Y})}{\sqrt{(\sum_{i=1}^{N}(X_i - \overline{X})^2)(\sum_{i=1}^{N}(Y_i - \overline{Y})^2)}}. \tag{4.2}$$

where i is the index of the data, N is the total amount of data in each frequency-phase combination, X_i and Y_i are the value of the simulation and experimental data at a specific index, and $\overline{X}$ and $\overline{Y}$ are the average values of the simulation and experimental results in a frequency-phase combination.

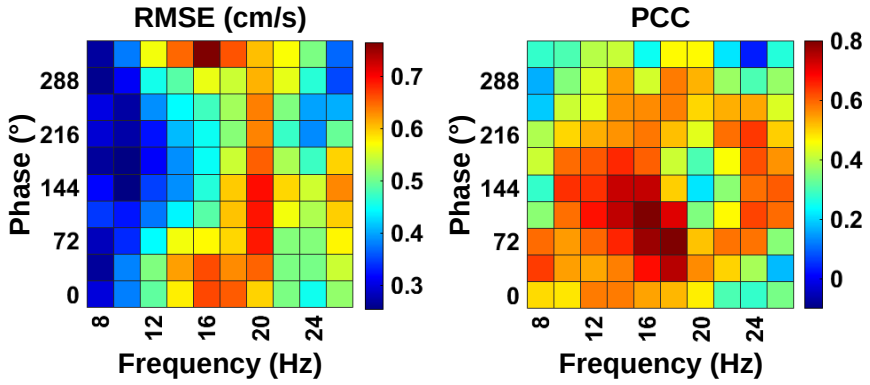

Figure 4.17: The root-mean-square error (RMSE) and Pearson Correlation Coefficient (PCC) of the simulated and measured velocity as a function of operating frequency and phase (for two-actuator operation).

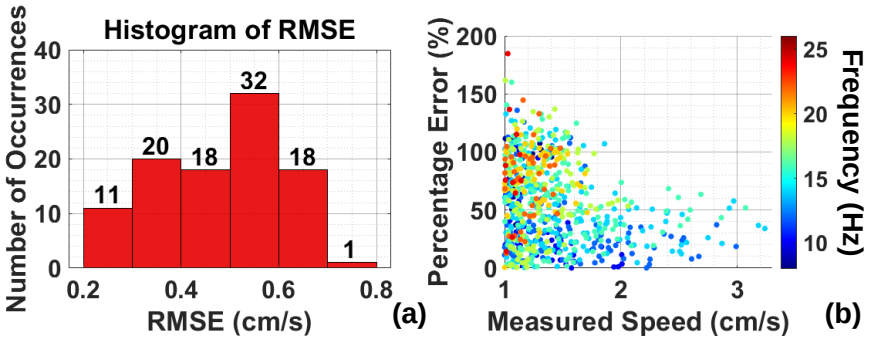

Figure 4.18: (a) Histogram of the root mean square error (RMSE) shown in Fig. 4.17. (b) Percentage error of the absolute velocity. The model is less accurate when the robot is moving slow (slower than 2 cm/s) and more accurate when the robot is moving fast (faster than 2 cm/s).

The result is presented in Fig. 4.17. For example, comparing the data in the top row of Fig. 4.15 results in an RMSE of 0.59 cm/s and a correlation coefficient of 0.8. The RMSE graph tells us that the errors at mid-range frequencies are relatively high. This could result from the fact that the velocities at mid-range frequencies have a larger absolute value, or it could also come from the simulation errors discussed in Section 4.4. At the right half of Fig. 4.17, there is a "ring-shaped" region in the middle of the graph where the PCCs are larger than 0.5, and the values at the corners and the center of the ring are less satisfactory. Figure 4.18(a) shows the histogram of the RMSE. RMSEs are generally below 0.8 cm/s. Figure 4.18(b) says that the model is less accurate when the robot is moving slow (slower than 2 cm/s) and more accurate when the robot is moving fast (faster than 2 cm/s).

4.6 Chapter Summary

This chapter examined the design, modeling, and locomotion behavior of the two-actuator eViper system. The mechanical and electrical implementation were first introduced, followed by an exploration of the robot's basic operation principles. To simulate soft robotic structure in a physics engine, the SFERS simulation framework was developed. The robot's locomotion velocity and power-to-velocity efficiency were compared across different driving conditions. Finally, discrepancies between simulation and experimental measurements were statistically analyzed.

5

Planar 2D Piezoelectric Robots

This chapter is based on work published in the following paper or currently under review:

- *H. Cheng, E. Veilleux, Z. Zheng, S. Wagner, N. Verma, J. C. Sturm and M. Chen, "eViper-2D: A Thin Large-Area Soft Robotics Platform," 2025 IEEE International Conference on Robotics and Automation (ICRA), Atlanta, GA, USA, 2025.*

- *H. Cheng, Z. Zheng, E. Veilleux, S. Wagner, N. Verma, J. C. Sturm and M. Chen, "eViper: A Scalable Untethered End-to-End 2D Soft Robotics Research Platform with Data Driven Modeling and Control," IEEE Transactions on Robotics (T-RO) (Under Review).*

5.1 Chapter Introduction

Soft robots are a promising approach for intelligent mechanical structures to interact with humans and the environment. Their deformable nature and high adaptability present unique advantages in unstructured settings [16, 54–56]. These capabilities make them particularly attractive for applications such as biomedical devices, search-and-rescue missions, and assistive technologies. Soft robots are often inspired by animals, as illustrated in Fig. 5.1. Previous research has demonstrated prototypes capable of motion on land [8–12, 57], in the water [13, 14], and in the air [15, 58].

Soft robots with 1D body structures have been extensively studied [20, 53, 57, 59]. Extending soft robot structures from 1D to 2D opens new opportunities and challenges. 2D soft robots offer unique strengths in (1) the potential for low-cost large-area fabrication and integration, leveraging large-area semiconductor technologies [60, 61]; (2) their versatile locomotion capabilities in complex environments [62].

Leveraging the scalable architecture of our soft robot design, this chapter focuses on presenting a complete 2D eViper platform which was expanded into a four-actuator configuration by placing the actuators in a 2D array. Each actuator operates independently, providing a high-degree-of-freedom control for the soft robot. By applying different electrical driving signals, the robot can move forward, backward, and rotate in both directions, achieving unrestricted untethered locomotion on a 2D surface. The robot is battery powered, can be controlled wirelessly, and can be made water-resistant to perform amphibious locomotion.

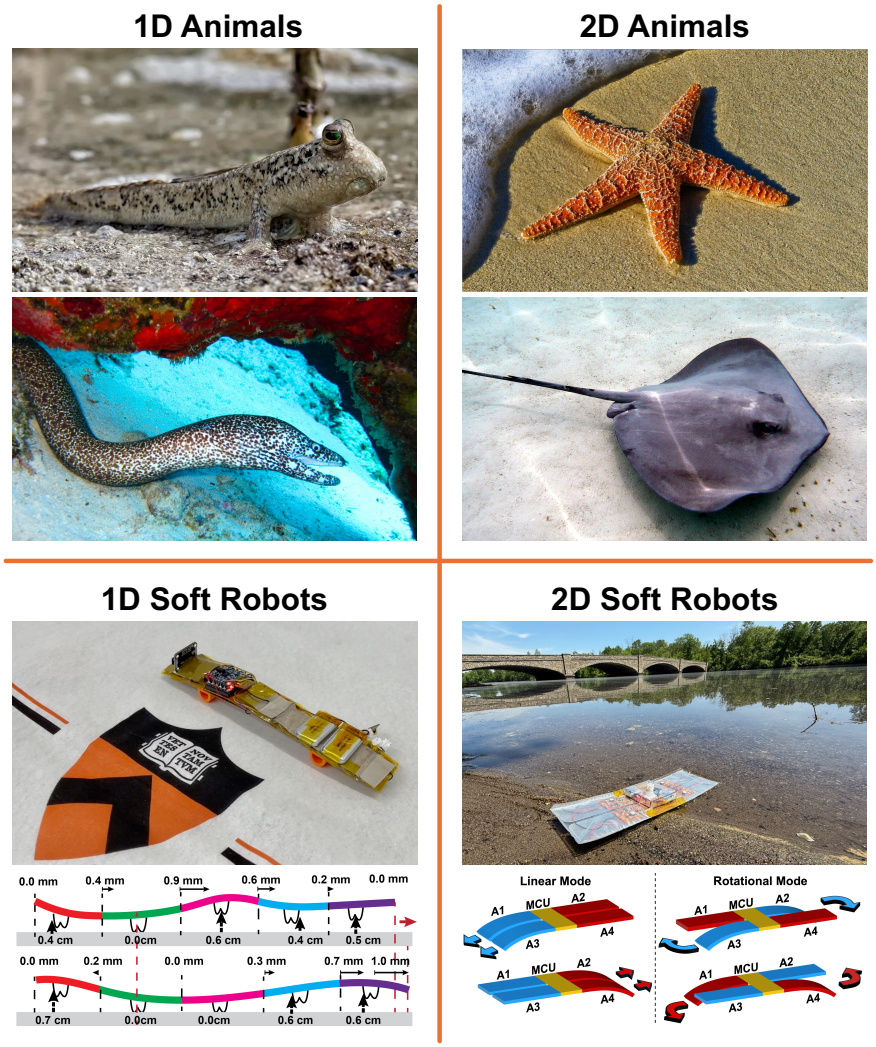

Figure 5.1: Inspired by natural creatures with varied body structures, eViper can perform both 1D and 2D actuation patterns and achieve agile locomotion. Compared to the previous 1D eViper, the 2D prototype exhibits greater control complexity and is capable of crawling, rotating, and swimming.

The eViper platform provides valuable insight into the modeling and design of the electrical and mechanical systems, motion dynamics, and data-driven control. Section 5.2 introduces the mechanical construction of the four-actuator eViper. Section 5.3 explains the robot's two basic operation modes. Section 5.4 investigates its basic locomotion behavior. Section 5.5 explores methods to calibrate the robot's inherent asymmetry and decouple linear and rotational motion. Section 5.6 presents the automated data acquisition framework, and a series of experiments for analyzing eViper's velocity variability, data-driven model, feedback control framework, and power-to-velocity conversion efficiency. In Section 5.7, the amphibious eViper is introduced and its

performance across driving waveforms and operating frequencies are recorded. Section 5.8 studies the cost of transport (COT) of eViper and compare it across multiple untethered soft robotic systems. Finally, Section 5.9 summarizes this chapter.

5.2 Hardware Implementation

The example 2D eViper platform has a multilayer mechanical structure as shown in Fig. 5.2(a). It is 265 mm long, 75 mm wide, and weighs 67.3 g. Components required for different functionalities are distributed across separate layers to enable scalable and flexible manufacturing and assembly, with their weight distribution shown in Fig. 5.2(b). The piezoelectric actuators are commercial Macro Fiber Composite units (MFC) from Smart Material Corporation [33], each measuring $100\times20\times0.3$ mm (length$\times$width$\times$thickness). Four MFC actuators are bonded to a single steel sheet cut in an "H" pattern. Eight strain sensors are attached to the upper side of the steel sheet to monitor the physical behavior and enable future feedback control. The strain sensor connectors feed the signals to the analog-to-digital converter (ADC) of the microcontroller unit (MCU). A customized 4-layer flexible printed circuit board (PCB) sits on the steel sheet and drives the actuators. The combined thickness of the actuators, steel sheet, and the PCB is less than 1 mm.

Fig. 5.2(c) illustrates the basic operating principle of a single steel-bonded piezoelectric actuator. The Young's modulus is 30 GPa for the actuator and 190 GPa for the steel sheet. When high voltage is applied to an actuator, it tries to contract, but it bends concave downward instead due to the higher compressive stiffness of the steel sheet. When discharged, the actuator returns to its original configuration.

As shown in Figs. 5.2(d) and 5.2(f), both the steel sheet and the PCB are configured in an "H" shape, with the microcontroller sitting in the middle interconnection. Seven 3D-printed plastic feet are attached to the bottom of the robot. They prevent the actuators and associated electrical connections from making direct contact with the ground during actuation. These feet have spherical tips to ensure uniform contact between the robot and the ground during operation.

There are two infrared-reflective markers and an infrared light-emitting diode (LED) on the

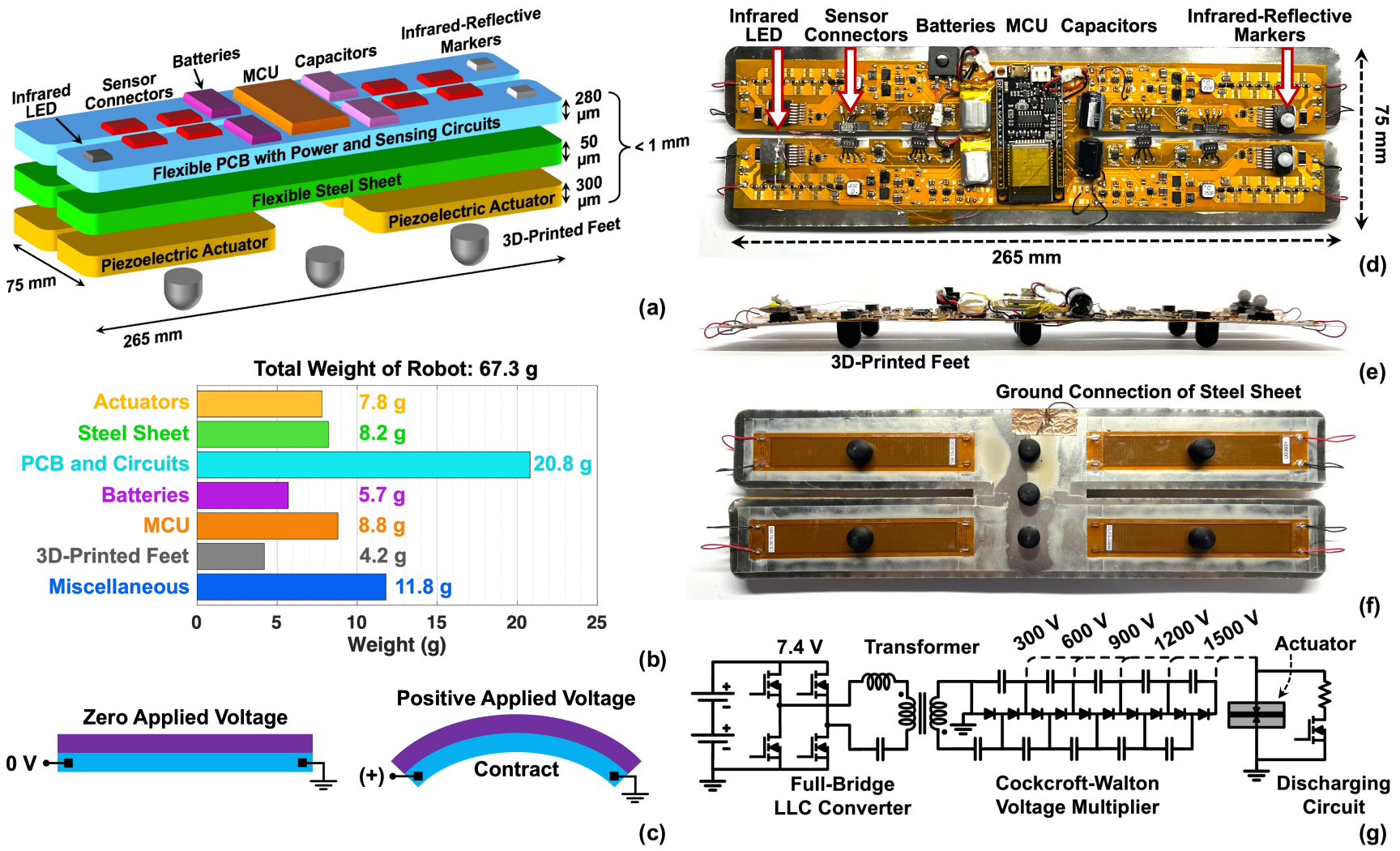

Figure 5.2: Breakdown of eViper's (a) mechanical structure and (b) weight across components. (c) An illustration of a steel-bonded MFC piezoelectric actuator. The purple layer is the steel sheet, and the blue layer represents the actuator. (d) Top view, (e) side view, and (f) bottom view of the prototype. (g) The circuit schematic of a power converter module. The output of the circuit is configurable between 300 V and 1500 V, depending on the number of stages in the Cockcroft-Walton voltage multiplier. The gate signals of all MOSFETs are controlled by the onboard MCU. The dimensions are not to scale in (a).

Table 5.1: Notations and Definitions for Locomotion Analysis

Notation	Definition
A1, A2, A3, A4	Actuator #1, #2, #3, or #4 as shown in Figs. 5.3 and 5.4(b).
CW, CCW	Clockwise (CW) or counterclockwise (CCW) rotation.
f	Driving frequency of all actuators.
T	Period of the driving waveform. $T = 1/f$.
ϕ_{12}	Phase between the driving waveforms of A1 and A2. Phase, when expressed as a percentage, is the fraction of a period T between the rising edges of the two signals.
D_1	Duty ratio of A1's driving signal. Duty ratio, when expressed as a percentage, is the fraction of a period T that a signal remains at the high level.
$D_{1,3}$	Duty ratio of A1 and A3's driving signals.
v_x	Linear velocity along the x axis. Positive rightward.
v_y	Linear velocity along the y axis. Positive upward.
ω	Angular velocity. Positive counterclockwise.

prototype for high-speed motion tracking. To ensure electrical safety, the steel sheet is connected to the electrical ground of the PCB, and, if necessary, the PCB can be insulated with Kapton tape [12].

The power source consists of two 3.7 V, 100 mAh lithium polymer batteries connected in series, providing a 7.4 V input to the electrical system. Two 2.2 mF electrolytic capacitors help buffer the voltage buses on the robot. The average power rating of the robot is about 2 W (including the MCU). The batteries last for about 20 minutes. Fig. 5.2(g) shows the schematic of the onboard power converter introduced in Chapter 3. Other driving strategies [45, 63, 64] can be adopted to further improve the energy efficiency of the electrical system. The onboard MCU communicates with a PC through Bluetooth, and it regulates the converters to drive the actuators with various electrical signals. A current sensor measures the current (and power) consumption of eViper.

5.3 Operating Principles of the Prototype

Each actuator in eViper can be operated independently, offering a very high-degree-of-freedom control. For simplicity, this section focuses on two distinct modes of operation: the "linear" mode and the "rotational" mode. Additional behaviors and exceptions are discussed in later sections.

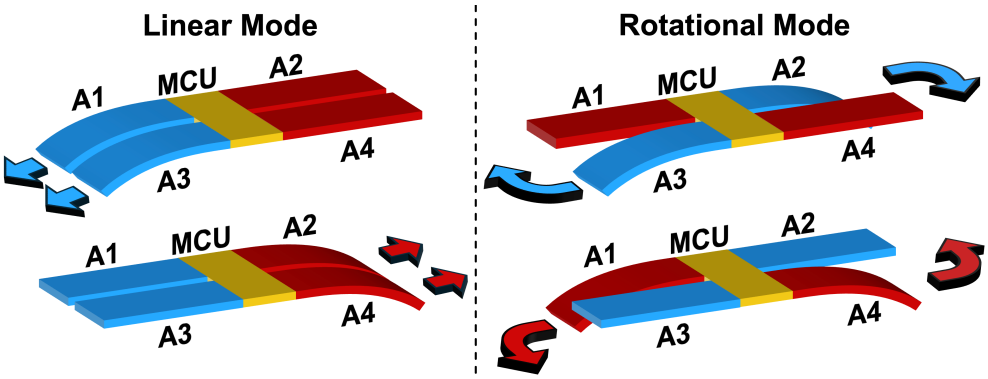

Figure 5.3: The operating principles of the "linear" and "rotational" mode. The MCU sends the same electrical signal to drive the actuators marked with the same color. Two distinct electrical signals are required to drive the two different pairs of actuators. An example is provided in Fig. 5.4.

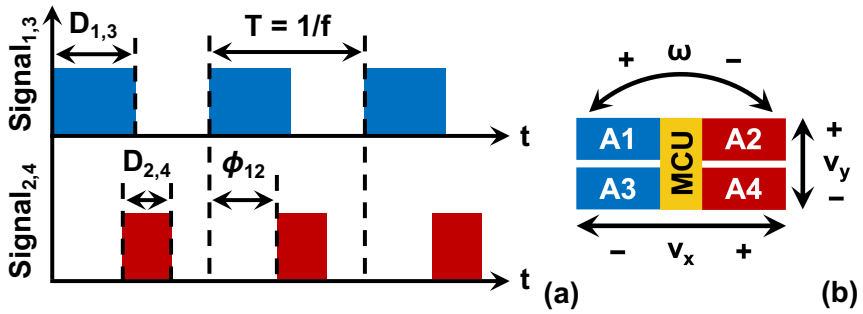

Figure 5.4: (a) An example showing the two actuator driving signals in the "linear" mode with specific frequency (f), phase (ϕ_{12}), and duty ratio ($D_{1,3}$ and $D_{2,4}$). (b) The definition of linear velocities (v_x and v_y) and angular velocity (ω), and the number assignment of the actuators. In (a), the upper waveform, $\text{Signal}_{1,3}$, is sent to A1 and A3 while the lower waveform, $\text{Signal}_{2,4}$, is sent to A2 and A4.

Table 5.1 summarizes the notations used to analyze eViper's driving waveforms and locomotion. Fig. 5.3 illustrates the basic cases where only one pair of actuators is active while the other pair is idle. In the "linear" mode, actuators A1 and A3 receive the same electrical driving signal from the MCU, and the same applies to A2 and A4. The robot principally moves forward or backward along its longitudinal axis. Non-ideal rotation can occur due to the actuator asymmetry and characteristic variation. On the other hand, in the "rotational" mode, A1 and A4 operate in phase, as do A2 and A3. The robot rotates clockwise (CW) or counterclockwise (CCW) in this mode. The center of mass of eViper exhibits slight displacement due to a small radius of rotation. The onboard power electronics can drive the prototype with various high-voltage square waves. Fig. 5.4 shows an example of driving waveforms with frequency, phase, and duty ratio as control variables.

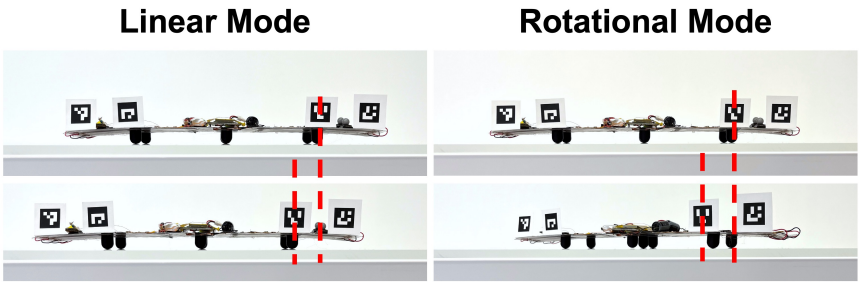

Figure 5.5: The experimental setup for basic motion analysis. The setup can be used to understand the mechanisms of linear and rotational motion since the markers exhibit horizontal displacement in both cases (refer to Fig. 5.6).

5.4 Basic Robot Motion

Fig. 5.5 shows the experimental setup for recording the soft robot motion through a slow-motion camera. Four ArUco markers are placed from left to right: at the left edge, left foot, right foot, and right edge of the robot. The locomotion is recorded by the camera (240 frame/s) and analyzed using the OpenCV software library in Python. One pair of actuators is activated at a time while the other remains idle. This results in the four different cases shown in Fig. 5.6(b). The blue line depicts the z-axis position of the marker, labeled in Fig. 5.6(a), on an active actuator. The periodic waveform represents the regular bending behavior. The orange line shows the x-axis position of the marker on an idle actuator. It shows how the idle actuator moves along the x-axis. The purpose of these figures is to show how the idle actuators are passively "dragged" by the recurrent bending and relaxation behavior of the active ones. Overall, the robot moves in a stepwise manner corresponding to the actuation cycle of the active actuators. The prototype reaches a new local extreme point, in terms of the x-axis position, when the active actuators bend concave down (step 2 in Fig. 5.7). The exception is clockwise rotation, during which the robot reaches a local minimum x-axis position as the active actuators relax.

Fig. 5.6 illustrates that leftward motion results from driving A1 and A3, and rightward motion results from driving A2 and A4. Driving A2 and A3 produces clockwise rotation, and driving A1 and A4 produces counterclockwise rotation. These four cases exhibit a consistent characteristic: the active actuators generate an outward thrust, thereby developing a lateral force in the "linear" mode and a torque in the "rotational" mode. Fig. 5.7 presents a qualitative understanding of the

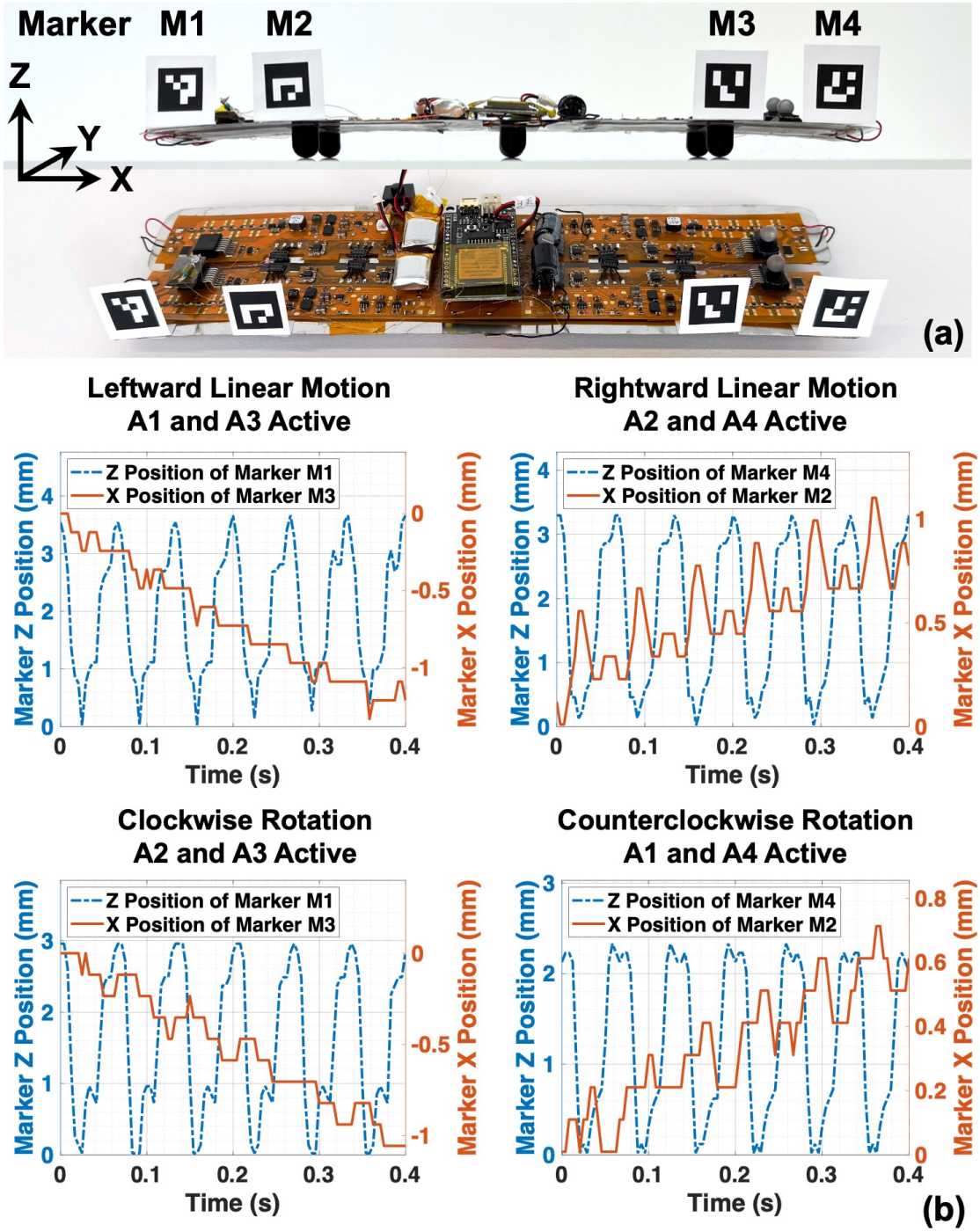

Figure 5.6: (a) The experimental setup. The reference x-, y-, and z-axes and labels assigned to the four ArUco markers are shown. (b) Motion analysis results of the four basic motion types. In each figure, the blue line represents the z position of the marker that sits on an active actuator, exhibiting periodic behavior corresponding to the actuator bending cycles. In contrast, the orange line illustrates the x position of the marker that sits on an idle actuator. It moves in the positive or negative x direction based on how the robot is driven. The orange line demonstrates a step-like behavior which synchronizes with the actuation cycle of the active actuators. The active actuators are driven at 15 Hz, no phase shift, and 50% duty ratio in all cases.

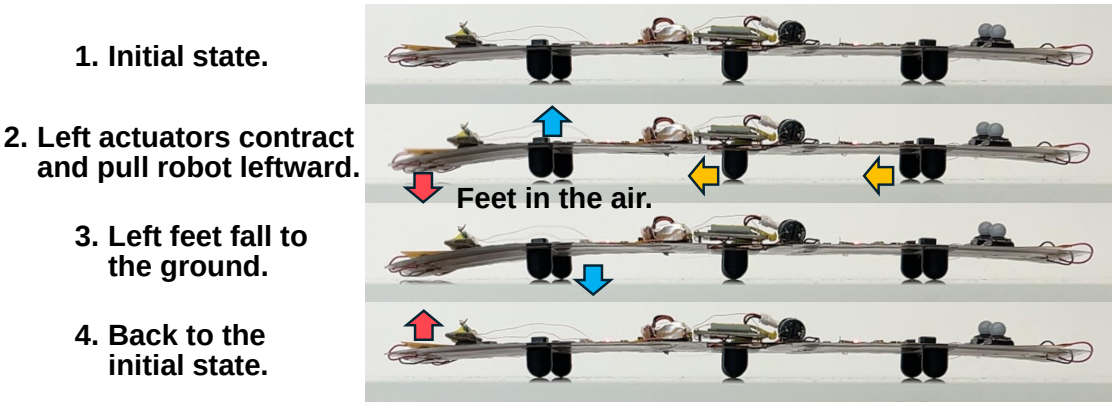

Figure 5.7: Observation of leftward linear motion when only driving the two left actuators (actuators #1 and #3). 1. Initial state. 2. The actuators bend in response to a square wave excitation. The middle part of the actuators shoots up and raises the left feet into the air. The upward momentum reduces the normal force and friction between the robot and the ground, and the actuator contraction pulls the right half of the soft robot body leftward. 3. The left feet fall to the ground due to gravity. 4. The actuators are discharged. The right half of the robot stays in the new position due to a higher friction with the ground (no upward momentum to reduce normal force).

motion mechanism based on observations from slow-motion videos.

The prototype is designed to be symmetric. However, the four orange traces in Fig. 5.6 show different characteristics. The trace corresponding to leftward linear motion is generally step-like, whereas the trace for rightward motion is more spiky. Combined with the previously mentioned fact that clockwise rotation exhibits different locomotion behavior from the other three cases, it is evident that the four actuators have different dynamic responses even when driven by the same electrical signal, leading to asymmetries. In addition to the factors introduced in Section 2.6, nonuniform flexibility and weight distribution across the PCB could also contribute to these non-ideal effects.

These factors lead to non-ideal drift or rotation during locomotion of eViper, motivating the development of data-driven modeling and feedback control that will be discussed in Section 5.6. In the following sections, the robot's motion on a 2D plane is decomposed into three components: linear velocity along the x-axis (v_x), linear velocity along the y-axis (v_y), and angular velocity (ω). Their reference axes are labeled in Fig. 5.4(b). In the context of linear motion, v_y and ω are considered results of non-ideal drift, as the robot is primarily designed to move along the x-axis. When eViper rotates, small values of v_x and v_y also occur due to drift.

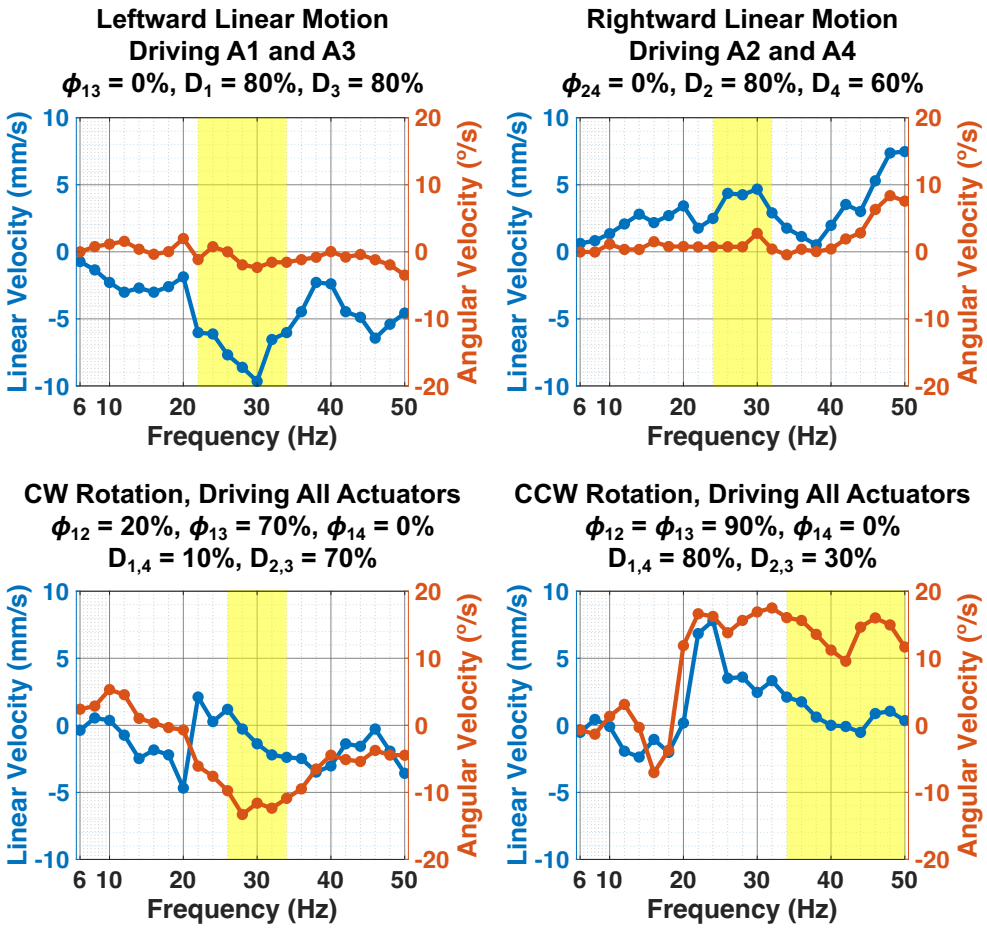

Figure 5.8: Frequency sweep results for four actuation patterns that produce bidirectional linear motion and rotation. The corresponding v_x and ω are plotted, with the yellow shaded areas indicating the desired ranges of operating frequency. For linear motion, the desired frequency range is characterized by high $|v_x|$ and low $|\omega|$. For rotation, low $|v_x|$ and high $|\omega|$ are preferred. To mitigate non-ideal drift in the system, the driving waveforms are fine-tuned and do not strictly follow the "linear" and "rotational" mode conventions introduced in Section 5.3.

5.5 Empirical Locomotion Control

When all four actuators of eViper are active, or when the robot is operated at higher frequencies, its dynamics become more complex, and the effects of non-ideal drift are more pronounced. Despite these challenges, this section presents multiple experimental results to demonstrate that the robot can be controlled to exhibit desired behaviors by selecting appropriate electrical driving parameters. Fig. 5.8 shows examples of leftward and rightward linear motion, as well as clockwise and counterclockwise rotation. In each example, the operating frequency is swept from 6 Hz to 50 Hz with a step size of 2 Hz, while the phase and duty ratio are fixed. The resulting linear velocity (v_x)

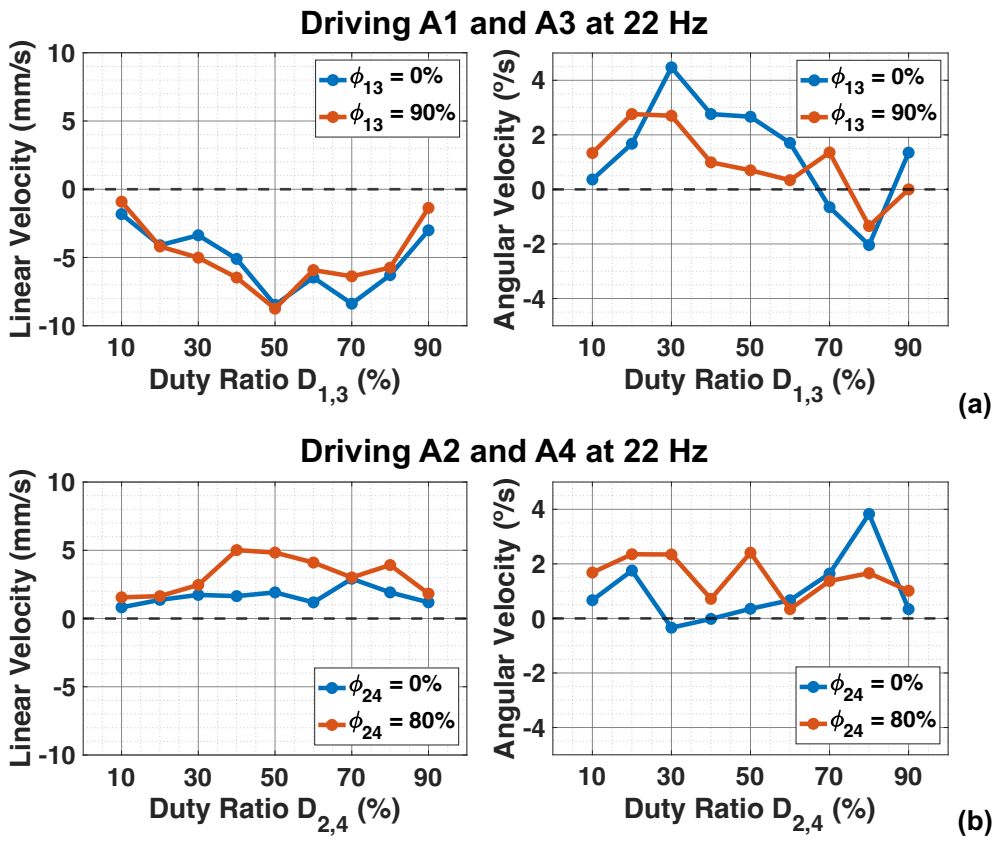

Figure 5.9: Comparison of eViper performance before and after the introduction of phase shift calibration. (a) Driving A1 and A3 at 22Hz. (b) Driving A2 and A4 at 22 Hz. In each case, the linear velocity (v_x) and the angular velocity (ω) are plotted.

and angular velocity (ω) are plotted. For leftward linear motion, the prototype achieves high $|v_x|$ and negligible $|\omega|$ from 22 to 34 Hz, indicating ideal behavior. The same is observed between 24 and 32 Hz for rightward motion. In the case of clockwise rotation, $|\omega|$ is high and $|v_x|$ remains low from 26 to 34 Hz, while ideal counterclockwise rotation occurs when the operating frequency is above 34 Hz. These results demonstrate the robot's ability to perform controllable, bidirectional linear motion and rotation despite facing internal asymmetries. eViper can reach any position on a 2D plane by combining the four actuation patterns described above.

Fine-tuning the phase shift between actuators is an effective method for calibrating linear-mode driving patterns with noticeable non-ideal rotation. Fig. 5.9(a) compares the scenarios where A1 and A3 are driven at 22 Hz with different phase shifts between them. $\phi_{13} = 0\%$ represents the base case, while $\phi_{13} = 90\%$ represents the calibrated case. The angular speed ($|\omega|$) is lower in the

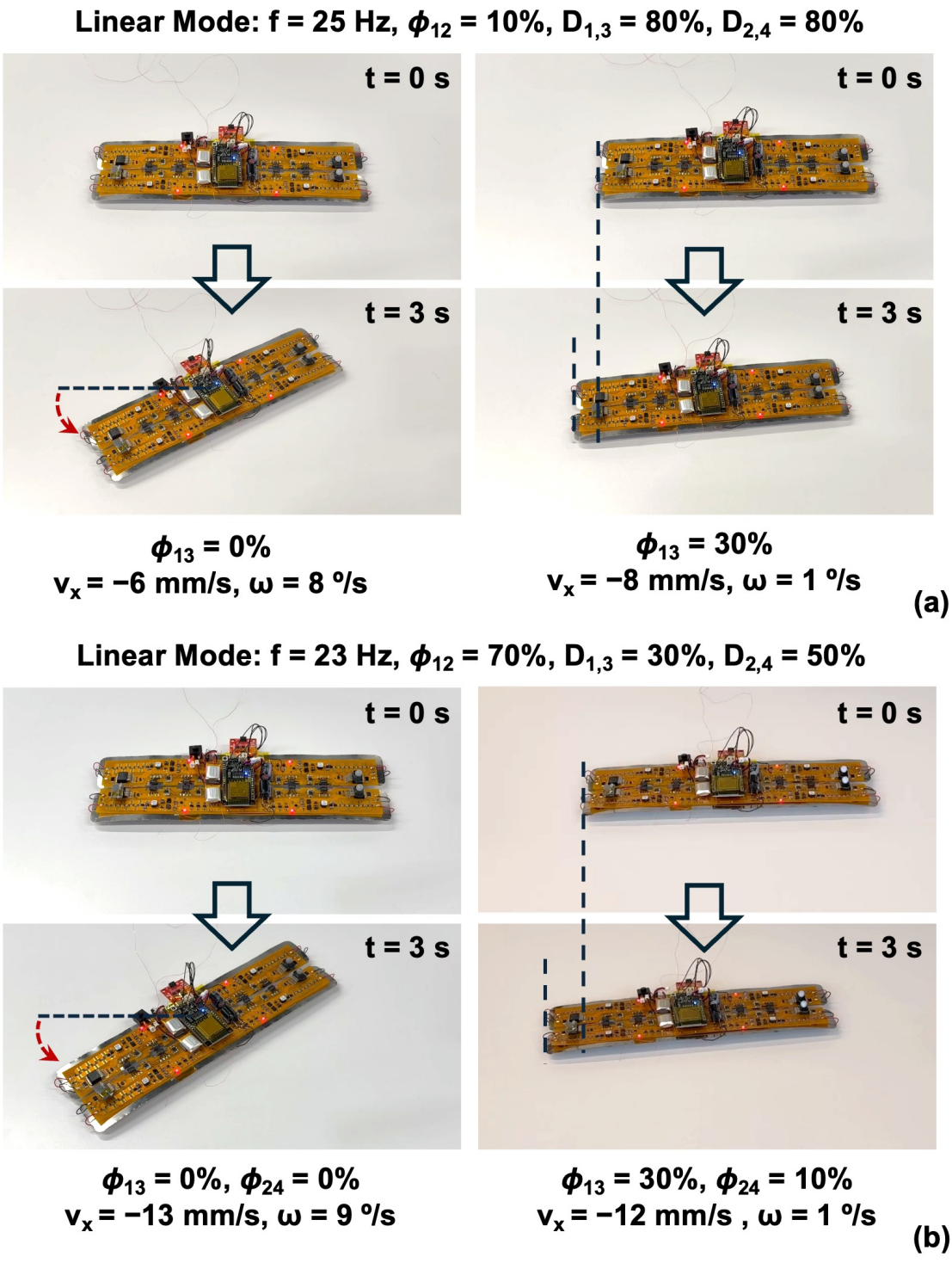

Figure 5.10: The locomotion of the prototype before (first and third columns) and after (second and fourth columns) introducing phase shift for the calibration of structural and actuation asymmetry. The prototype demonstrates linear motion and minimal rotation after applying the phase shift. When the phase shift was applied, actuator A3 lagged A1, and actuator A4 lagged A2.

presence of a phase shift for the majority of the operating duty ratio. The profiles of linear velocity are similar between the two cases, indicating that introducing a phase shift improves linearity in the robot's motion. Similarly, in Fig. 5.9(b), when A2 and A4 are driven at 22 Hz without a phase shift, greater rotation is observed at higher duty ratios. Adding a phase shift reduces the rotation in that region and increases the overall linear velocity. These results demonstrate that phase shift calibration is an effective strategy for enhancing linear motion performance, motivating model-based or data-driven feedback control.

Introducing a phase shift can also modulate the robot's locomotion when all four actuators are active. Fig. 5.10 shows two scenarios. In both cases, the robot exhibits rotation when operated in linear mode. After applying a phase shift to the actuators, the robot moves primarily in a linear fashion. This indicates that phase shifting can mitigate the effects of asymmetries on the robot's locomotion. The optimal phase shift depends on the driving parameters and the aging effects of actuators. Therefore, active sensing and feedback control are necessary for practical deployment of eViper.

5.6 Data-Driven Methods and Results

In this section, eViper was driven in either the "linear" mode or the "rotational" mode outlined in Section 5.3, Fig. 5.3, and Fig. 5.4. In the linear mode, A1 and A3 operate in phase and have the same duty ratio, and the same applies to A2 and A4. In the rotational mode, A1 and A4 operate in phase and have the same duty ratio, as do A2 and A3.

5.6.1 Velocity Response under Parameter Sweep

To examine eViper's velocity response under similar but distinct sets of electrical driving parameters, a parameter sweep was conducted for both linear and rotational motions, as illustrated in Fig. 5.11. Each set of driving parameters consisted of four variables (f, ϕ_{12}, D_1, and D_2). Only one parameter was swept at a time, while the other three were held constant. The frequency was swept from 6 Hz to 50 Hz, with a step size of 2 Hz. The phase and duty ratios were varied from 0% to 90%, each with a step size of 10%. The linear velocity v_x and angular velocity ω were plotted for

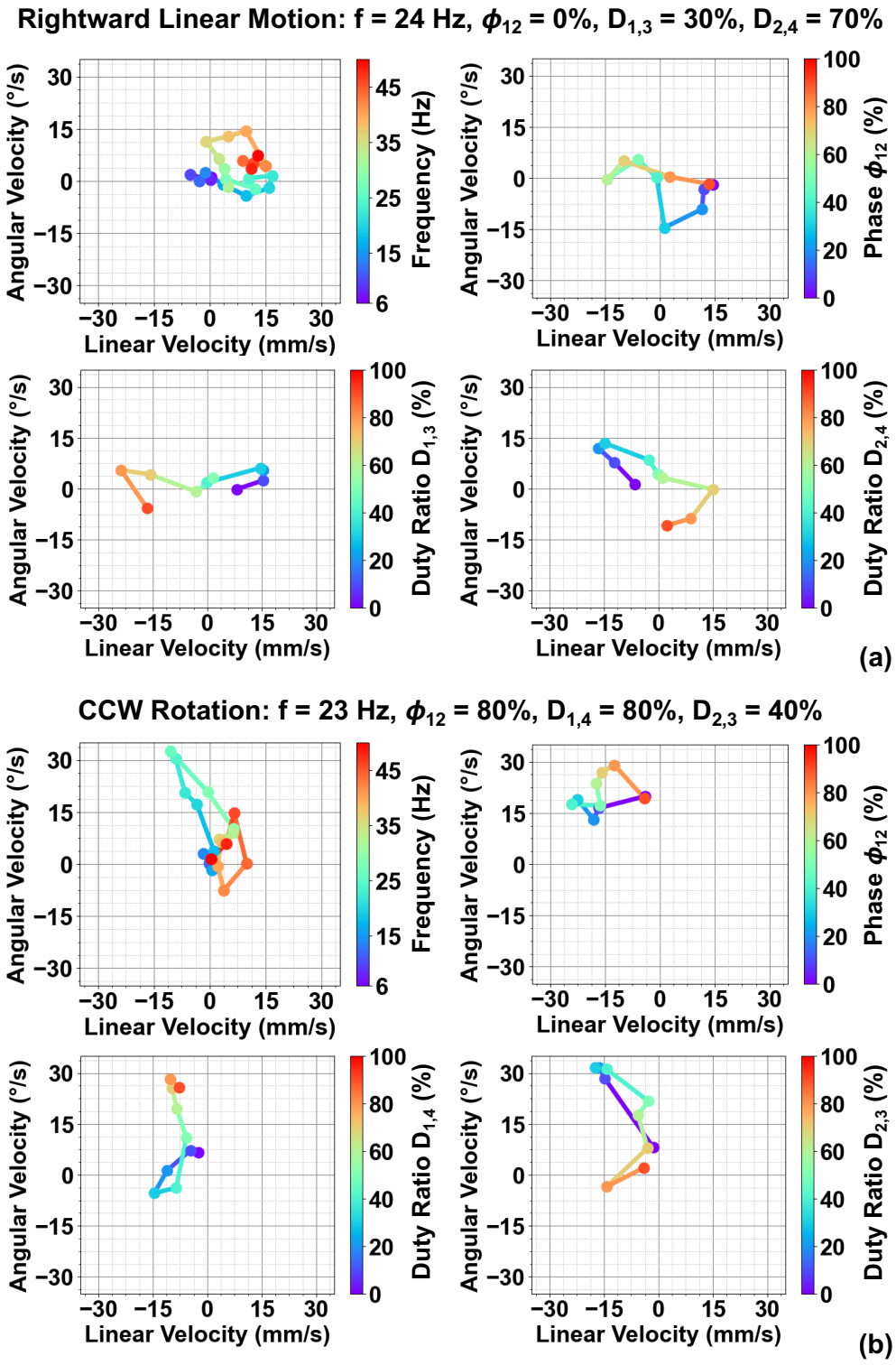

Figure 5.11: Results of parameter sweep for (a) a rightward linear motion and (b) a counterclockwise (CCW) rotation. The linear velocity v_x and angular velocity ω are plotted, with the color bar indicating the swept parameter. The paths shown in the figures illustrate the robot's behavior as the swept parameter increases from lower to higher values. No clear pattern can be observed in the results, suggesting that the dynamics of eViper are complex.

each result. The color bar in each graph represents the parameter being swept. The parameters used in Fig. 5.11(a) originally produced rightward linear motion (positive v_x); however, many leftward motions (negative v_x) were observed during the sweep. Similarly, the parameters in Fig. 5.11(b) initially generated a counterclockwise rotation, but the robot exhibited clockwise rotations at certain sets of driving parameters. These results suggest that the robot's motion dynamics are highly nonlinear and complex, motivating the application of data-driven methods to analyze and model eViper's behavior.

5.6.2 Automated Data Acquisition

To better understand the complex motion of eViper, the robot was driven with a wide variety of driving signals, whose waveform parameters were randomly generated, and the resulting linear and angular velocities were recorded. The procedure for automated data acquisition is as follows: (1) determine the robot's operating mode ("linear" mode or "rotational" mode); (2) the microcontroller randomly generates driving parameters (frequency, phase, and duty ratio); (3) the microcontroller and power electronics drive the prototype for three seconds; (4) the robot idles for three seconds; and (5) revisit step 2 if there is no user-triggered stop signal.

The randomly generated frequencies ranged from 6 Hz to 50 Hz, with a step size of 1 Hz. The phase and duty ratios ranged from 0% to 90%, each with a step size of 10%. In each set of driving parameters, the operating frequency was the same across all four actuators. The robot was operated on a smooth acrylic board during data collection unless otherwise stated. The robot also functioned on smooth surfaces of different textures, such as foam sheets, cotton cloths, and engineered hardwood, and the velocity responses varied due to differences in surface friction. Further research is required to assess the robot's adaptability to rugged environments.

A Vicon Vantage V16 motion-capturing camera system was utilized to record the robot's motion. The system takes infrared light at 850 nm as input and requires at least three infrared markers to be installed on the object for tracking. There are two passive infrared-reflective markers and one active infrared LED on the robot. The LED serves as the third infrared marker. It only turns on during step 3 of the above procedure, which serves the purpose of synchronizing the camera system with

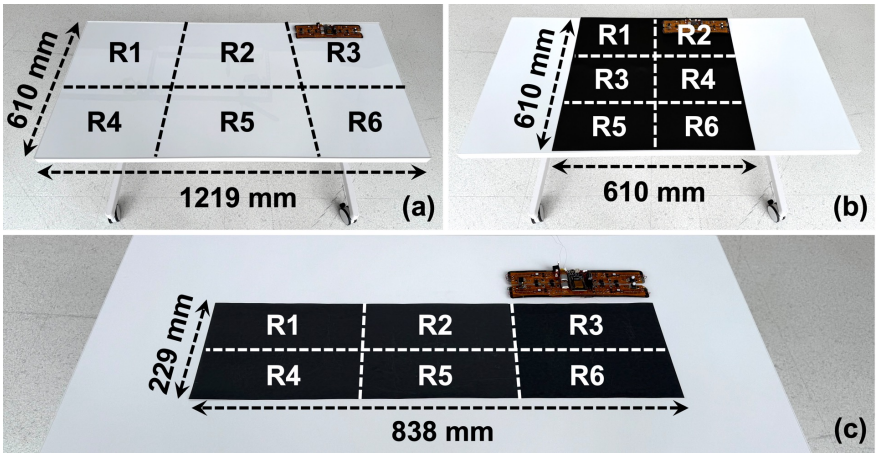

Figure 5.12: The surface partitions of (a) transparent acrylic board, (b) black foam sheet, and (c) sandpaper with a grit size of 2500, for the velocity variability measurements.

the robot. An onboard current sensor measures the current and power consumption of the robot. A total of 3500 data points were recorded with the motion capturing camera and the current sensor. Each data point includes linear velocities v_x and v_y, angular velocity ω, and power consumption.

5.6.3 Velocity Variability Due to Surface Condition

This section aims to characterize the noise in the measured velocity data and to investigate the robot's behavioral response on a tilted surface. eViper's locomotion relies on the friction between its feet and the ground, and it is also influenced by vibrations and jumping motions generated by actuator dynamics. Nonuniform surface conditions may introduce noise into the system, leading to unpredictability in the prototype's linear and angular velocities. This surface-dependent behavior causes eViper to exhibit different velocities across various materials, motivating the following comparative analysis.

Experiments were conducted to evaluate eViper's velocity variability by driving it on three different materials: transparent acrylic boards, black foam sheets, and sandpaper with a grit size of 2500. During the automated data acquisition process described earlier, the acrylic board was considered to be an ideal surface, and the robot was allowed to move freely across the entire board area (i.e., it did not start from the same location for each actuation pattern). To better simulate the inherent noise in the actual data collection process, each of the three surface materials was partitioned into six regions, labeled R1 through R6, as shown in Figs. 5.12(a) to 5.12(c). The robot

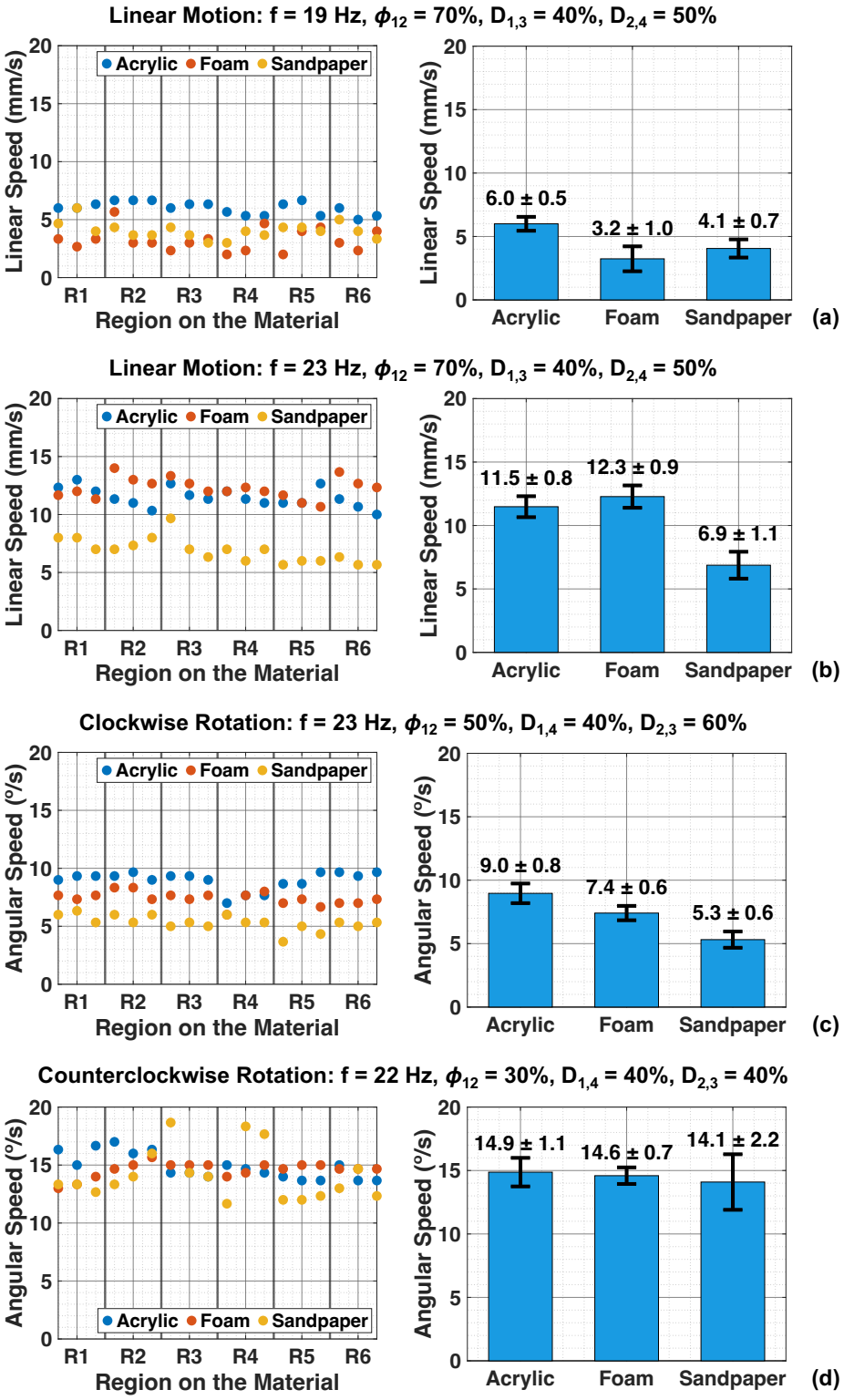

Figure 5.13: The velocity variability measurement results. (a) to (d) show results for four different actuation patterns across multiple trials. The left column shows the trials conducted per actuation pattern on each material. The right column presents the mean robot speed ($|v_x|$ or $|\omega|$) and the corresponding standard deviation. The standard deviation represents the noise in the measured speeds.

was driven with the same actuation pattern three times consecutively in each region, resulting in a total of eighteen trials per pattern on each material. Figs. 5.13(a) to 5.13(d) present the experimental results. The left column displays the measured speed ($|v_x|$ or $|\omega|$) of each trial, while the right column shows the mean and standard deviation of those data. The standard deviation is used as a measure of noise intensity.

Fig. 5.13 illustrates that eViper exhibits different mean speeds and standard deviations depending on the surface material. These results indicate that the robot is highly sensitive to variations in surface contact — and therefore friction — between its feet and the ground. Rows (a) and (b) compare two linear motions with identical actuation parameters except for the driving frequency. The comparison reveals the frequency sensitivity of eViper's locomotion.

The performance of eViper on a tilted surface was also measured by using the same actuation patterns and materials, as depicted in Fig. 5.14. The tilt angle ranged from 1º to 5º, and three trials were conducted at each angle. For the two linear motions, the robot moved leftward on a flat surface. On the tilted surface, the left end was elevated, meaning that the slope opposed the robot's leftward motion. As the tilt angle increased, the robot's leftward velocity gradually decreased. On some materials, the velocity became negative at larger tilt angles, indicating that the robot slid downhill. Clockwise and counterclockwise rotations were also tested, but no clear relationship was observed between the robot's angular velocity and the surface angle.

It is difficult to quantify the velocity variability across the entire dataset, or to determine which surface is most suitable for eViper's operation, since the robot's friction sensitivity, slope sensitivity, and noise level vary for each set of actuation parameters. Nevertheless, the collected data provide valuable insights into eViper's velocity variability and serve as a useful reference for understanding its response to diverse environments and driving parameters. The measured noise levels also highlight a fundamental limitation in the system's predictability when using data-driven models under uncontrolled surface conditions.

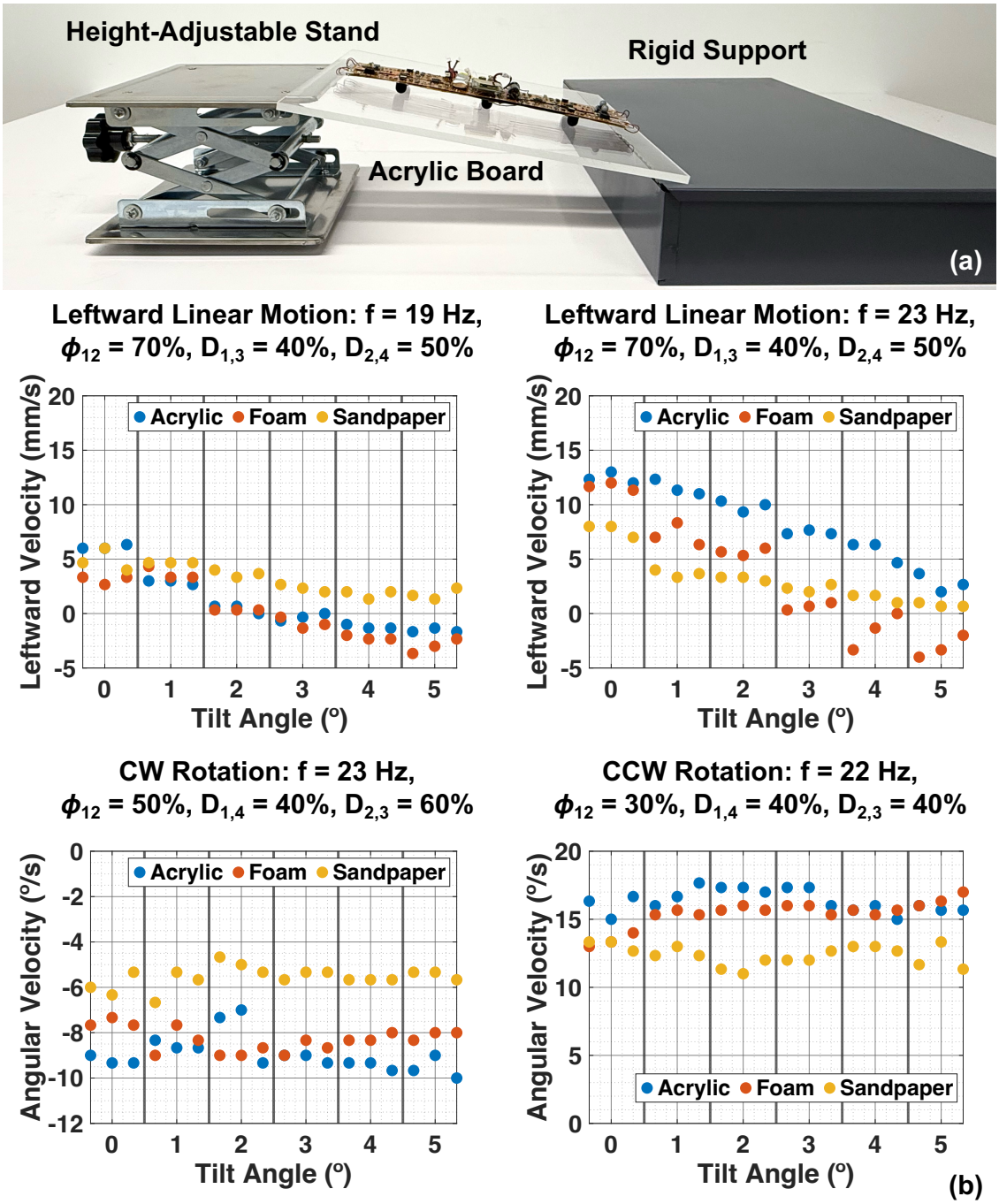

Figure 5.14: Characterization of velocity variability on a tilted surface. (a) Experimental setup. A height-adjustable stand was used to adjust the tilt angle of the surface. The tilt angle shown in the image is exaggerated for demonstration purposes. The foam sheet and sandpaper were laid on the acrylic board during testing. (b) Experimental results. Three trials were conducted for each tilt angle. The robot's linear motions were significantly affected by the slope, with negative velocities indicating that the robot slid downhill at larger tilt angles. The relationship between eViper's angular velocity and the surface angle was weak. Note: the robot moved leftward on a flat surface for both linear motions. In this figure, leftward velocities are plotted as positive for clarity and readability.

5.6.4 Data-Driven Models and Operating Regions

The prototype's motion dynamics are nonlinear and complex when all four actuators are active. One approach to analyzing this complexity is through neural networks. Considering the amount of available training data, a small neural network was adopted in this work. A smaller model requires less data to generalize and is less prone to overfitting. Developing differentiable models also presents opportunities for future investigation into advanced control strategies for eViper.

With the 3500 collected data points, two independent feedforward neural network models were created to predict v_x, v_y, and ω in the "linear" and "rotational" modes based on the robot's operating frequency, phase, and duty ratio. The structure of these models is presented in Fig. 5.15. A key

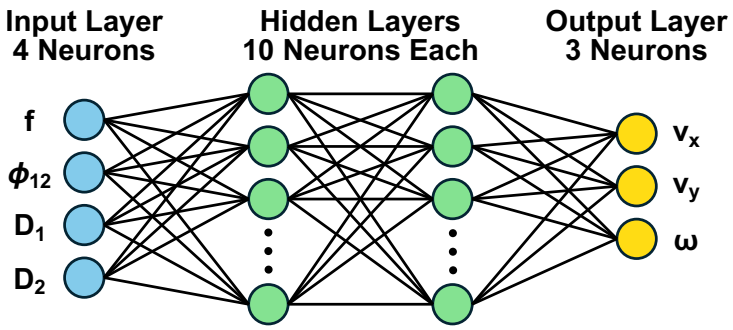

Figure 5.15: Structure of a feed-forward neural network model for eViper. Each model has 4 input parameters, 3 output parameters, and 2 hidden layers. The model contains 193 parameters.

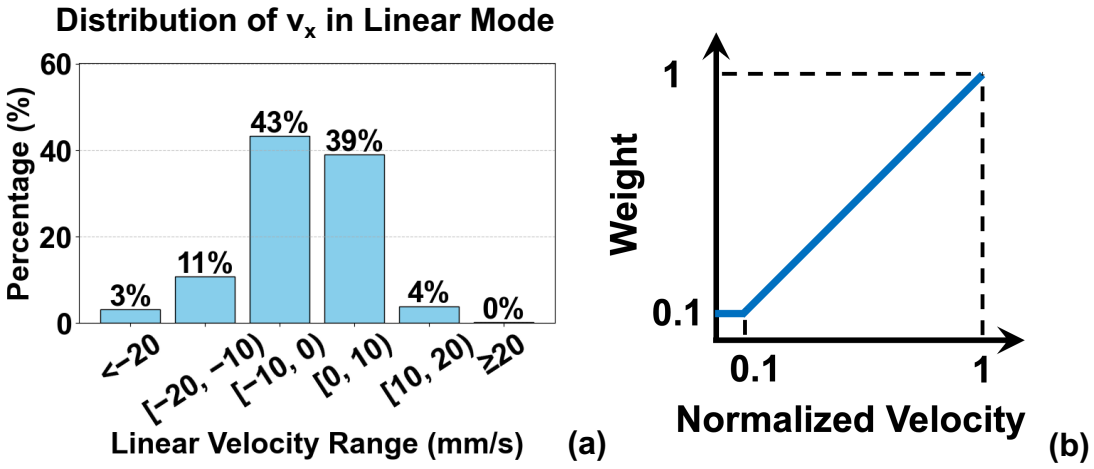

Figure 5.16: (a) Histogram showing the nonuniform distribution of v_x in the linear mode dataset. The distribution of ω in the rotational mode dataset is similar. (b) The weight function that is applied to each data point during the training process of the two models. The weight is applied according to the normalized velocity and has a lower limit of 0.1.

challenge in training the models is the severe imbalance in velocity distribution within the dataset. Fig. 5.16(a) shows the distribution of v_x in the linear mode dataset. Because the driving parameters were randomly generated for each data point, more than 80% of the collected data lack meaningful linear motion as they have a $|v_x| < 10$ mm/s. High-velocity data points are scarce. The objective of training the model is to identify sets of driving parameters that result in high-velocity locomotion. However, the imbalance of the dataset makes this task even more challenging.

To improve the model's ability to learn which sets of driving parameters lead to high-velocity linear locomotion, a weight function was applied to each data point during training, as depicted in Fig. 5.16(b). The weight was assigned based on the normalized velocity of each data point, with a lower bound of 0.1. The normalized velocity was computed as follows: since the robot exhibits asymmetric locomotion capabilities in the positive and negative v_x directions, the most positive velocity, $v_{x,max}$, and the most negative velocity, $v_{x,min}$, were identified. If $v_x \geq 0$ for a given data point, the normalized velocity was calculated as $v_x/v_{x,max}$; otherwise, it was computed as $v_x/v_{x,min}$. This approach ensures that the data points with high velocities in both directions are weighted equally. The same weighting strategy was applied when training the rotational mode model, except that the weight was computed based on ω rather than v_x.

Models trained with and without the weight function were evaluated using 5-fold cross-validation, and the average prediction root mean square errors (RMSEs) are reported in Tables 5.2 and 5.3. The results indicate that weighted models generalize better on high-velocity data points but exhibit higher error when evaluated across the full dataset. This generally suggests that the weighted models learned more information from the high-velocity samples, while the unweighted models captured features from the majority of low-velocity data points. Since the goal is to improve the generalization on high-velocity data points, the chosen weight function is considered effective.

Note that v_y and ω in the linear mode dataset, and v_x and v_y in the rotational mode dataset, result from non-ideal drift. Therefore, they are not the focus of optimization.

The neural network models can help analyze which sets of "linear" driving parameters lead to high $|v_x|$, and which sets of "rotational" driving parameters produce high $|\omega|$. The measured

Table 5.2: Comparison of model performance in linear mode dataset

RMSE for Data Points With $\lvert v_x \rvert > 15$ mm/s			
	v_x (mm/s)	v_y (mm/s)	ω (º/s)
With Weight	**9.6**	5.1	4.8
Without Weight	**11.7**	4.6	4.5
RMSE for All Data Points			
	v_x (mm/s)	v_y (mm/s)	ω (º/s)
With Weight	**6.3**	4.6	4.6
Without Weight	**5.6**	4.4	4.3

Table 5.3: Comparison of model performance in rotational mode dataset

RMSE for Data Points With $\lvert \omega \rvert > 15$ º/s			
	v_x (mm/s)	v_y (mm/s)	**ω (º/s)**
With Weight	6.1	5.4	**7.7**
Without Weight	6.4	5.9	**8.9**
RMSE for All Data Points			
	v_x (mm/s)	v_y (mm/s)	**ω (º/s)**
With Weight	5.8	5.4	**7.0**
Without Weight	5.2	5.0	**6.0**

velocities, model predicted velocities, and absolute prediction errors are visualized in Fig. 5.17. Due to the high-dimensional nature of the variable space (f, ϕ_{12}, D_1, D_2, and either v_x or ω), the frequency f and duty ratio D_2 are omitted in the figure. The models can identify the regions of control parameters which lead to high $|v_x|$ and $|\omega|$, but the exact extreme velocities need to be experimentally determined. As illustrated in Fig. 5.18, the robot reaches 36 mm/s in the leftward ($-x$) direction (predicted as 29 mm/s), and 26 mm/s in the rightward ($+x$) direction (predicted as 15 mm/s). The robot can rotate clockwise at $29°$/s (predicted as $21°$/s) and counterclockwise at $37°$/s (predicted as $25°$/s).

As reported in Table 5.2, Table 5.3, and Fig. 5.18, the average model prediction error is relatively high. Possible sources of error include:

1. Intrinsic electromechanical variations, asymmetries, and time-dependent degradation in the piezoelectric actuators and robotic structure.

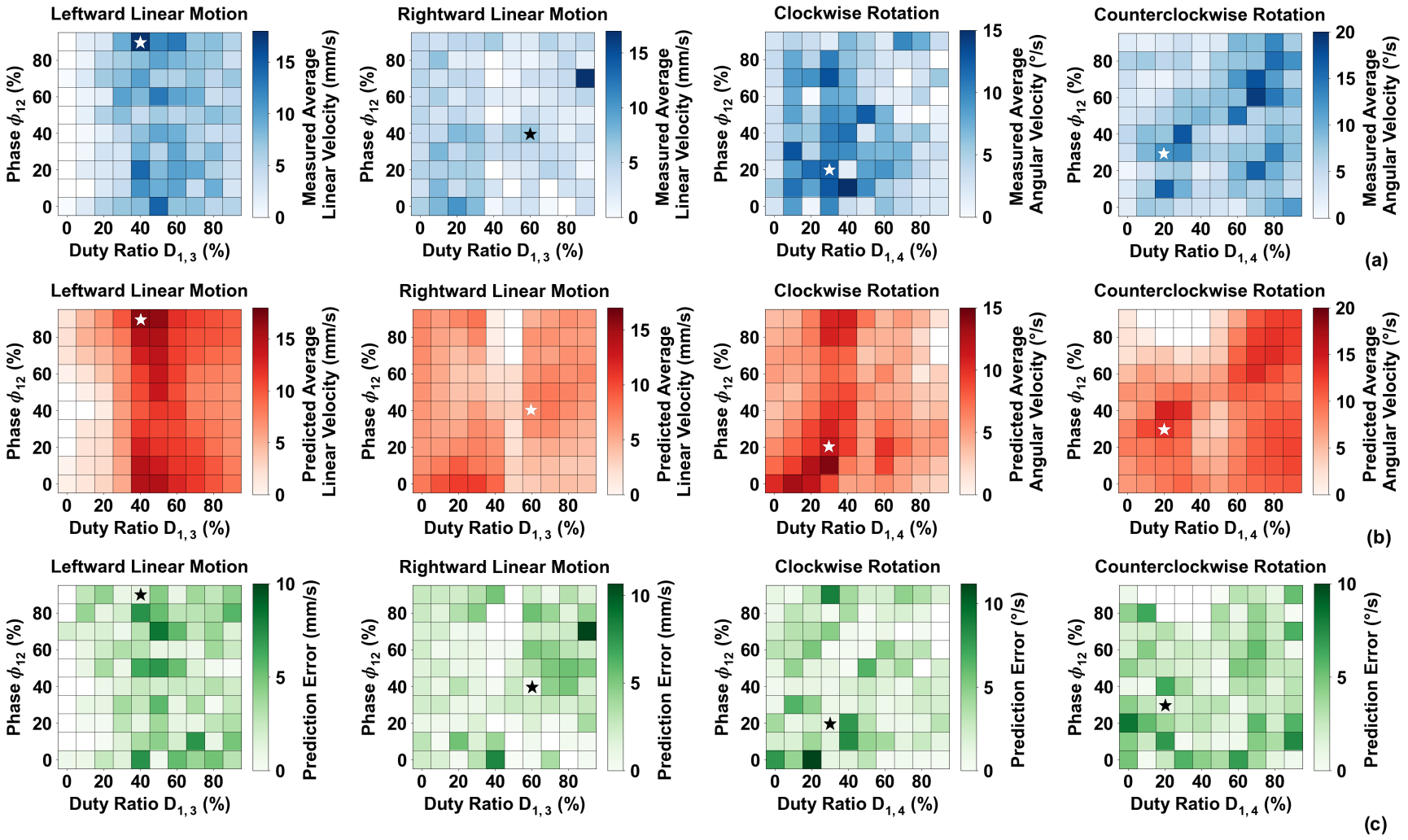

Figure 5.17: (a) Visualization of the robot's average velocity across the parameter space of duty ratio #1 (D_1) and phase (ϕ_{12}), based on measured data for leftward and rightward linear motions, as well as clockwise and counterclockwise rotations. (b) Visualization of average velocity based on predictions from the neural network model. (c) Absolute prediction error, computed as the difference between the heatmaps in rows (a) and (b). The star symbol in each plot denotes the driving parameters reported in Fig. 5.18. The data shown in rows (a) and (b) are the averaged values across driving frequency (f) and duty ratio #2 (D_2)

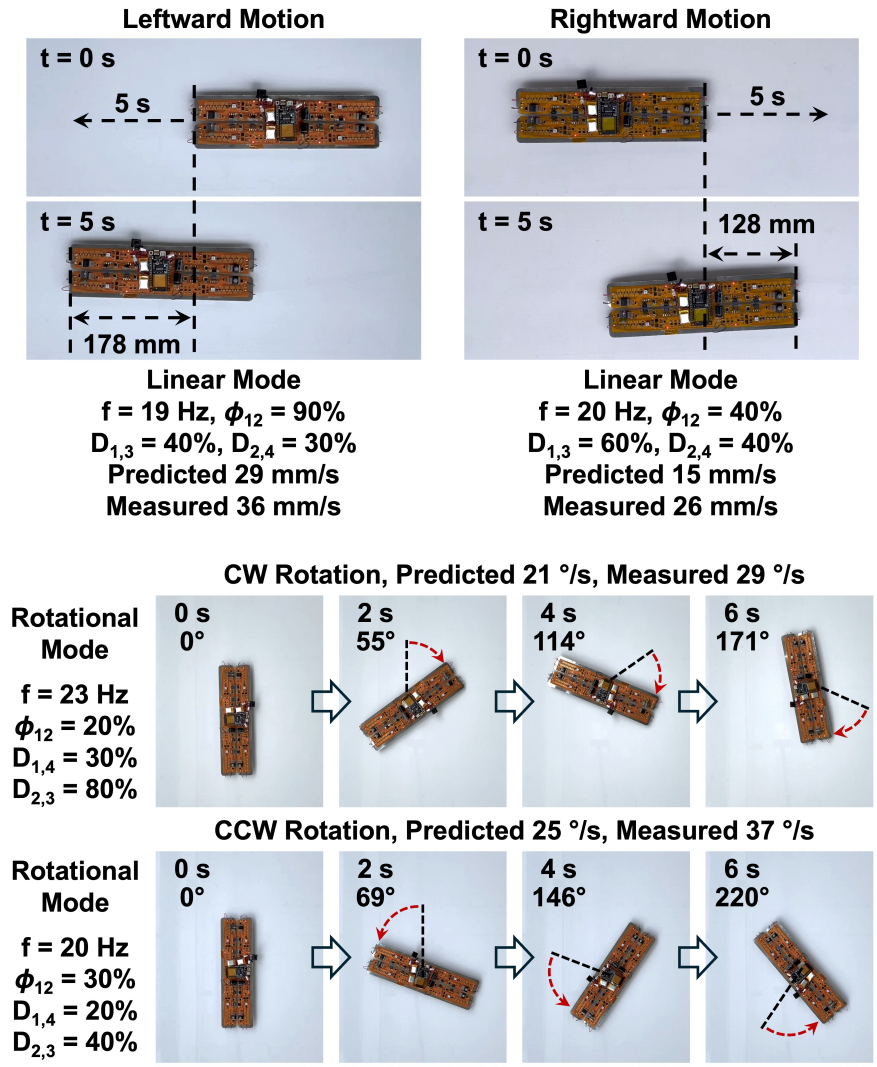

Figure 5.18: Bidirectional linear motion and rotation of the prototype. It achieves a leftward velocity of 36 mm/s and a rightward velocity of 26 mm/s. It can perform clockwise rotation at 29 °/s and counterclockwise rotation at 37 °/s.

2. Variations in the external measurement environment (i.e., nonuniform ground surface).

3. Limitations of the proposed neural network architecture in capturing the nonlinear system dynamics across a wide range of operating conditions.

The combined effect of these factors hinders accurate modeling of eViper's locomotion velocities, necessitating the development of feedback control to precisely regulate the robot's behavior.

5.6.5 Feedback Control and Path Tracking

Due to the limitations outlined above, it is difficult to analytically characterize the relationship between the driving parameters and the robot's velocities. To achieve precise control of the locomotion behavior, feedback control is necessary. A closed-loop feedback control system was constructed based on the OpenCV library in Python, and it instructs the robot to perform a path-tracking task. Fig. 5.19 presents the experimental setup and results. A letter "**P**" was laid out on a tabletop using black vinyl tape. ArUco markers were placed at each turning point of the "**P**" path, and an additional marker was attached at the center of the robot. An external camera monitored the markers' locations. A laptop processed the camera images and remotely sent actuation commands to the prototype to guide it through the path. The prototype was untethered throughout the path-tracking task.

A lookup table was created based on the actuation parameters shown in Fig. 5.18. The feedback controller determined if the robot should adjust its orientation or move linearly based on the current robot position. The duration of each operation was determined by the position and orientation errors, and vision sensing was activated at the end of each operation to provide information for the next action. Given the practical limitations of achieving zero tracking error, a tolerance of 4 cm is specified. The tracking accuracy, defined as the distance between the marker on the robot and the markers on the path, remained within this 4-cm threshold. Sensing hardware can be further optimized to accelerate image processing. The results in Fig. 5.19 confirm eViper's ability to navigate its environment using vision-based closed loop control.

5.6.6 Power Consumption and Energy Efficiency

As described in Section 5.6.2, the collected dataset includes eViper's average power consumption for each set of driving parameters. Dividing the values of $|v_x|$ and $|\omega|$ of each data point by their corresponding power consumption yields the linear and rotational power efficiencies, as depicted in Fig. 5.20. The results indicate that operating eViper in the range of 18 to 25 Hz achieves the highest energy efficiency.

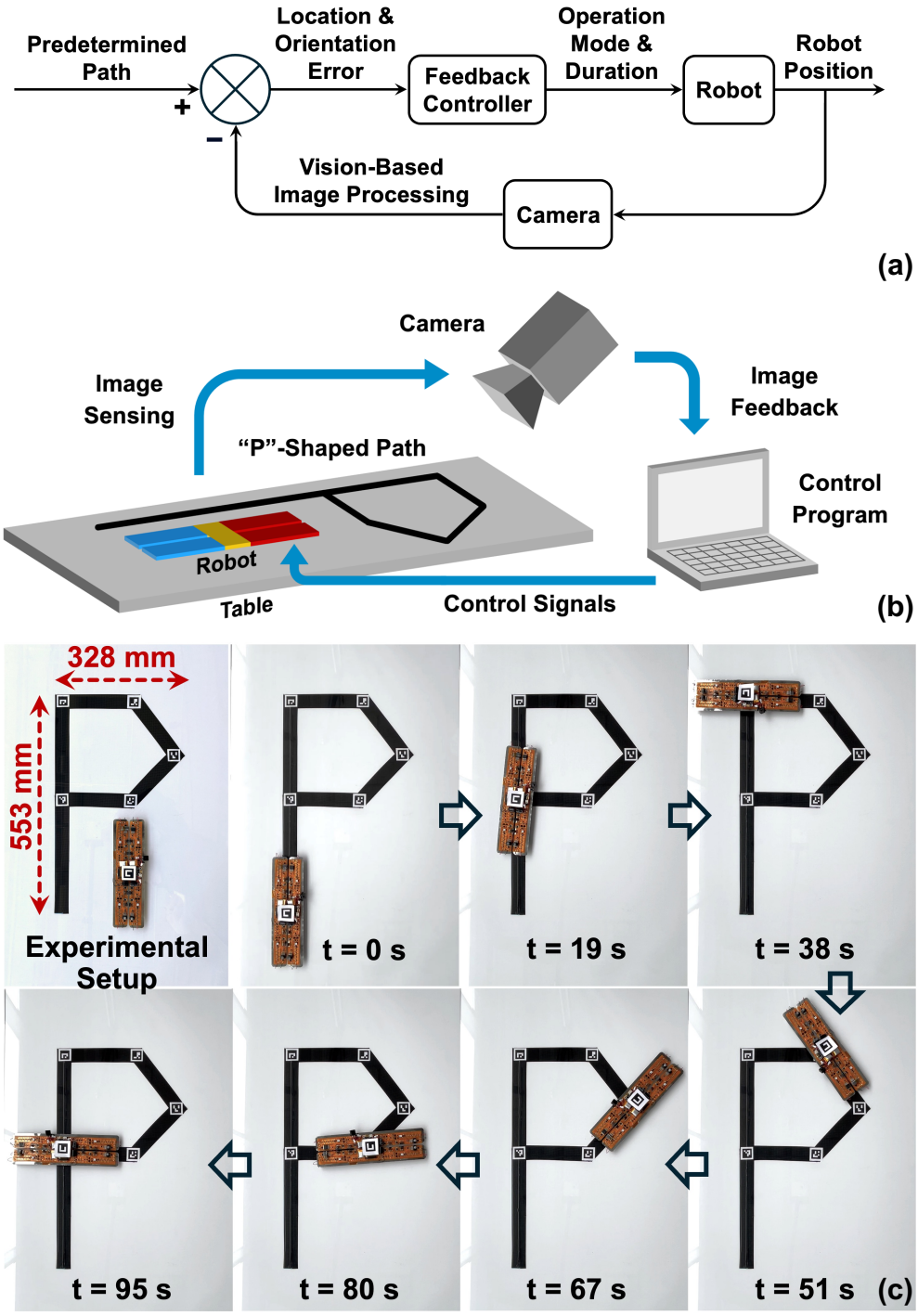

Figure 5.19: (a) Block diagram of the vision-based feedback control framework. The feedback controller instructs the robot on the operating mode and duration based on its position error relative to the predetermined path. (b) Illustration of the feedback control platform for path-tracking task. The "P"-shaped desired path for the robot was created by applying black vinyl tape to a table. (c) The experimental setup and the process of the untethered path-tracking operation.

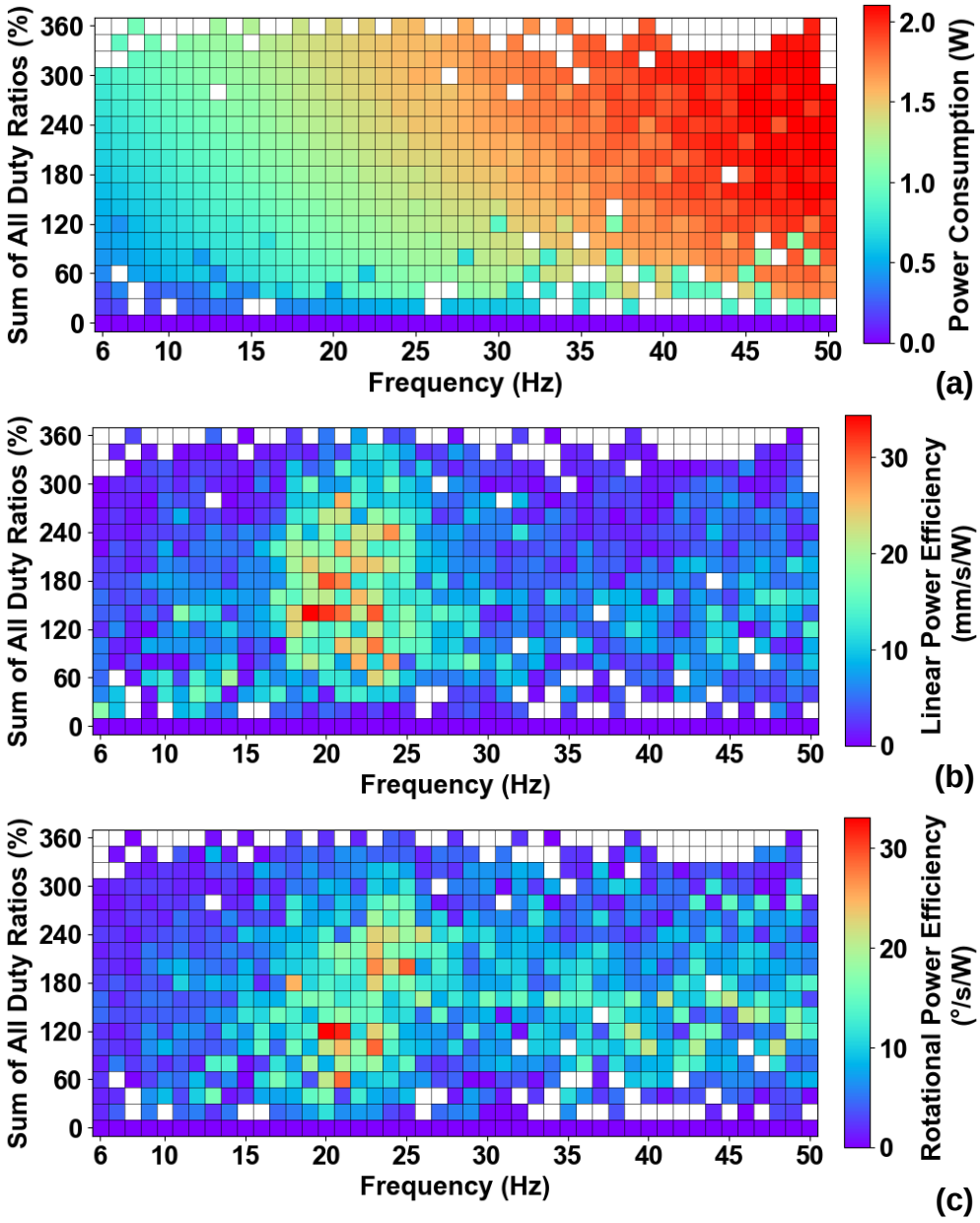

Figure 5.20: Illustration of the (a) power consumption, (b) linear power efficiency, and (c) rotational power efficiency with respect to frequency and duty ratio. The vertical axis shows the sum of duty ratios across the four power modules to reflect the overall system power consumption. The white squares indicate no data was collected. If there are multiple data points that are located in the same square, only the maximum measured data is drawn. (b) and (c) consider only $|v_x|$ and $|\omega|$, respectively.

A piezoelectric actuator is primarily considered a capacitive load. Therefore, increasing the driving frequency requires the circuit to charge and discharge the actuator more times per second, leading to an increase in power consumption. Capacitive energy in piezoelectric actuators can be recycled to improve energy efficiency, as proposed in previous literature [63]. The duty ratio also affects the power consumption because there is a resistive element in the power circuit for voltage regulation. Fig. 5.20(a) verifies that the power consumption has positive correlation with both frequency and duty ratio, with frequency being the dominant factor. Figs. 5.20(b) and 5.20(c) demonstrate the linear and rotational power efficiencies with respect to the operating frequency and duty ratio. The robot is most efficient between 18 and 25 Hz. The efficiency at lower frequencies is reduced because the robot barely moves at those operating points. The efficiency at higher frequencies is also lower due to increased power consumption and reduced velocity.

5.7 Amphibious Operation of eViper

To highlight the versatility of the eViper platform, an amphibious untethered prototype was developed by enclosing the robot in a heat-sealed polyethylene insulation layer. The platform's large surface area and lightweight structure allow it to float on water. The same 3D-printed feet are attached outside the enclosure, enabling the robot to also operate on land. Images of the prototype are shown in Figs. 5.21(a) to 5.21(c). The PCB was re-designed to integrate the Bluetooth microcontroller (ESP32-WROOM-32D, Espressif Systems) directly, eliminating the breakout board. A power management integrated circuit (LTC4079, Analog Devices) was also included to handle battery charging without removing the waterproof layer. The prototype's operation, both on land and on the surface of water, is illustrated in Figs. 5.21(d) and 5.21(e). Fig. 5.21(f) presents composite images that display the transition from land to water.

The prototype was driven on the water surface under multiple driving waveforms and frequencies. Figure 5.22 shows the measured linear and rotational velocities. A general trend is that square-wave excitation yields the highest velocities, whereas triangular-wave excitation yields the lowest. The data points peak around 20 Hz, indicating a resonant behavior of the robot structure. Overall,

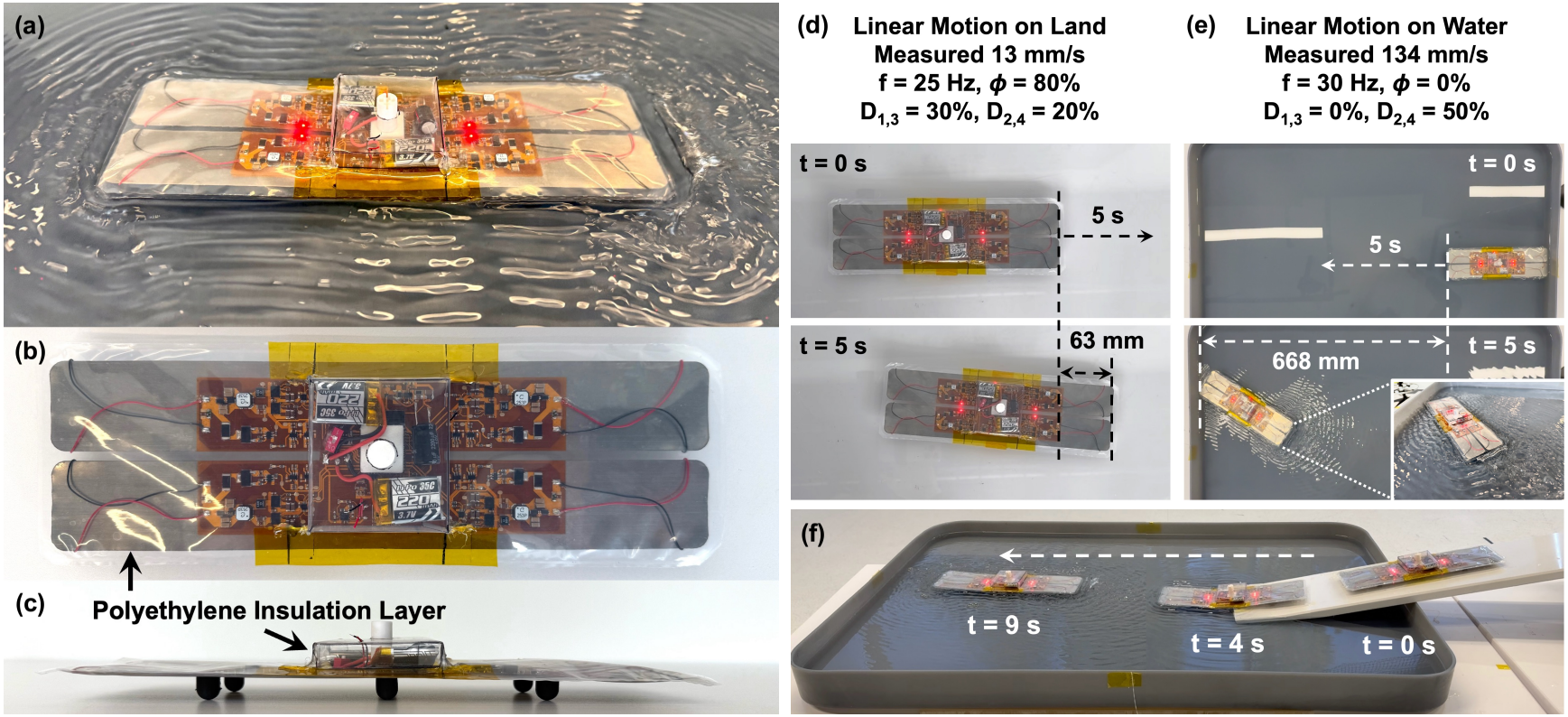

Figure 5.21: (a) An amphibious eViper operating on the surface of water. (b) Top view and (c) side view of the amphibious prototype. (d) Snapshots of the prototype's terrestrial locomotion. (e) Snapshots of the prototype's aquatic operation. (f) Composite images showing the process of eViper moving from a terrestrial environment (a smooth marble tile) to an aquatic environment.

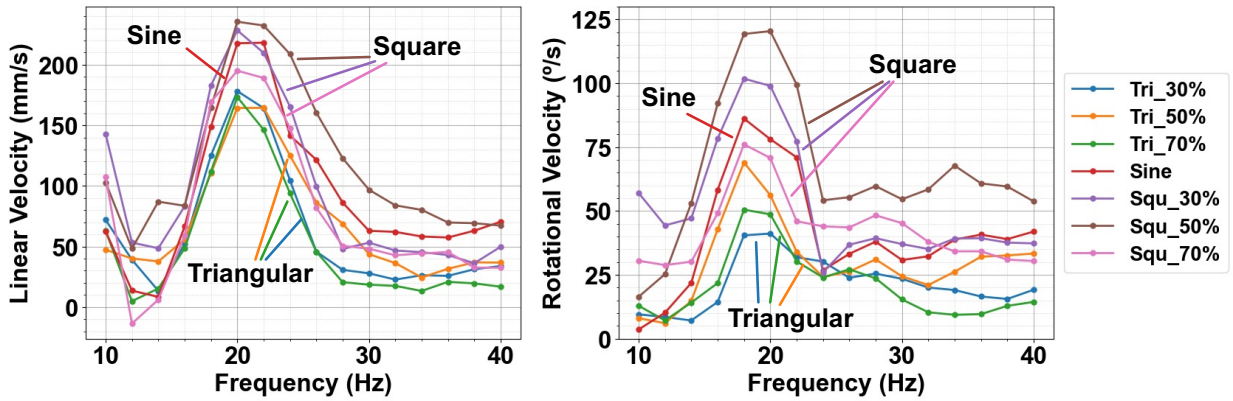

Figure 5.22: Measured linear and rotational velocities of the amphibious eViper under seven driving waveforms (triangular wave with 30%, 50%, and 70% duty ratio, sine wave, and square wave with 30%, 50%, and 70% duty ratio) across a frequency range from 10 to 40 Hz. Only two actuators are driven during the measurement because initial experimental data show that driving all four actuators simultaneously does not produce higher velocities.

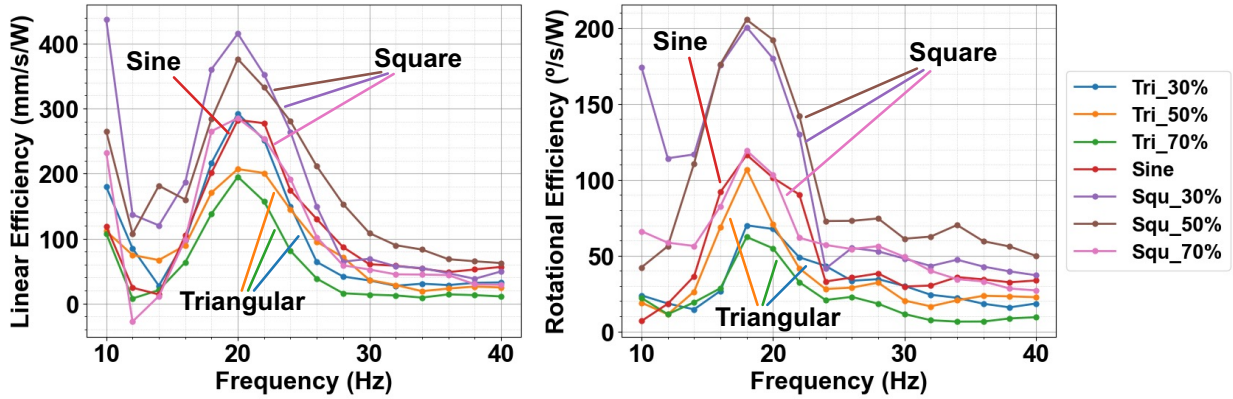

Figure 5.23: Power-to-velocity conversion efficiency computed from data points in Fig. 5.22.

Fig. 5.22 confirms that both the driving waveform and frequency strongly influence the locomotion performance of eViper.

It is also observed that the prototype moves substantially faster on water than on land. Compared with Fig. 5.18, the amphibious eViper achieves a 6.7× higher linear velocity and a 3.3× higher rotational velocity. We ascribe this to the fluid dynamics and the distinct friction profile at the water surface. These results motivate a new and ongoing research direction for the robotic platform.

The power-to-velocity conversion efficiency is computed by dividing the velocity data in Fig. 5.22 by the corresponding power consumption, with the results shown in Fig. 5.23. Similar trends are observed: square-wave excitation yields the highest conversion efficiency, and the efficiency peaks near 20 Hz. It is worth noting that the linear conversion efficiency reaches its

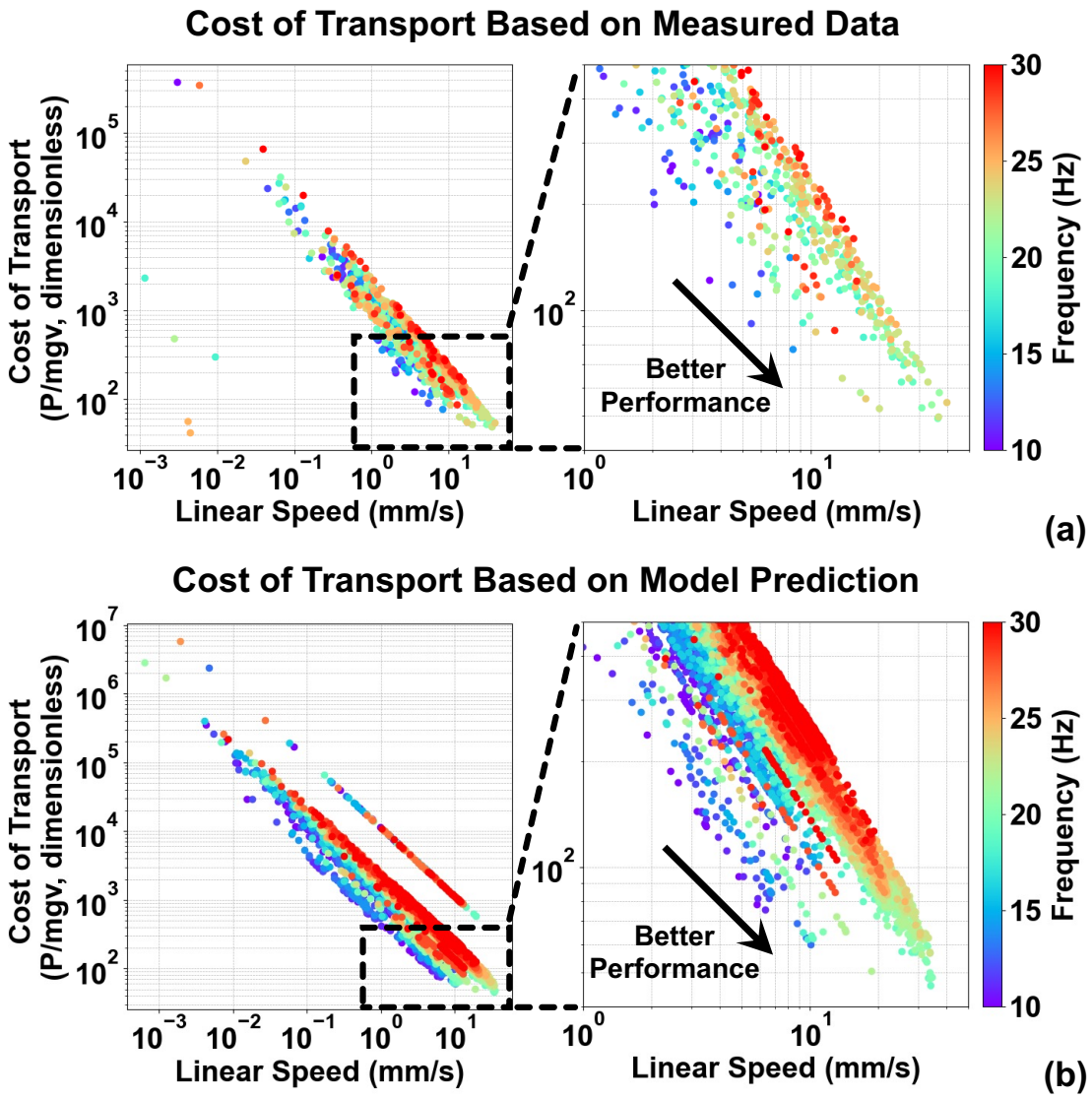

Figure 5.24: Illustration of eViper's cost of transport with respect to the linear speed ($|v_x|$) under different operating frequencies. The distribution of data points is closely aligned between (a) experimentally collected data and (b) neural network model predictions, indicating that the model is effective for sweeping the entire operating parameter space and identifying optimal choices. eViper achieves its lowest cost of transport when operated near 20 Hz.

maximum at 10 Hz when the robot is driven by a square wave with 50% duty ratio. This occurs because the robot maintains a relatively high velocity at 10 Hz while consuming minimal power, resulting in a large efficiency ratio.

5.8 Energy Efficiency and Cost of Transport (COT)

Cost of transport (COT = $\frac{P}{mgv}$, a dimensionless quantity) can be interpreted as the input power required to drive a robot at a constant velocity. It is a widely used metric for comparing locomotion

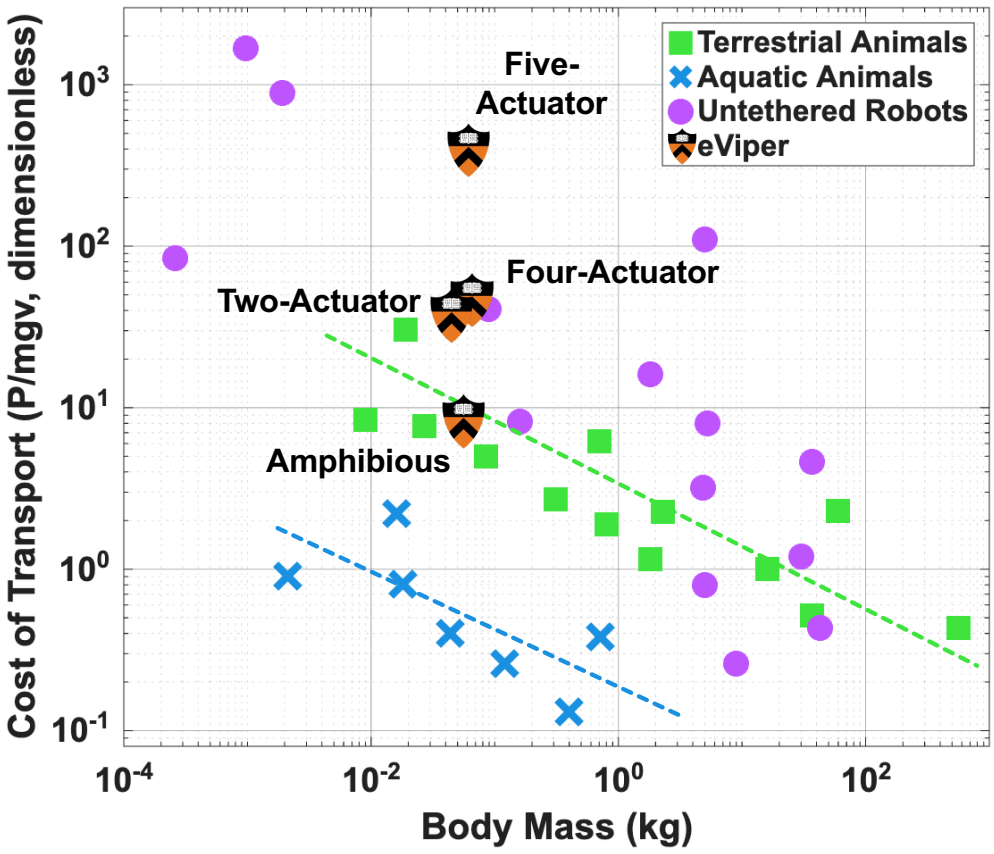

Figure 5.25: The cost of transport (COT, the lower the better) of various animals and bio-inspired robotic systems. This figure was recreated from [65].

efficiency across robotic systems. Fig. 5.24(a) plots eViper's COT for each measured linear-mode data point as a function of linear speed $|v_x|$. An ideal robot has high speed, low power consumption, and low COT; therefore, data points in the lower-right corner of the plot represent the most efficient behaviors. The figure shows that eViper performs the best when operated near 20 Hz. The data-driven model introduced earlier can also be used to generate a similar plot by sweeping through the parameter space and predicting the velocity at each operating point. Fig. 5.24(b) shows the resulting COT, computed using the model predictions combined with power consumption data from Fig. 5.20(a). The data distributions in Figs 5.24(a) and 5.24(b) are well-matched: high-frequency data points (reddish) appear on the upper-right, low-frequency data points (bluish) on the lower left, and mid-frequency data points (greenish) extend to the lower-right corner of the plot. The results demonstrate that the data-driven model is an effective tool for sweeping through the entire

operating space and identifying the optimal operating parameters.

The lowest measured COT of the terrestrial eViper is obtained when the power consumption P = 1.1 W, the robot mass m = 0.0673 kg, the gravitational acceleration g = 9.8 m/s^2, and the robot velocity v = 0.036 m/s (Fig. 5.18 leftmost column). The resulting COT is 46. In aquatic locomotion, the COT decreases to 8 (P = 1.0 W, m = 0.0574 kg, g = 9.8 m/s^2, v = 0.236 m/s, Fig. 5.22). Fig. 5.25 compares the COT of various animals and untethered robots [66–75]. Table 5.4 summarizes key performance metrics for several untethered soft robotic systems.

The eViper platform offers: (1) highly integrated, fully untethered, modular, and scalable power electronics and actuation subsystems; (2) end-to-end co-design opportunities across electrical, mechanical, and control domains; (3) competitive energy efficiency and cost of transport; and (4) adaptability to diverse environments (terrestrial and aquatic) and surfaces (rigid and soft).

5.9 Chapter Summary

This chapter presented four-actuator and amphibious eViper, an untethered soft robotic platform with integrated actuation, power, control, and wireless communication. The robot has high control freedom on each of its four actuators, demonstrating sophisticated locomotion behavior by controlling the electrical driving parameters. The basic robot motion and empirical control methods were first explored, demonstrating that the four-actuator prototype can decouple linear and rotational motion. Through systematic data collection, the prototype's motion sensitivity to nonuniform surface conditions and actuator characteristics was explored, and a data-driven model was developed to analyze the robot's operating principles. An off-board vision-based feedback system and Bluetooth communication enable the robot to perform agile path-tracking. With a waterproofing layer, eViper can float on the surface of water, perform amphibious operations, and move linearly over 230 mm/s. The total power consumption is below 2 W, and the robot operates most efficiently at frequencies near 20 Hz. The eViper platform is highly modular and scalable, and it can be designed in different configurations to support a wide range of robotic missions, with the potential to achieve high energy efficiency through multidisciplinary co-design.

Table 5.4: Comparing this work with other recently published untethered soft robots.

Work	[8]	[10]	[11]	[13]	[15]	eViper	Amphibious eViper
Prototype Length, Weight, and Photo	 20 mm, 1.8 g	 24 mm, 1.9 g	 40 mm, 0.97 g	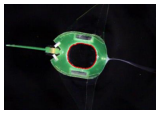 93 mm, 90.3 g	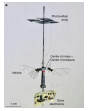 65 mm, 0.26 g	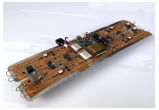 265 mm, 67.3 g	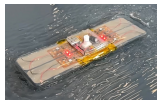 265 mm, 57.4 g
Environment	Land	Land	Land	Water	Air	Land	Land & Water
Actuation Mechanism	Piezo-electricity	Piezo-electricity, Electro-statics	Dielectric Elastomer	Dielectric Elastomer	Piezo-electricity	Piezo-electricity	Piezo-electricity
Path Control	Yes (Tethered)	Yes	Yes	Yes	No	Yes	Yes
Wireless Comm.	No	No	No	Yes	No	Yes	Yes
Onboard Sensing	No	Yes	Yes	No	No	Yes	Yes
2D Scalability	Yes	Unknown	Unknown	Unknown	Unknown	Yes	Yes
Weight Density	4.5 mg/mm^2	3.6 mg/mm^2	1.0 mg/mm^2	8.7 mg/mm^2	N/A	3.4 mg/mm^2	2.9 mg/mm^2
COT	Unknown	887	1670	40	84	46	13

6

Conclusion

6.1 Chapter Introduction

This thesis focuses on the design and development of piezoelectric mechatronic systems. These systems offer fast and precise deformation, high control bandwidth, and compact form factors. Nevertheless, several open problems remain that need to be investigated to further advance their capabilities. The requirement for high actuation voltages and the performance dependency on driving waveforms and frequencies pose challenges for the integrated power converters. System modeling is complicated because the interaction between soft actuators with surrounding rigid structures are difficult to formulate analytically. The energy flow from the power source to the load actuator needs to be studied to provide insight for improving system energy efficiency. Finally, actuator aging and sample-to-sample variations affect behavioral consistency, motivating the need for feedback control to regulate system performance.

This thesis aims to address the challenges outlined above in the context of piezoelectric soft robots. In Chapter 2, the fundamental electromechanical properties, equivalent-circuit modeling, and energy utilization under different driving conditions are investigated, providing the foundation for subsequent chapters. Chapter 3 introduces the design, implementation, and key features of the power system adopted in this research. System-level power flow under different driving waveforms and frequencies is analyzed, supporting energy-aware control strategies. Chapters 4 and 5 document the development and evaluation of multiple eViper prototypes. Modeling approaches for the soft robots are explored via either physics-based simulation tools or data-driven methods. Finally, a feedback control framework is presented to demonstrate the maneuverability of the robotic platform. The remainder of this chapter summarizes the contributions of this thesis and discusses the limitations and future research directions.

6.2 Summary of Contributions

This section summarizes the contributions of this thesis:

- Designed and validated a lightweight, high-voltage power conversion architecture for untethered piezoelectric soft robots, facilitating rapid system iteration through its modularity

and scalability while providing flexible control of output voltage, waveform, and frequency.

- Developed a system-level energy analysis framework that connects battery-level energy input, power electronics behavior, and actuator energy consumption, enabling quantitative study of energy flow in piezoelectric systems.

- Implemented and demonstrated the eViper soft robotic platform as a fully integrated system combining piezoelectric actuators, power electronics, onboard energy storage, control, and wireless communication, providing the foundation for systematic investigation of energy-aware piezoelectric mechatronic systems.

- Established an automated data acquisition pipeline for robotic locomotion studies, enabling data-driven analysis and modeling of soft robot behavior across diverse driving conditions.

- Characterized actuator-level power consumption and robot-level power-to-velocity conversion efficiency over a wide range of driving waveforms and frequencies, revealing key trends that inform energy-aware design and control of piezoelectric robotic systems.

These contributions form a unified framework that spans actuator characterization, circuit design, system integration, and experimental methodology. Collectively, they provide a systematic approach for understanding energy utilization, designing fully untethered piezoelectric mechatronic systems, and developing energy-aware modeling and control strategies. Beyond the specific implementations presented in this thesis, the methods and platforms establish a foundation for future research on scalable, energy-efficient piezoelectric mechatronic systems.

6.3 Limitations and Future Work

Despite the contributions, several technical challenges remain in this field and require further investigation. In Chapter 3, the high-voltage converter's dc-dc power efficiency was satisfactory; however, the efficiency decreased when the converter drove actuators with ac waveforms. Other converter topologies could be further studied to improve the system's dc-ac power efficiency. Additionally, in the current system design, the returned energy during actuator discharge is dissipated

through a resistive path. Circuit configurations that enable energy recycling could be explored to improve overall system energy efficiency.

In Chapters 4 and 5, different system-level modeling approaches were explored, but their predictive accuracy remains limited. The modeling errors could come from multiple sources, including: (1) nonuniform surface conditions that cause friction variation between the robotic feet and the ground; (2) actuator variation and aging effects that are not captured in the models; and (3) nonlinear system dynamics of the integrated prototypes that are insufficiently characterized. The modeling of soft robotic systems is still an open challenge, and future work should place greater emphasis on the uncertainty in contact, friction, and impact dynamics, actuator aging effects, and the integration of data-driven approaches with physics-based analytical models.

In Chapter 5, the data demonstrated that eViper moves much faster on water surface than on land. This marks a promising research direction for future development of this platform because higher mobility is desirable for a wide range of robotic application. Aquatic operation also presents new opportunities for the modeling of system dynamics, as the contact between water surface and robot body is expected to be more uniform. In the pursuit of optimal aquatic eViper operation, future research may further investigate different waterproofing structure, size and number of actuators, and coordination of multiple actuators.

6.4 Final Remarks

This thesis provides an end-to-end power analysis of piezoelectric mechatronic systems. Examining the energy flow across various functional blocks allows informed design optimization and application-specific control strategies. In the context of untethered piezoelectric soft robots, the integrated actuators, power electronics, and robotic functions are tightly coupled, creating significant opportunities for multidisciplinary co-design. The practicality of these robots often depends on the achievable continuous operating time, which is an energy-centric, multivariable optimization problem among battery sizing, power efficiency of driving circuits, power-to-velocity conversion efficiency, control strategies, and overall system mass. Together, these considerations emphasize

the crucial role of energy in piezoelectric mechatronic systems, and this thesis lays a foundation for future design and implementation of these platforms.

References

[1] Xiangyu Gao, Jikun Yang, Jingen Wu, Xudong Xin, Zhanmiao Li, Xiaoting Yuan, Xinyi Shen, and Shuxiang Dong. Piezoelectric Actuators and Motors: Materials, Designs, and Applications. *Advanced Materials Technologies*, 5(1):1900716, January 2020.

[2] S Mohith, Adithya R Upadhya, Karanth P Navin, S M Kulkarni, and Muralidhara Rao. Recent trends in piezoelectric actuators for precision motion and their applications: A review. *Smart Materials and Structures*, 30(1):013002, January 2021.

[3] Jing Li, Jie Deng, Shijing Zhang, Weishan Chen, Jie Zhao, and Yingxiang Liu. Developments and Challenges of Miniature Piezoelectric Robots: A Review. *Advanced Science*, 10(36):2305128, December 2023.

[4] Shijing Zhang, Yingxiang Liu, Jie Deng, Xiang Gao, Jing Li, Weiyi Wang, Mingxin Xun, Xuefeng Ma, Qingbing Chang, Junkao Liu, Weishan Chen, and Jie Zhao. Piezo robotic hand for motion manipulation from micro to macro. *Nature Communications*, 14(1):500, January 2023.

[5] Haoyue Xue, Jing Jin, Zhi Tan, Keliang Chen, Gengxi Lu, Yushun Zeng, Xiaolin Hu, Xingchen Peng, Laiming Jiang, and Jiagang Wu. Flexible, biodegradable ultrasonic wireless electrotherapy device based on highly self-aligned piezoelectric biofilms. *Science Advances*, 10(22):eadn0260, May 2024.

[6] R.J. Wood, E. Steltz, and R.S. Fearing. Nonlinear Performance Limits for High Energy Density Piezoelectric Bending Actuators. In *Proceedings of the 2005 IEEE International Conference on Robotics and Automation*, pages 3633–3640, Barcelona, Spain, 2005. IEEE.

[7] Xuyang Zhou, Shuang Wu, Xiaoxu Wang, Zhenshan Wang, Qixuan Zhu, Jinshuai Sun, Panfeng Huang, Xuewen Wang, Wei Huang, and Qianbo Lu. Review on piezoelectric actuators: Materials, classifications, applications, and recent trends. *Frontiers of Mechanical Engineering*, 19(1):6, February 2024.

[8] Weilei Mu, Mengjiao Li, Erdong Chen, Yiduo Yang, Jie Yin, Xiaoming Tao, Guijie Liu, and Rong Yin. Spiral-Shape Fast-Moving Soft Robots. *Advanced Functional Materials*, 33(35):2300516, August 2023.

[9] Erdong Chen, Yiduo Yang, Mengjiao Li, Binghang Li, Guijie Liu, Weilei Mu, and Rong Yin. Bio-Mimic, Fast-Moving, and Flippable Soft Piezoelectric Robots. *Advanced Science*, 10(20):2300673, July 2023.

[10] Jiaming Liang, Yichuan Wu, Justin K. Yim, Huimin Chen, Zicong Miao, Hanxiao Liu, Ying Liu, Yixin Liu, Dongkai Wang, Wenying Qiu, Zhichun Shao, Min Zhang, Xiaohao Wang, Junwen Zhong, and Liwei Lin. Electrostatic footpads enable agile insect-scale soft robots with trajectory control. *Science Robotics*, 6(55):eabe7906, June 2021.

[11] Xiaobin Ji, Xinchang Liu, Vito Cacucciolo, Matthias Imboden, Yoan Civet, Alae El Haitami, Sophie Cantin, Yves Perriard, and Herbert Shea. An autonomous untethered fast soft robotic insect driven by low-voltage dielectric elastomer actuators. *Science Robotics*, 4(37):eaaz6451, December 2019.

[12] Hsin Cheng, Zhiwu Zheng, Prakhar Kumar, Wali Afridi, Ben Kim, Sigurd Wagner, Naveen Verma, James C. Sturm, and Minjie Chen. eViper: A Scalable Platform for Untethered Modular Soft Robots. In *2023 IEEE/RSJ International Conference on Intelligent Robots and Systems (IROS)*, pages 604–611, Detroit, MI, USA, October 2023. IEEE.

[13] Tiefeng Li, Guorui Li, Yiming Liang, Tingyu Cheng, Jing Dai, Xuxu Yang, Bangyuan Liu, Zedong Zeng, Zhilong Huang, Yingwu Luo, Tao Xie, and Wei Yang. Fast-moving soft electronic fish. *Science Advances*, 3(4):e1602045, April 2017.

[14] Guorui Li, Xiangping Chen, Fanghao Zhou, Yiming Liang, Youhua Xiao, Xunuo Cao, Zhen Zhang, Mingqi Zhang, Baosheng Wu, Shunyu Yin, Yi Xu, Hongbo Fan, Zheng Chen, Wei Song, Wenjing Yang, Binbin Pan, Jiaoyi Hou, Weifeng Zou, Shunping He, Xuxu Yang, Guoyong Mao, Zheng Jia, Haofei Zhou, Tiefeng Li, Shaoxing Qu, Zhongbin Xu, Zhilong Huang, Yingwu Luo, Tao Xie, Jason Gu, Shiqiang Zhu, and Wei Yang. Self-powered soft robot in the Mariana Trench. *Nature*, 591(7848):66–71, March 2021.

[15] Noah T. Jafferis, E. Farrell Helbling, Michael Karpelson, and Robert J. Wood. Untethered flight of an insect-sized flapping-wing microscale aerial vehicle. *Nature*, 570(7762):491–495, June 2019.

[16] Steven I. Rich, Robert J. Wood, and Carmel Majidi. Untethered soft robotics. *Nature Electronics*, 1(2):102–112, February 2018.

[17] Alireza Fath, Tian Xia, and Wei Li. Recent Advances in the Application of Piezoelectric Materials in Microrobotic Systems. *Micromachines*, 13(9):1422, August 2022.

[18] Yeongju Jung, Kangkyu Kwon, Jinwoo Lee, and Seung Hwan Ko. Untethered soft actuators for soft standalone robotics. *Nature Communications*, 15(1):3510, April 2024.

[19] Zhiwu Zheng, Prakhar Kumar, Yenan Chen, Hsin Cheng, Sigurd Wagner, Minjie Chen, Naveen Verma, and James C. Sturm. Model-Based Control of Planar Piezoelectric Inchworm Soft Robot for Crawling in Constrained Environments. In *2022 IEEE 5th International Conference on Soft Robotics (RoboSoft)*, pages 693–698, Edinburgh, United Kingdom, April 2022. IEEE.

[20] Zhiwu Zheng, Prakhar Kumar, Yenan Chen, Hsin Cheng, Sigurd Wagner, Minjie Chen, Naveen Verma, and James C. Sturm. Piezoelectric Soft Robot Inchworm Motion by Tuning Ground Friction Through Robot Shape: Quasi-Static Modeling and Experimental Validation. *IEEE Transactions on Robotics*, 40:2339–2356, 2024.

[21] Meng Yu, Weimin Yang, Yuan Yu, Xiang Cheng, and Zhiwei Jiao. A Crawling Soft Robot Driven by Pneumatic Foldable Actuators Based on Miura-Ori. *Actuators*, 9(2):26, April 2020.

[22] Pang Wu, Wang Jiangbei, and Fei Yanqiong. The Structure, Design, and Closed-Loop Motion Control of a Differential Drive Soft Robot. *Soft Robotics*, 5(1):71–80, February 2018.

[23] Abraham Simpson Chen and Sarah Bergbreiter. Electroadhesive feet for turning control in legged robots. In *2016 IEEE International Conference on Robotics and Automation (ICRA)*, pages 3806–3812, Stockholm, Sweden, May 2016. IEEE.

[24] Luigi Calabrese, Alice Berardo, Danilo De Rossi, Massimiliano Gei, Nicola Maria Pugno, and Gualtiero Fantoni. A soft robot structure with limbless resonant, stick and slip locomotion. *Smart Materials and Structures*, 28(10):104005, October 2019.

[25] Jiaming Liang, Xiaohao Wang, Liwei Lin, Yichuan Wu, Zhichun Shao, Justin K. Yim, Renxiao Xu, Yi Song, Mingjing Qi, Junwen Zhong, and Min Zhang. Manipulating the Moving Trajectory of Insect-Scale Piezoelectric Soft Robots by Frequency. In *2019 IEEE 32nd International Conference on Micro Electro Mechanical Systems (MEMS)*, pages 1041–1044, Seoul, Korea (South), January 2019. IEEE.

[26] Hassan H. Hariri, Leonardus A. Prasetya, Shaohui Foong, Gim Song Soh, Kevin N. Otto, and Kristin L. Wood. A tether-less Legged Piezoelectric Miniature Robot using bounding gait locomotion for bidirectional motion. In *2016 IEEE International Conference on Robotics and Automation (ICRA)*, pages 4743–4749, Stockholm, Sweden, May 2016. IEEE.

[27] Erwin Coumans. Bullet physics simulation. In *ACM SIGGRAPH 2015 Courses*, page 1, Los Angeles California, July 2015. ACM.

[28] Erwin Coumans and Yunfei Bai. PyBullet, January 2016.

[29] Emanuel Todorov, Tom Erez, and Yuval Tassa. MuJoCo: A physics engine for model-based control. In *2012 IEEE/RSJ International Conference on Intelligent Robots and Systems*, pages 5026–5033, Vilamoura-Algarve, Portugal, October 2012. IEEE.

[30] Jack Collins, Shelvin Chand, Anthony Vanderkop, and David Howard. A Review of Physics Simulators for Robotic Applications. *IEEE Access*, 9:51416–51431, 2021.

[31] Zhiwu Zheng, Hsin Cheng, Prakhar Kumar, Sigurd Wagner, Minjie Chen, Naveen Verma, and James C. Sturm. Wirelessly-Controlled Untethered Piezoelectric Planar Soft Robot Capable of Bidirectional Crawling and Rotation. In *2023 IEEE International Conference on Robotics and Automation (ICRA)*, pages 641–647, London, United Kingdom, May 2023. IEEE.

[32] Hsin Cheng, Elias Veilleux, Zhiwu Zheng, Sigurd Wagner, Naveen Verma, James C. Sturm, and Minjie Chen. eViper-2D: A Thin Large-Area Soft Robotics Platform. In *2025 IEEE International Conference on Robotics and Automation (ICRA)*, pages 15336–15342, Atlanta, GA, USA, May 2025. IEEE.

[33] Smart Material Corporation. Macro Fiber Composite (MFC) Data Sheet, February 2025.

[34] Kenji Uchino. *Advanced Piezoelectric Materials*. Elsevier/ Woodhead publishing, 2nd edition edition, 2017.

[35] Dragan Damjanovic. Hysteresis in Piezoelectric and Ferroelectric Materials. In *The Science of Hysteresis*, pages 337–465. Elsevier, 2006.

[36] A Erturk and D J Inman. An experimentally validated bimorph cantilever model for piezoelectric energy harvesting from base excitations. *Smart Materials and Structures*, 18(2):025009, February 2009.

[37] G.K. Ottman, H.F. Hofmann, A.C. Bhatt, and G.A. Lesieutre. Adaptive piezoelectric energy harvesting circuit for wireless remote power supply. *IEEE Transactions on Power Electronics*, 17(5):669–676, September 2002.

[38] Mingjie Guan and Wei-Hsin Liao. Studies on the circuit models of piezoelectric ceramics. In *International Conference on Information Acquisition, 2004. Proceedings.*, pages 26–31, Hefei, China, 2004. IEEE.

[39] Michael Karpelson, Gu-Yeon Wei, and Robert J. Wood. Driving high voltage piezoelectric actuators in microrobotic applications. *Sensors and Actuators A: Physical*, 176:78–89, April 2012.

[40] Zhen Qiu, M. R. Sadiq, C. Demore, M. F. Parker, P. Marin, K. Mayne, and S. Cochran. Characterization of piezocrystals for practical configurations with temperature- and pressure-dependent electrical impedance spectroscopy. *IEEE Transactions on Ultrasonics, Ferroelectrics and Frequency Control*, 58(9):1793–1803, September 2011.

[41] Congrui Jin and Xiaodong Wang. Analytical modelling of the electromechanical behaviour of surface-bonded piezoelectric actuators including the adhesive layer. *Engineering Fracture Mechanics*, 78(13):2547–2562, August 2011.

[42] Xuerong Liu, Yuanming Xu, Xiangyu Wang, Yunmeng Ran, and Weifang Zhang. Effect of Adhesive and Its Aging on the Performance of Piezoelectric Sensors in Structural Health Monitoring Systems. *Metals*, 10(10):1342, October 2020.

[43] Hong Wang, Sung-Min Lee, James L. Wang, and Hua-Tay Lin. Fatigue of extracted lead zirconate titanate multilayer actuators under unipolar high field electric cycling. *Journal of Applied Physics*, 116(23):234101, December 2014.

[44] Yuri A. Genenko, Julia Glaum, Michael J. Hoffmann, and Karsten Albe. Mechanisms of aging and fatigue in ferroelectrics. *Materials Science and Engineering: B*, 192:52–82, February 2015.

[45] Sanghyeon Park, Daniel S. Drew, Sean Follmer, and Juan Rivas-Davila. Lightweight High Voltage Generator for Untethered Electroadhesive Perching of Micro Air Vehicles. *IEEE Robotics and Automation Letters*, 5(3):4485–4492, July 2020.

[46] Haofeng Xu, Yiou He, Kieran L. Strobel, Christopher K. Gilmore, Sean P. Kelley, Cooper C. Hennick, Thomas Sebastian, Mark R. Woolston, David J. Perreault, and Steven R. H. Barrett. Flight of an aeroplane with solid-state propulsion. *Nature*, 563(7732):532–535, November 2018.

[47] Yiou He, Mark Woolston, and David Perreault. Design and implementation of a lightweight high-voltage power converter for electro-aerodynamic propulsion. In *2017 IEEE 18th Workshop on Control and Modeling for Power Electronics (COMPEL)*, pages 1–9, Stanford, CA, USA, July 2017. IEEE.

[48] Tianshi Xie, Miquel Ricart Oltra, and Hanh-Phuc Le. A 5kV/15W Dual-Transformer Hybrid Converter with Extreme 2000X Conversion Ratios for Soft Mobile Robots. In *2020 IEEE Applied Power Electronics Conference and Exposition (APEC)*, pages 1548–1552, New Orleans, LA, USA, March 2020. IEEE.

[49] Venkata Anand Kishore Prabhala, Poria Fajri, Venkat Sai Prasad Gouribhatla, Bhanu Prashant Baddipadiga, and Mehdi Ferdowsi. A DC–DC Converter With High Voltage Gain and Two Input Boost Stages. *IEEE Transactions on Power Electronics*, 31(6):4206–4215, June 2016.

[50] Yanqiao Li, Benjamin L. Dobbins, and Jason T. Stauth. 33.8 A Decentralized Daisy-Chain-Controlled Switched-Capacitor Driver for Microrobotic Actuators with 10× Power-Reduction Factor and Over 300V Drive Voltage. In *2021 IEEE International Solid- State Circuits Conference (ISSCC)*, pages 474–476, San Francisco, CA, USA, February 2021. IEEE.

[51] Yanqiao Li, Bahlakoana Mabetha, and Jason T. Stauth. A 3. 7V-to-1kV Chip-Cascaded Switched-Capacitor Converter with Auxiliary Boost Achieving $> 96{\%}$ Reactive Power Efficiency for Electrostatic Drive Applications. In *2023 IEEE International Solid- State Circuits Conference (ISSCC)*, pages 1–3, San Francisco, CA, USA, February 2023. IEEE.

[52] Robert W. Erickson and Dragan Maksimović. *Fundamentals of Power Electronics*. Springer, Cham, third edition edition, 2020.

[53] Zhiwu Zheng, Prakhar Kumar, Yenan Chen, Hsin Cheng, Sigurd Wagner, Minjie Chen, Naveen Verma, and James C. Sturm. Scalable Simulation and Demonstration of Jumping Piezoelectric 2-D Soft Robots. In *2022 International Conference on Robotics and Automation (ICRA)*, pages 5199–5204, Philadelphia, PA, USA, May 2022. IEEE.

[54] Cecilia Laschi, Barbara Mazzolai, and Matteo Cianchetti. Soft robotics: Technologies and systems pushing the boundaries of robot abilities. *Science Robotics*, 1(1):eaah3690, December 2016.

[55] Matteo Cianchetti, Cecilia Laschi, Arianna Menciassi, and Paolo Dario. Biomedical applications of soft robotics. *Nature Reviews Materials*, 3(6):143–153, May 2018.

[56] Meng Li, Aniket Pal, Amirreza Aghakhani, Abdon Pena-Francesch, and Metin Sitti. Soft actuators for real-world applications. *Nature Reviews Materials*, 7(3):235–249, November 2021.

[57] Yichuan Wu, Justin K. Yim, Jiaming Liang, Zhichun Shao, Mingjing Qi, Junwen Zhong, Zihao Luo, Xiaojun Yan, Min Zhang, Xiaohao Wang, Ronald S. Fearing, Robert J. Full, and Liwei Lin. Insect-scale fast moving and ultrarobust soft robot. *Science Robotics*, 4(32):eaax1594, July 2019.

[58] YuFeng Chen, Siyi Xu, Zhijian Ren, and Pakpong Chirarattananon. Collision Resilient Insect-Scale Soft-Actuated Aerial Robots With High Agility. *IEEE Transactions on Robotics*, 37(5):1752–1764, October 2021.

[59] Guoyong Mao, David Schiller, Doris Danninger, Bekele Hailegnaw, Florian Hartmann, Thomas Stockinger, Michael Drack, Nikita Arnold, and Martin Kaltenbrunner. Ultrafast small-scale soft electromagnetic robots. *Nature Communications*, 13(1):4456, August 2022.

[60] Noah T Jafferis, Mario Lok, Nastasia Winey, Gu-Yeon Wei, and Robert J Wood. Multilayer laminated piezoelectric bending actuators: Design and manufacturing for optimum power density and efficiency. *Smart Materials and Structures*, 25(5):055033, May 2016.

[61] Levent E. Aygun, Prakhar Kumar, Zhiwu Zheng, Ting-Sheng Chen, Sigurd Wagner, James C. Sturm, and Naveen Verma. Hybrid LAE-CMOS Force-Sensing System Employing TFT-Based Compressed Sensing for Scalability of Tactile Sensing Skins. *IEEE Transactions on Biomedical Circuits and Systems*, 13(6):1264–1276, December 2019.

[62] Noah T. Jafferis, Howard A. Stone, and James C. Sturm. Traveling wave-induced aerodynamic propulsive forces using piezoelectrically deformed substrates. *Applied Physics Letters*, 99(11):114102, September 2011.

[63] Yanqiao Li, Bahlakoana Mabetha, and Jason T. Stauth. A Modular Switched-Capacitor Chip-Stacking Drive Platform for kV-Level Electrostatic Actuators. *IEEE Journal of Solid-State Circuits*, 58(12):3530–3543, December 2023.

[64] Mario Lok, Elizabeth Farrell Helbling, Xuan Zhang, Robert Wood, David Brooks, and Gu-Yeon Wei. A Low Mass Power Electronics Unit to Drive Piezoelectric Actuators for Flying Microrobots. *IEEE Transactions on Power Electronics*, 33(4):3180–3191, April 2018.

[65] Robert Baines, Sree Kalyan Patiballa, Joran Booth, Luis Ramirez, Thomas Sipple, Andonny Garcia, Frank Fish, and Rebecca Kramer-Bottiglio. Multi-environment robotic transitions through adaptive morphogenesis. *Nature*, 610(7931):283–289, October 2022.

[66] Kyunam Kim, Patrick Spieler, Elena-Sorina Lupu, Alireza Ramezani, and Soon-Jo Chung. A bipedal walking robot that can fly, slackline, and skateboard. *Science Robotics*, 6(59):eabf8136, October 2021.

[67] Gerardo Bledt, Matthew J. Powell, Benjamin Katz, Jared Di Carlo, Patrick M. Wensing, and Sangbae Kim. MIT Cheetah 3: Design and Control of a Robust, Dynamic Quadruped Robot. In *2018 IEEE/RSJ International Conference on Intelligent Robots and Systems (IROS)*, pages 2245–2252, Madrid, October 2018. IEEE.

[68] Marco Hutter, Christian Gehring, Dominic Jud, Andreas Lauber, C. Dario Bellicoso, Vassilios Tsounis, Jemin Hwangbo, Karen Bodie, Peter Fankhauser, Michael Bloesch, Remo Diethelm, Samuel Bachmann, Amir Melzer, and Mark Hoepflinger. ANYmal - a highly mobile and dynamic quadrupedal robot. In *2016 IEEE/RSJ International Conference on Intelligent Robots and Systems (IROS)*, pages 38–44, Daejeon, South Korea, October 2016. IEEE.

[69] Y. Sakagami, R. Watanabe, C. Aoyama, S. Matsunaga, N. Higaki, and K. Fujimura. The intelligent ASIMO: System overview and integration. In *IEEE/RSJ International Conference on Intelligent Robots and System*, volume 3, pages 2478–2483, Lausanne, Switzerland, 2002. IEEE.

[70] A.D. Kuo. Choosing Your Steps Carefully. *IEEE Robotics & Automation Magazine*, 14(2):18–29, June 2007.

[71] Vance A. Tucker. Energetic cost of locomotion in animals. *Comparative Biochemistry and Physiology*, 34(4):841–846, June 1970.

[72] William I. Sellers, Kayleigh A.R. Rose, Dane A. Crossley, and Jonathan R. Codd. Inferring cost of transport from whole-body kinematics in three sympatric turtle species with different locomotor habits. *Comparative Biochemistry and Physiology Part A: Molecular & Integrative Physiology*, 247:110739, September 2020.

[73] F Berlinger, M Saadat, H Haj-Hariri, G V Lauder, and R Nagpal. Fish-like three-dimensional swimming with an autonomous, multi-fin, and biomimetic robot. *Bioinspiration & Biomimetics*, 16(2):026018, March 2021.

[74] Nathan Kau, Aaron Schultz, Natalie Ferrante, and Patrick Slade. Stanford Doggo: An Open-Source, Quasi-Direct-Drive Quadruped. In *2019 International Conference on Robotics and Automation (ICRA)*, pages 6309–6315, Montreal, QC, Canada, May 2019. IEEE.

[75] Uluc Saranli, Martin Buehler, and Daniel E. Koditschek. RHex: A Simple and Highly Mobile Hexapod Robot. *The International Journal of Robotics Research*, 20(7):616–631, July 2001.